DEPARTAMENTO DE FÍSICA ATÓMICA MOLECULAR Y NUCLEAR

DIRECT MEASUREMENT OF RESONANCE DRIVING TERMS IN THE SUPER PROTON SYNCHROTRON (SPS) OF CERN USING BEAM POSITION MONITORS

ROGELIO TOMÁS GARCÍA

UNIVERSITAT DE VALENCIA
Servei de Publicacions
2002

Aquesta Tesi Doctoral va ser presentada a Valencia el día 30 de
Maig de 2003 davant un tribunal format per:

- Dr. D. Antonio Ferrer Soria
- Dr. D. Joan Bordas Orpinell
- Dr. D. Jorge Velasco Gonzalez
- Dr. D. Luigi Palumbo
- Dr. D. Frank Zimmermann

Va ser dirigida per:
Prof. Dra. Dña. Angeles Faus Golfe y Dr. D. Frank Schmiot

DOCTORAL THESIS
Direct Measurement of Resonance Driving Terms in the Super Proton Synchrotron (SPS) of CERN using Beam Position Monitors

AUTHOR
Rogelio Tomás García

SUPERVISORS
Angeles Faus Golfe
Frank Schmidt

DEFENDED THE 30th OF MAY OF 2003
TRIBUNAL
Antonio Ferrer Soria
Jorge Velasco Gonzalez
Joan Bordas Orpinell
Luigi Palumbo
Frank Zimmermann

MARK
Sobresaliente cum laude

In this thesis a beam based technique is developed to measure the Hamiltonian terms of an accelerator by precise Fast Fourier Transform of turn-by-turn beam position data. To this aim analytical derivations, simulations and experiments in two different accelerators are performed. The first analytical derivation consists on describing the effect of the beam particle distribution on the Fourier spectrum of the turn-by-turn motion. This study leads to the appearance of decoherence factors that reduce the amplitude of the non-linear spectral lines. The second analytical derivation describes how the resonance driving terms vary around the accelerator. It is demonstrated that these terms remain constant along sections free of non-linearities and abruptly change at the location of the non-linear elements. This property permits to localise the non-linear sources by measuring the resonance driving terms around the ring using the beam position monitors. In order to demonstrate the applicability of this technique in a real accelerator experiments were performed at the SPS of CERN and at the RHIC of BNL. The SPS is a very linear accelerator equipped with eight powerful sextupoles that were used to introduce a controlled amount of non-linearity. Measurements and predictions from the model are in good agreement. In the SPS a method to measure and compensate the linear coupling was also developed. The RHIC, as the future LHC, is a superconducting machine with a large content of non-linearity. Sextupolar resonances were measured in this accelerator using the presented technique obtaining a satisfactory agreement with the model. Lastly an improvement of the technique is studied analytically consisting on using an AC dipole instead of applying a single kick. This has the main advantage of not being destructive.

The future Large Hadron Collider (LHC) will provide proton-proton collisions with a center of mass energy of 14 TeV. The circumference of this machine will be 27 km and the magnetic field in the dipoles will be 8.4 T. The LHC magnet system consists of 1232 superconducting dipoles and 386 superconducting quadrupoles together with 20 different types of magnets for experimental insertions and correction systems. In a conventional magnet the field is mainly defined by the shape of the iron poles which can be realized with an accuracy of the order of 0.01 mm. In a superconducting magnet the field is mainly defined by the spatial distribution of the superconducting cables of the coils, which can be positioned with an accuracy of 0.1 mm. This difference makes the superconducting magnets intrinsically less precise than the normal conducting magnets. Furthermore in the superconducting magnets there are persistent currents in the filaments, which are the memory of the former variations of the field. The real field in a superconducting magnet is represented by a multipolar expansion whose coefficients correspond to the different multipolar field errors. Each one of these multipoles contributes to the dynamics of the confined particles in a precise way represented by a set of Hamiltonian terms. Nevertheless only the linear part of the Hamiltonian, defined by the dipoles and the quadrupoles, has an exact solution of the motion (equivalent to that of a harmonic oscillator). The higher multipoles, e.g. the sextupole and the octupole, define the non-linear motion of the particle. Solutions to the non-linear motion can only be approximated around a fix point using perturbative approaches. Furthermore, for large oscillation amplitudes, the particle motion becomes chaotic and unstable. The region of the phase space where the motion remains stable over a sufficiently large number of

turns is called the dynamic aperture of the machine. The LHC has a tight dynamic aperture budget, for this reason it will be equipped with different non-linear corrector magnets that will be used to enlarge the dynamic aperture by compensating the effect of the multipolar errors of the magnets.

In this thesis a beam based technique is developed to measure the Hamiltonian resonance driving terms of an accelerator by precise Fast Fourier Transform (FFT) of turn-by-turn beam position data. To this aim analytical derivations, simulations and experiments in two different accelerators are performed. The first analytical derivation consists on describing the effect of the beam particle distribution on the Fourier spectrum of the turn-by-turn motion. This study leads to analytical expressions that describe the particular shape of the different Fourier lines. The main conclusion is the observation of the appearance of decoherence factors that reduce the amplitude of the non-linear spectral lines. The spectral line $(m,0)$, i.e. the spectral line with a frequency m times the fundamental horizontal frequency, is reduced by a factor of $|m|$. As well the width of the spectral line is almost linear with the order of the line.

The second analytical derivation describes how the resonance driving terms vary around the accelerator. It is demonstrated that these terms remain constant along sections free of non-linearities and abruptly change at the location of the non-linear elements. This property permits to localise the non-linear sources by measuring the resonance driving terms around the ring using the beam position monitors.

All the analytical predictions have been confirmed by numerical simulations of an SPS model. To reproduce the decoherence a large amount of particles fulfilling Gaussian

disributions were tracked through the lattice. The turn-by-turn centroid position was computed by taking the average of the particle positions at every turn. The Fourier spectrums of these signals were confronted with the analytical formulas obtaining a satisfactory agreement.

In order to demonstrate the applicability of this technique in a real accelerator experiments were performed at the SPS of CERN and at the RHIC of BNL. The SPS is a very linear accelerator equipped with eight powerful sextupoles that were used to introduce a controlled amount of non-linearity. The main conclusion from the SPS experiments is that coupling and sextupolar terms were measured around the ring and the results are in good agreement with the predictions from the model. Other important conclusions follow. It was possible to identify locations with or without non-linearities. Correct sextupole polarities were inferred from measurements. A method to measure and compensate the linear coupling was also developed.

The RHIC is a superconducting machine with a large content of non-linearity. This accelerator serves as an ideal test bed in order to apply this technique to the LHC. Sextupolar resonances were measured in this accelerator using the presented technique obtaining a satisfactory agreement with the model.

Lastly an improvement of the technique is studied analytically that consists on using an AC dipole instead of applying a single kick. This has the main advantage of not being destructive. Furthermore no decoherence factors have to be taken into account and the data samples can be as long as desired. However the resonance driving terms in presence of the AC dipole differ from the natural resonance terms. This difference should not be large for low orders and the local information of either kind of terms is

equivalent. New resonances appear as a result of having introduced a new frequency in the dynamics.

Universitat de València

DEPARTAMENT DE FÍSICA ATÒMICA

MOLECULAR I NUCLEAR

UNIVERSITAT DE VALÈNCIA

Direct Measurement of Resonance Driving Terms in the Super Proton Synchrotron (SPS) of CERN using Beam Position Monitors

TESIS DE DOCTORADO
ROGELIO TOMÁS GARCÍA
Enero de 2003

Dra. ANGELES FAUS GOLFE, Técnico Superior de Investigación de la Universidad de Valencia (UVEG),
Dr. FRANK SCHMIDT, miembro del European Organization For Nuclear Research (CERN),

CERTIFICAN:

Que la presente memoria "Direct Measurement of Resonance Driving Terms in the Super Proton Synchrotron (SPS) of CERN using Beam Position Monitors" ha sido realizada bajo nuestra dirección en el Departamento de Física Atómica, Molecular y Nuclear de la Universitat de València por D. Rogelio Tomás García y constituye su Tesis Doctoral.

Y para que conste, firmamos el presente Certificado.

Angeles Faus Golfe   Frank Schmidt

Contents

Notation

LHC	Large Hadron Collider
FFT	Fast Fourier Transform
SPS	Super Proton Synchrotron
B_x, B_y	transverse components of the magnetic field
BPM	Beam Position Monitor
x, y	transverse coordinates
s	longitudinal coordinate
z	stands for x or y
M	linear map
$M(s)$	linear one turn map starting at s
$e^{:f:}$	Lie operator with f as generating function
$[f, g]$	Poisson bracket of f and g
$\mathcal{M}$	total one turn map
R	linear one turn map expressed as a rotation
h	non–linear Hamiltonian
$Q_{x,y}$	linear transverse tunes
Q_s	longitudinal or synchrotron tune
$\nu_{x,y}$	non–linear transverse tunes
h_{jklm}	Hamiltonian terms
F	generating function of the non–linear change of basis
f_{jklm}	generating function terms
H	Hamiltonian in the Normal Form basis
J, ϕ	action–angle variables
I, ψ	action–angle variables in the Normal Form basis
$h_{x,y}^{\pm}$	linearly normalized basis
$\zeta_{x,y}^{\pm}$	Normal Form basis
δ	relative momentum deviation
$Q'_{x,y}$	chromaticity
$\nu'_{xx}, \nu'_{xy}, \nu'_{yy}$	amplitude detuning coefficients
ρ_x, ρ_y, ρ_s	densities
J_n	Bessel function of order n
I_n	modified Bessel function of order n
δ_{Dirac}	Dirac delta function
$MOPOS$	Multi Orbit Position System

rms	root mean square
$SIXTRACK$	single particle tracking code [23]
$SUSSIX$	code for frequency analysis of non–Linear motion
$RHIC$	Relativistic Heavy Ion Collider
ALS	Advanced Light Source
AGS	Alternating Gradient Synchrotron
PLL	Phase Lock Loop

Chapter 1

Introduction

The future Large Hadron Collider (LHC) will provide proton–proton collisions with a center of mass energy of 14 TeV. The circumference of this machine will be 27 km and the magnetic field in the dipoles will be 8.4 T. The LHC magnet system consists of 1232 superconducting dipoles and 386 superconducting quadrupoles together with 20 different types of magnets for experimental insertions and correction systems. In a conventional magnet the field is mainly defined by the shape of the iron poles which can be realized with an accuracy of the order of 0.01 mm. In a superconducting magnet the field is mainly defined by the spatial distribution of the superconducting cables of the coils, which can be positioned with an accuracy of 0.1 mm. This difference makes the superconducting magnets intrinsically less precise than the normal conducting magnets. Furthermore in the superconducting magnets there are persistent currents in the filaments, which are the memory of the former variations of the field. The real field in a superconducting magnet is defined by the following multipolar expansion [1],

$$B_y + iB_x = B_r \sum_{n=1}^{\infty} [b_n(s) + ia_n(s)] \left(\frac{x + iy}{R_r} \right)^{n-1} ,$$

where B_r is the amplitude of the nominal field of the magnet at a radius R_r, b_n and a_n are the normal and the skew relative coefficients of the $2n$–pole (expressing the field errors) and R_r is the radius of the measurement coil. R_r is known as reference radius. For a multipole of order n the field is increasing with the power $(n-1)$ of the radius. To represent a dipole B_r is set to the value of the vertical magnetic field and b_1 is set to 1. The lowest order multipole error of the dipole is given by a_1, which is a constant horizontal field. The following errors in increasing order are b_2 and a_2, normal and skew quadrupolar fields, b_3 and a_3, normal and skew sextupolar fields, etc. Each one of these multipoles contributes to the dynamics of the confined particles in a precise way represented by a set of Hamiltonian terms. Nevertheless only the linear part of the Hamiltonian, defined by the dipoles ($n = 1$) and the quadrupoles ($n = 2$), has an exact solution of the motion (equivalent to that of a harmonic oscillator). The higher multipoles, e.g. the sextupole ($n = 3$) and

the octupole ($n = 4$), define the non–linear motion of the particle. Solutions to the non–linear motion can only be approximated around a fix point using perturbative approaches. Furthermore, for large oscillation amplitudes, the particle motion becomes chaotic and unstable. The region of the phase space where the motion remains stable over a sufficiently large number of turns is called the dynamic aperture of the machine. The LHC has a tight dynamic aperture budget, for this reason it will be equipped with different non–linear corrector magnets that will be used to enlarge the dynamic aperture by compensating the effect of the multipolar errors of the magnets. Measurements of the multipole coefficients of the magnets will be done prior to their installation in the tunnel. Nevertheless all magnets may not be measured and their properties may change during the installation process. Therefore beam based techniques to measure these field imperfections will be of great help in the commissioning and running of the machine.

The aim of this thesis is to develop a beam based method to measure the Hamiltonian terms of an accelerator by precise Fast Fourier Transform (FFT) of turn–by–turn beam position data. The first attempt to perform such measurements was made in [2]. In this work, in the framework of the first order perturbation theory, it has been studied how the spectra from tracking and experimental turn–by–turn data can be related to non–linear Hamiltonian terms. An important prerequisite to make possible this analysis was a more precise technique than the standard FFT [3] to compute the spectrum of the motion. Similar attempts were performed in the field of celestial mechanics by Laskar [4]. This approach is known as the frequency map analysis. Recently new techniques were developed [5], allowing an even more precise determination of the fundamental frequencies. The frequency map analysis can also be used to find spectral lines in descending order of magnitude. The relation between the Hamiltonian terms and the spectral lines of single particle motion is derived in [6]. Presently other methods are being studied for the measurement of the non–linear content of a machine. Some interesting references are: [7], [8], [9], [10], [11], [12] and [13]. They will be briefly discussed in the last section of this thesis.

In this thesis two theoretical aspects of the measurement of the resonance driving terms are developed. The first one is to derive an analytical relation between the Hamiltonian terms and the spectral lines of the beam centroid motion. The starting point of this work is the relation given in [6] between the Hamiltonian terms and the spectral lines of single particle motion. The results from these analytical studies will be compared to computer simulations using the model of the Super Proton Synchrotron (SPS) at CERN. The second aspect is the study of the variation of the Hamiltonian terms around the ring. In a real machine this information could be obtained by using the beam position monitors (BPMs). The intrinsic variation of these terms could be of great use for localizing important sources of errors.

Experiments have been done in the CERN SPS to measure coupling and sextupolar resonance driving terms. The measurement of the coupling resonance terms provides an efficient way of correcting the coupling. The extraction sextupoles were used to introduce a controllable amount of non–linearity. By computing the

Fourier spectrum of the turn–by–turn BPM data sextupolar resonance terms were measured around the ring. These measurements are compared to the predictions of the model for the different settings used. Similar measurements have been performed in the Relativistic Heavy Ion Collider (RHIC) of BNL which is a superconducting machine. This shows that this technique can be applied to more complex machines.

A major improvement of this method to measure the resonance driving terms has been analytically studied. Instead of applying a transverse kick, a forced oscillation is induced to the beam by an AC dipole with a frequency close to the fundamental frequency. This has the advantage of being a non destructive measurement and not being affected by decoherence processes.

Chapter 2

Maps in accelerators

The dynamics of a system such as a circular accelerator could be described using Hamiltonian flows or according to the discrete formalism of transfer maps. A transfer map is a set of functions that give a final set of phase space coordinates as a function of the initial set of phase space coordinates. This formalism is the non–linear generalization of transfer matrices used to describe the linear motion in an accelerator. In that case the linear transfer maps are represented by matrices. The use of transfer maps to describe the particle transverse dynamics in accelerators is justified by the discrete nature of magnetic elements. Furthermore maps have the advantage of being easily implementable on computers. Neglecting any non–linear element an accelerator could be represented by a product of matrices, each of them corresponding to a magnet or a drift (free field region). The non–linear map formalism provides the equivalent tool to the matrices in the linear systems. Therefore a realistic representation of the accelerator is given by a concatenation of non–linear maps and matrices. Nevertheless the motion of a particle in an accelerator could be obtained only approximately by using perturbative methods. The perturbative methods used in the non–linear map theory are more powerful than those used in the classical perturbative Hamiltonian theory.

2.1 Linear maps

The motion of a particle in an accelerator is usually described relative to the reference orbit defined by the dipoles for a particle with momentum p_0. The moving coordinate system is shown in fig. 2.1, where s, x and y are the longitudinal, horizontal and vertical coordinates respectively and ρ is the radius of curvature. High energy particles travel at a constant speed close to the speed of light. The path length s is given by $s = vt$. The transverse phase space in accelerators is defined as (x, x', y, y'), where the prime denotes the derivative over the path length. In the following the maps of the most important linear elements are given:

- Drift.
  The simplest element of an accelerator is a field free region or drift. The
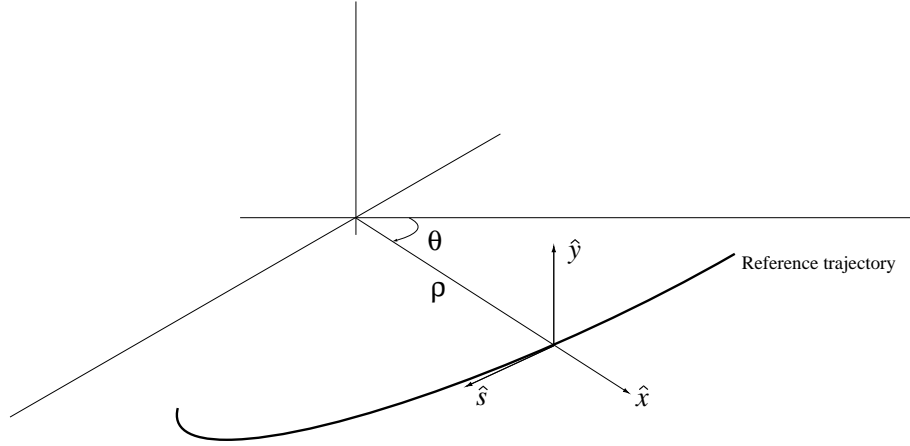
Figure 2.1: Coordinate system used for accelerators.

linear map that describes a drift of length L in the phase space is given by

$$\begin{pmatrix} z \\ z' \end{pmatrix}_{s+L} = \begin{pmatrix} 1 & L \\ 0 & 1 \end{pmatrix} \begin{pmatrix} z \\ z' \end{pmatrix}_s , \tag{2.1}$$

where z stands for x or y.

• Dipole.
A sector dipole, see figure 2.2, is a section of length L with a constant verti-
cal magnetic field and the edges perpendicular to the central trajectory. Ver-
tically the motion is equivalent to a drift of length L but horizontally the map
is given by

$$\begin{pmatrix} x \\ x' \end{pmatrix}_{s+L} = \begin{pmatrix} \cos(L/\rho) & \rho\sin(L/\rho) \\ (1/\rho)\sin(L/\rho) & \cos(L/\rho) \end{pmatrix} \begin{pmatrix} x \\ x' \end{pmatrix}_s , \tag{2.2}$$

where ρ is the radius of curvature of the reference orbit.

• Quadrupole.
A quadrupole, see figure 2.3, produces a linear magnetic field which vanishes
at the reference orbit. The gradient of the quadrupole k is defined as

$$k = \frac{q}{p_0} \frac{\partial B_y}{\partial x} ,$$

where q is the charge of the particle. A focusing quadrupole ($k > 0$) of
length L is described as

$$\begin{pmatrix} z \\ z' \end{pmatrix}_{s+L} = \begin{pmatrix} \cos\psi & (1/\sqrt{k})\sin\psi \\ -\sqrt{k}\sin\psi & \cos\psi \end{pmatrix} \begin{pmatrix} z \\ z' \end{pmatrix}_s , \tag{2.3}$$

with $\psi = L\sqrt{k}$. Similarly, a defocusing quadrupole ($k < 0$) of length L is described as

$$\begin{pmatrix} z \\ z' \end{pmatrix}_{s+L} = \begin{pmatrix} \cosh\psi & (1/\sqrt{k})\sinh\psi \\ \sqrt{k}\sinh\psi & \cosh\psi \end{pmatrix} \begin{pmatrix} z \\ z' \end{pmatrix}_s , \qquad (2.4)$$

with $\psi = L\sqrt{|k|}$.

For simplicity these expressions are given for a particle with the design momentum p_0. The advantage of this formalism is that particles can be propagated trough sections of several magnets by multiplying 2×2 matrices. The one turn matrix $M(s)$ for a circular accelerator is the transfer matrix that propagates the particle through all the elements back to the starting location s. It is constructed by multiplying all the elements in the form

$$M(s_1) = M_{N+1}M_N \cdots M_2M_1 , \qquad (2.5)$$

where M_i are the matrices of the corresponding linear elements. The one turn matrices at different locations are connected via similarity transformations, for example

$$M(s_2) = M_1 M(s_1) M_1^{-1} . \qquad (2.6)$$

To guarantee the stability of the motion over a large number of turns $M(s)$ has to be connected to a pure rotation matrix via a similarity transformation. The angle of rotation in the phase space is called tune and is represented by Q_z. Its fractional part can be computed from $M(s)$ using the following expression,

$$2\cos(2\pi Q_z) = Tr[M(s)] \qquad (2.7)$$

where $Tr[M(s)]$ represents the trace of the corresponding 2×2 one–turn matrix. The parametrization of the turn–by–turn coordinates at a given location of the ring s_0 is given by [14]

$$x(N) = \sqrt{\epsilon_x \beta_x(s_0)} \cos(2\pi Q_x N + \phi_x) \qquad (2.8)$$

$$y(N) = \sqrt{\epsilon_y \beta_y(s_0)} \cos(2\pi Q_y N + \phi_y) \qquad (2.9)$$

where N is the number of turns, ϵ_z and ϕ_z are given by the initial conditions of the particle and β_z are the betatronic functions. Comparing to the harmonic oscillator, ϵ_z represents the energy of the oscillation. ϵ_z is called the transverse emittance and $\pi\epsilon_z$ is the area enclosed by the trajectory of the particle in the phase space (z,z'). ϕ_z is the initial phase. The betatronic function $\beta_z(s)$ represents the amplitude modulation due to the changing focusing strength. For more details see [15].
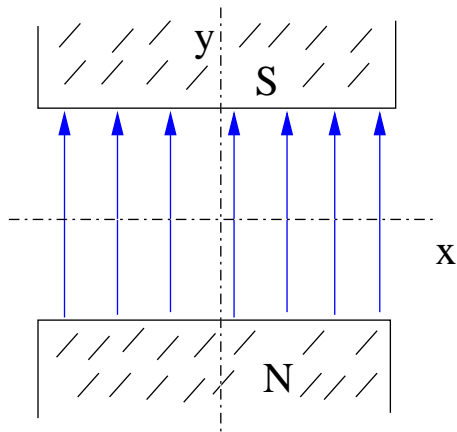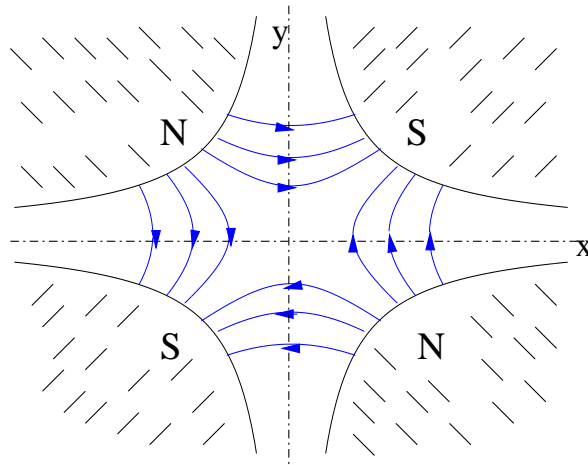
Figure 2.2: Dipole magnet.
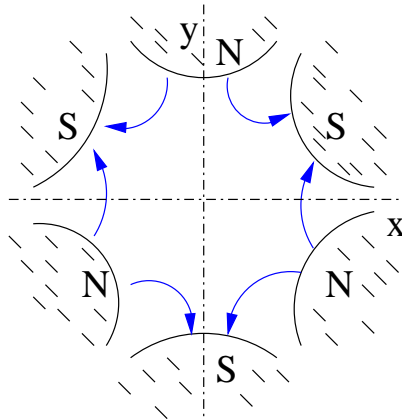
Figure 2.3: Quadrupole magnet.

Figure 2.4: Sextupole magnet.

2.2   Non–linear maps

The lowest order non–linear element is the sextupole. The sextupole, see figure 2.4, produces a magnetic field that increases quadratically in the transverse coordinates,

$$
\begin{aligned}
B_x &= B_3 2xy \,, \\
B_y &= B_3(x^2 - y^2)
\end{aligned}
\tag{2.10}
$$

For large accelerators it is a good approximation to assume that B_3 is a Dirac delta function along the longitudinal coordinate at the location of the sextupoles. This is called thin lens approximation and has the advantage that the final coordinates will be functions only of the initial positions x and y. The transfer map of a thin sextupole placed at s is given by

$$
\begin{pmatrix} x \\ x' \\ y \\ y' \end{pmatrix}_{s+\epsilon}
=
\begin{pmatrix} x \\ x' \\ y \\ y' \end{pmatrix}_{s}
+
\frac{qLB_3}{p}
\begin{pmatrix} 0 \\ x^2 - y^2 \\ 0 \\ -2xy \end{pmatrix} \,,
\tag{2.11}
$$

where LB_3 is the integrated strength of the sextupole.

In general the magnetic field of a multipole of order n is given by

$$
B_y(x, y) + iB_x(x, y) = [B_n(s) + iA_n(s)](x + iy)^{n-1}
\tag{2.12}
$$

The terms $B_n(s)$ and $A_n(s)$ in eq. (2.12) are called *normal* and *skew* coefficients and they are given by the expressions

$$
B_n(s) = \frac{1}{(n-1)!} \frac{\partial^{n-1} B_y}{\partial x^{n-1}}\bigg|_{(0,0;s)}
\tag{2.13}
$$

$$
A_n(s) = \frac{1}{(n-1)!} \frac{\partial^{n-1} B_x}{\partial x^{n-1}}\bigg|_{(0,0;s)}
\tag{2.14}
$$

Notice that B_n and A_n are absolute values, contrary to b_n and a_n that were introduced relatively to the main field and the radius of the expansion. A skew multipole of order n is a normal multipole of order n rotated by $90°/n$ in the transverse plane. Higher multipoles are, for example, the octupole ($n\!=\!4$, third order in x and y) and the decapole ($n\!=\!5$, fourth order in x and y). In presence of these non–linear elements the maps are no longer matrices and an alternative approach has to be used. In this work Taylor maps (see section 3) are used to represent these non–linear multipole elements. The total Hamiltonian can be expressed as the sum $H_0 + H_1$ where H_0 is the linear part already described with matrices and H_1 contains the contributions of all the non–linear lenses. The magnetic field of one element can be derived from a vector potential with only the longitudinal component. Therefore H_1 is proportional to this component of the magnetic vector potential, $A_s(x, y, s)$,

which is obtained by taking the real part of the primitive of the magnetic field expansion. The perturbation Hamiltonian is given by

$$H_1 = -\frac{q}{p}\mathrm{Re}\left[\sum_{n=3}^{\infty}\frac{1}{n}[B_n(s) + iA_n(s)](x + iy)^n\right] \qquad (2.15)$$

The perturbative approach followed in this work consists of the following steps:

- Construction of the one–turn–map associated to the Hamiltonian (section 3.2) using Taylor approach. Basically the one–turn–map is the set of functions that relate the initial position of the particle in the phase space to the final position after one turn.

- Construction of the Normal Form of the one–turn–map (section 3.3). A change of coordinates is done in a way that the new one–turn–map is much simpler than the initial one.

- The particle trajectories in the Normal Form basis are transformed into the initial phase space by inverting the previous change of coordinates (section 3.4).

All these steps will be presented up to first order in the perturbation parameters.

Chapter 3

Taylor maps

A Taylor map expresses a final set of coordinates as polynomial functions of an initial set of coordinates. The most general way to represent this kind of map is using the exponential Lie operator. The exponential Lie operator is written as $e^{:f:}$. It operates on differentiable functions and is defined by

$$e^{:f:}g = g + [f, g] + \frac{1}{2}[f, [f, g]] + \dots \tag{3.1}$$

where $[f, g]$ is the Poisson bracket of any functions f and g of the phase space coordinates defined by

$$[f, g] = \frac{\partial f}{\partial \vec{x}} \frac{\partial g}{\partial \vec{p}} - \frac{\partial f}{\partial \vec{p}} \frac{\partial g}{\partial \vec{x}} \ . \tag{3.2}$$

When $e^{:f:}$ operates on a coordinate function, the result

$$x_f = e^{:f:}x = x + [f, x] + \frac{1}{2}[f, [f, x]] + \dots \tag{3.3}$$

can be interpreted as the value of the coordinate at a time $t = 1$, expressed as a function of the coordinates at time $t = 0$, for a dynamical system with a Hamiltonian $H = -f$. Therefore the exponential Lie operator of a thin lens can be constructed by multiplying its Hamiltonian, as given in eq. (2.15), by the length of the magnet (that is the time like variable) and putting it with a minus sign in the exponent. As an illustration the exponential Lie operator corresponding to a sextupolar thin lens is constructed. The Hamiltonian of a normal sextupole is given by eq. (2.15),

$$-\frac{qB_3}{3p}\left(x^3 - 3xy^2\right) \ . \tag{3.4}$$

11

Therefore the Lie operator is given by

$$
\begin{aligned}
x_f &= e^{L\frac{qB_3}{3p}(x_0^3 - 3x_0 y_0^2)} x_0 && = x_0 \; , \\
p_{xf} &= e^{L\frac{qB_3}{3p}(x_0^3 - 3x_0 y_0^2)} p_{x0} && = p_{x0} + \frac{qLB_3}{p}(x_0^2 - y_0^2) \; , \\
y_f &= e^{L\frac{qB_3}{3p}(x_0^3 - 3x_0 y_0^2)} y_0 && = y_0 \; , \\
p_{yf} &= e^{L\frac{qB_3}{3p}(x_0^3 - 3x_0 y_0^2)} p_{y0} && = p_{y0} - \frac{qLB_3}{p} 2x_0 y_0 \; ,
\end{aligned}
\tag{3.5}
$$

notice that only the momentum coordinates are changed by the map. This is known as "multipole kick" and its Hamiltonian is named "kick Hamiltonian". To construct the one–turn map of an accelerator including multipole kicks represented by exponential Lie operators some of its properties are needed. These properties are described in the following section.

3.1   Properties of the exponential Lie operator

- **Action on polynomial functions**. Using eq. (3.3) it can be shown that

$$
e^{:f:} x^n = x_f^n \; ,
\tag{3.6}
$$

  and thus for any polynomial function $g(x)$ it follows

$$
g(x_f) = g(e^{:f:} x) = e^{:f:} g(x)
\tag{3.7}
$$

- **Composition of exponential Lie operators**. Suppose we have two operators, $e^{:f_1(z_1):}$ mapping the phase space z_1 into the phase space z_2 and the second operator $e^{:f_2(z_2):}$ mapping z_2 into z_3. The composition of the maps is expressed as

$$
z_3 = e^{:f_2(z_2):} e^{:f_1(z_1):} z_1 = e^{:f_2(z_2):} z_2 = g(z_2) \; .
\tag{3.8}
$$

  Using the property of eq. (3.7) this composition of maps is expressed in the following way

$$
z_3 = g(z_2) = g(e^{:f_1(z_1):} z_1) = e^{:f_1(z_1):} g(z_1) = e^{:f_1(z_1):} e^{:f_2(z_1):} z_1 \; .
\tag{3.9}
$$

  This equation illuminates the somewhat un–intuitive result that a succession of Lie operators can be expressed in the initial coordinates by reverting the order of the operators. This property is needed in the construction of maps as a succession of elements. From this property the following relation is derived

$$
e^{:g:} e^{:f:} e^{-:g:} = e^{:e^{:g:} f:}
\tag{3.10}
$$

  which is the analogue of the similarity transformation in linear matrix algebra.

- **The Campbell–Baker–Hausdorf theorem**. The concatenation of two exponential Lie operators can be expressed by another exponential Lie operator,

$$e^{:f_2:}e^{:f_1:} = e^{:f:} \tag{3.11}$$

with the generator f given by the infinite series

$$f = f_2 + f_1 + [f_2, f_1] + ... \tag{3.12}$$

Higher order terms are complicated and not discussed here. The proof of this theorem is given in [16]. In practice, this formula is of interest in those cases where f_1 and f_2 are small and the series converges rapidly.

3.2 The one turn map

The one turn map of a circular accelerator is the set of functions that relate the initial coordinates of the particle to the final coordinates after one turn. The one turn map is given by the composition of successive element maps in the form

$$\mathcal{M} = M_{N+1}e^{:h_N:}M_N e^{:h_{N-1}:}\cdots e^{:h_2:}M_2 e^{:h_1:}M_1 \, , \tag{3.13}$$

where the M_n are the maps corresponding to the linear elements and the $h_n = h_n(x_n, y_n)$ are the kick Hamiltonians of the non–linear thin lenses at the longitudinal coordinate $s = s_n$. Using the properties of the exponential Lie operator $\mathcal{M}$ can be written as a function of the initial coordinates by reverting the order:

$$\mathcal{M} = M_1 e^{:h_1:}M_2 e^{:h_2:}\cdots e^{:h_{N-1}:}M_N e^{:h_N:}M_{N+1} \tag{3.14}$$

taking $\overline{M_n} = M_1 M_2 ... M_n$, inserting identities of the form $M_n^{-1}M_n$ and using the similarity relation this equation transforms into:

$$\mathcal{M} = e^{:\overline{M}_1 h_1:}e^{:\overline{M}_2 h_2:}\cdots e^{:\overline{M}_{N-1} h_{N-1}:}e^{:\overline{M}_N h_N:}\overline{M}_{N+1} \tag{3.15}$$

The linear one turn map is $\overline{M}_{N+1}$. Since $\overline{M}_{N+1}$ is a linear, symplectic and stable operator there exists a linear change of coordinates that transforms this operator into a pure rotation. This is expressed by the similarity transformation

$$\overline{M}_{N+1} = ARA^{-1} \, , \tag{3.16}$$

where A represents the transformation and R the rotation. By inserting identities of the form AA^{-1} in eq. (3.15) The one turn map can be expressed as

$$\mathcal{M} = A^{-1}e^{:A\overline{M}_1 h_1:}e^{:A\overline{M}_2 h_2:}\cdots e^{:A\overline{M}_{N-1} h_{N-1}:}e^{:A\overline{M}_N h_N:}RA \tag{3.17}$$

In the following we will work in the new frame where the linear one turn map is a pure rotation. The total one turn map in the new frame will be represented by the same symbol $\mathcal{M}$. Using eq. (3.7) $\mathcal{M}$ is written in the form

$$\mathcal{M} = e^{:\tilde{h}_1:}e^{:\tilde{h}_2:}\cdots e^{:\tilde{h}_N:}R \tag{3.18}$$

where $\tilde{h}_n$ are the functions $h_n(x_n, y_n)$ written in terms of the eigencoordinates of the linear motion at the longitudinal location $s = s_n$. Assuming that there is no coupling present x_n and y_n are given by

$$x_n = \sqrt{2\beta_{xn}J_x}\cos(\phi_x + \phi_{xn}) \tag{3.19}$$

$$y_n = \sqrt{2\beta_{yn}J_y}\cos(\phi_y + \phi_{yn}) \tag{3.20}$$

where β_{zn}, ϕ_{zn} are the beta function and the phase advance at the location $s = s_n$. J_z and ϕ_z are the action–angle variables defined by the initial conditions. Comparing to eqs. (2.8) and (2.9) J_z corresponds to the transverse emittance divided by two.

Using the Campbell–Baker–Hausdorf theorem (see section 3.1), eq. (3.18) simplifies to

$$\mathcal{M} = e^{:h:}R \tag{3.21}$$

Assuming that the $\tilde{h}_n$ are small, h can be approximated by

$$h = \sum_{n=1}^{N}\tilde{h}_n + \sum_{n,m<n}^{N}[\tilde{h}_m, \tilde{h}_n] + \cdots \tag{3.22}$$

In the following only first order in $\tilde{h}_n$ are kept, i.e. the second summation of the right hand side of eq. (3.22) will be neglected. Using eqs. (2.15), (3.19) and (3.20), h can be expanded as:

$$h = \sum_{jklm} h_{jklm}(2J_x)^{\frac{j+k}{2}}(2J_y)^{\frac{l+m}{2}}e^{-i[(j-k)(\phi_x+\phi_{x_0})+(l-m)(\phi_y+\phi_{y_0})]} \tag{3.23}$$

where h_{jklm} are the Hamiltonian coefficients containing the contributions from all the multipoles of order $n = j+k+l+m$, being normal multipoles (B_n) if $(l+m)$ is an even number, or skew multipoles (A_n) if $(l+m)$ is an odd number. For example the Hamiltonian terms coming from normal sextupoles are: h_{3000}, h_{1200} and h_{2100}. In particular h_{3000} is given by the following summation over the existing sextupoles

$$h_{3000} = -\frac{q}{24p}\sum_i L_i B_{3i}\beta_{xi}^{\frac{3}{2}}e^{-i3\phi_{xi}} \tag{3.24}$$

3.3   Normal Form

For a non–linear map such as eq. (3.21), the idea of Normal Form is to look for a change of coordinates that shapes the map into a simpler form. Generally, the simplest form is an amplitude dependent rotation, i.e. a rotation in the phase space whose angle depends on the oscillation amplitude of the particle. The change of coordinates is represented by a similarity transformation of the one turn map, written as

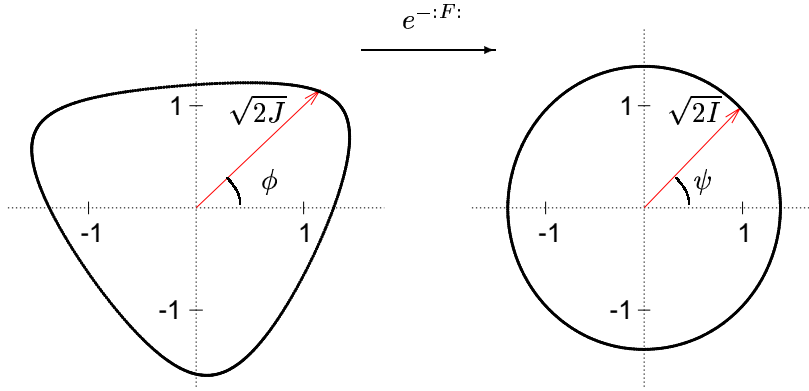$$e^{-:F:}e^{:h:}R\,e^{:F:} \tag{3.25}$$

Figure 3.1: Normalized phase space portraits in the initial coordinates (left) and in the Normal Form coordinates (right). The unit of the axis is $0.5\sqrt{mm}$.

where F is the generating function for the transformation. Figure 3.1 shows a simulated tracking example of this kind of transformation. In the left part the phase space trajectory of a particle in presence of strong sextupolar fields is shown. For this case the generating function F was numerically computed and the data were transformed by applying $e^{-:F:}$. The trajectory after the transformation (in the Normal Form coordinates) is shown in the right part of the figure 3.1. The one turn map in the Normal Form coordinates is an amplitude dependent rotation represented by $e^{:H(I):}R$, where $H(I)$ is a function that depends only on the action variables and not on the phases and R is the rotation matrix. Equating this to eq. (3.25) gives

$$e^{-:F:}e^{:h:}Re^{:F:} = e^{:H(I):}R \tag{3.26}$$

Multiplying the l.h.s. of the equation by $R^{-1}R$ and using eq. (3.10) it becomes

$$e^{-:F:}e^{:h:}e^{:RF:}R = e^{:H(I):}R \tag{3.27}$$

Using the Campbell–Baker–Hausdorf up to first order in F, h and $H(I)$, eq. (3.27) is expressed as

$$(1 - R)F + H = h \tag{3.28}$$

and the formal solution of this equation is ([17], [18] or [19]):

$$F = \frac{1}{(1 - R)}(h - \overline{h}) \tag{3.29}$$

$$H = \overline{h} \tag{3.30}$$

where $\overline{h}$ represents the average of h over the phase coordinates ϕ_x and ϕ_y. When the denominator $(1 - R)$ of eq. (3.29) takes values close to zero F diverges and Normal Form cannot be applied. In these cases the motion is not regular.

Introducing the expansion of h from eq. (3.23) in eq. (3.29) the generating function is expressed in the form

$$F = \sum_{jklm} f_{jklm} (2I_x)^{\frac{j+k}{2}} (2I_y)^{\frac{l+m}{2}} e^{-i[(j-k)(\psi_x+\psi_{x_0})+(l-m)(\psi_y+\psi_{y_0})]} \quad (3.31)$$

The generating function terms f_{jklm} are related to the h_{jklm} by the following relation,

$$f_{jklm} = \frac{h_{jklm}}{1 - e^{-i2\pi[(j-k)Q_x+(l-m)Q_y]}} \quad (3.32)$$

where Q_x and Q_y are the horizontal and vertical tunes. f_{jklm} diverges when

$$(j-k)Q_x + (l-m)Q_y = p2\pi \; ,$$

being p any integer. This situation is known as a resonance and is avoided during normal operation of accelerators. The label of the resonance is (n_1, n_2), being $n_1 = (j-k)$ and $n_2 = (l-m)$. Every generating function term or, equivalently, Hamiltonian term is associated to certain resonance. For this reason these terms are generally known as **resonance driving terms**.

3.4   The non–linear motion and its spectrum

The relation between the action angle variables $(J_x, \phi_x, J_y, \phi_y)$ and the Courant–Snyder variables $(\hat{x}, \hat{p}_x, \hat{y}, \hat{p}_y)$ is given by the formula (z stands for x or y):

$$\hat{z} = \sqrt{2J_z} \cos(\phi_z + \phi_{z0}) \quad (3.33)$$
$$\hat{p}_z = -\sqrt{2J_z} \sin(\phi_z + \phi_{z0}) \quad (3.34)$$

where ϕ_{z0} is the initial phase. It is convenient to use the resonance basis $(h_x^+, h_x^-, h_y^+, h_y^-)$ defined by the relations:

$$h_z^{\pm} = \hat{z} \pm i\hat{p}_z = \sqrt{2J_z} e^{\mp i(\phi_z+\phi_{z0})} \quad (3.35)$$

The transformation to the new set of Normal Form canonical coordinates $(\zeta_x^+, \zeta_x^-, \zeta_y^+, \zeta_y^-)$ is given by the operator $e^{-:F:}$, where F is taken from eq. (3.29), and is expressed as

$$\zeta_z^{\pm} = \sqrt{2I_z} e^{\mp i(\psi_z+\psi_{z0})} = e^{-:F:} h_z^{\pm} \quad (3.36)$$

where I_z is the invariant of the motion in the new frame. By construction the one–turn map in Normal Form coordinates is an amplitude dependent rotation. Therefore the motion in these coordinates as function of the turn number N are given by

$$\zeta_z^{\pm}(N) = \sqrt{2I_z} e^{\mp i(2\pi\nu_z N+\psi_{z0})} \quad (3.37)$$

where ν_z are the tunes including the amplitude dependent detuning. Using the two previous equations the turn–by–turn motion in the normalized coordinates is obtained. The evolution after N turns of the linearly normalized horizontal variable is expressed in the form

$$
\begin{aligned}
h_x^-(N) \;=\; & \sqrt{2I_x}\,e^{i(2\pi\nu_x N+\psi_{x_0})} \;-\; \\
& 2i\sum_{jklm} j\,f_{jklm}(2I_x)^{\frac{j+k-1}{2}}(2I_y)^{\frac{l+m}{2}} \;\times\; \\
& e^{i[(1-j+k)(2\pi\nu_x N+\psi_{x_0})+(m-l)(2\pi\nu_y N+\psi_{y_0})]}
\end{aligned}
\tag{3.38}
$$

where the factors f_{jklm} are the generating function terms. Note that by evaluating this equation at $N = 0$ the relation between (J,ϕ) and (I,ψ) is obtained. Eq. (3.38) describes the motion of the particle in presence of non–linearities. Each Hamiltonian coefficient h_{jklm} introduces a spectral line proportional to its amplitude. The FFT of the turn by turn signal $h_x^-(N)$ can be used to measure these Hamiltonian coefficients approximately (see [6]). To construct the signal $h_x^-(N)$ defined in eq. (3.35) both the position and the momentum are needed. In a real machine the position are available from the beam position monitors (BPM). It is however possible to reconstruct the momentum using two nearby BPMs. If the phase advance between the BPMs is exactly $\pi/2$ the first BPM gives the position $\hat{z}$ and the second BPM the momentum $\hat{p}_z$ as can be seen from eq. (3.34). Otherwise the data from the second BPM is linearly transformed using the data from the first BPM to achieve the $\pi/2$ of phase advance. In figure 3.4 an example corresponding to the SPS in presence of strong sextupoles of the amplitude of the Fourier spectrum of the horizontal signal $h_x^-(N)$ is presented. The spectral line with frequency $-2Q_x$, (-2, 0), is proportional to the term h_{3000}, the line with frequency $2Q_x$, (-2, 0), is proportional to the term h_{1200} and the line with zero frequency, (0,0), is proportional to the term h_{2100}.
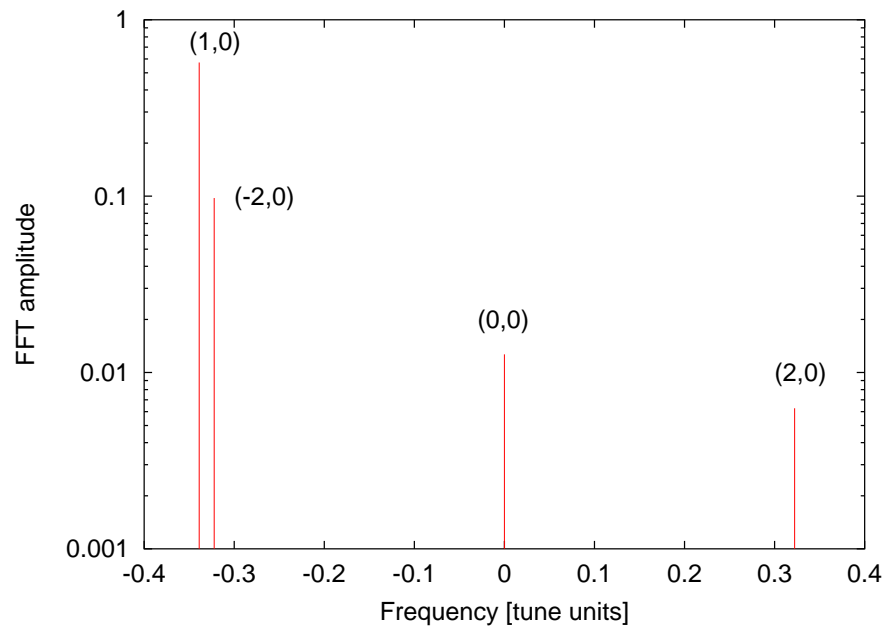
Figure 3.2: Amplitude of Fourier spectrum of the horizontal signal $h_x^-(N)$ for the SPS in presence of strong sextupolar fields. The label (m,n) attached to the spectral lines means that the frequency of that line is $mQ_x + nQ_y$.

Chapter 4

Spectral response to particle distributions

4.1 Analytical study

In section 3.4 the relation between the spectral lines of the single particle motion and the resonance driving terms was established by means of $h_x^-(N)$. In a real machine the BPMs are used to record the turn–by–turn transverse position of the centroid of the beam. Therefore the equivalent relation to that given by $h_x^-(N)$ has to be found between the spectral lines of the motion of the centroid and the resonance driving terms. To derive such relation it will be assumed that the coordinates of the centroid are given by averaging over a Gaussian distribution of particles that do not interact between them. The most important processes that affect the centroid motion are the decoherence processes, i.e. when all the particles do not oscillate with the same frequency or tune. The two main sources of tune spread in an accelerator are amplitude detuning and chromaticity.

The amplitude detuning is caused by the presence of non–linear magnetic fields. The horizontal and vertical tunes are functions of the betatronic amplitudes of the particles. Thus particles with different oscillation amplitudes have also different tunes. This causes the decoherence of the beam. The oscillations of the centroid are completely damped after certain number of turns. Simulation data showing this effect for an SPS model with strong sextupoles is plotted in figure 4.1.

The tunes of the particle also depend on its momentum deviation. The parameter used to quantify this dependence is the chromaticity Q', defined as

$$Q_z' = \frac{\partial Q_z}{\partial \delta} \ ,$$

(4.1)

where z stands for x or y and $\delta = (p - p_0)/p_0$ is the relative momentum deviation. This dependence of the tune on the energy of the particle is explained by the fact that the more energetic particles are less focused by the quadrupoles and vice versa. In addition the energy of off–momentum particles performs harmonic oscillations

19

around the reference energy due to the effect of the radio frequency cavities. The frequency of these oscillations is the synchrotron tune Q_s. Therefore the transverse tunes are modulated with the synchrotron tune with a modulation amplitude given by the chromaticity. The phase of this modulation is equally distributed between 0 and 2π among the particles of a centered beam. Simulation data showing the effect of chromaticity in the centroid motion is plotted in figure 4.6.

In this chapter the spectrum of the motion of the centroid of the beam is studied assuming Gaussian particle distributions and including amplitude detuning and chromaticity. This study will allow to relate the lines of the Fourier spectrum of the centroid turn–by–turn data to the non–linearities of the machine. This is the generalization of eq. (3.38), for single particle, to particle distributions. The quantitative dependence of the tune on the different phase space variables that will be used in the subsequent analysis is given in the next section.

4.1.1   Tune dependence and bunch densities

Sextupoles and octupoles introduce a linear dependence of the tunes ν_x and ν_y with respect to the horizontal and vertical invariants I_x and I_y [20], introduced in eq. (3.36). Note that this effect is of first order in the strength of the octupoles and of second order in the strength of the sextupoles. Higher multipoles introduce higher powers of the invariants but it is assumed here that these contributions are negligible. This could be expressed as follows:

$$\nu_x = Q_x + \nu'_{xx}2I_x + \nu'_{xy}2I_y$$
$$\nu_y = Q_y + \nu'_{yx}2I_x + \nu'_{yy}2I_y \tag{4.2}$$

where the ν' are constant factors defined as

$$\nu'_{xx} = \frac{\partial \nu_x}{\partial \epsilon_x} \quad \nu'_{xy} = \frac{\partial \nu_x}{\partial \epsilon_y}$$
$$\nu'_{yx} = \frac{\partial \nu_y}{\partial \epsilon_x} \quad \nu'_{yy} = \frac{\partial \nu_y}{\partial \epsilon_y} \tag{4.3}$$

with $\epsilon_z = 2I_z$ and $\nu'_{xy} = \nu'_{yx}$.

Off–momentum particles will experience an additional tune oscillation given by the expressions [21]:

$$\Delta\nu_x = \frac{Q'_x\delta}{\pi Q_s N} \cos(\pi Q_s N + \psi_s) \sin(\pi Q_s N)$$
$$\Delta\nu_y = \frac{Q'_y\delta}{\pi Q_s N} \cos(\pi Q_s N + \psi_s) \sin(\pi Q_s N) \tag{4.4}$$

where Q_s is the longitudinal or synchrotron tune, ψ_s is the initial phase, δ is the momentum deviation, Q'_x and Q'_y are the horizontal and vertical chromaticities and N is the turn number.

Assuming Gaussian distributions in the three planes with the centroids of the initial transverse distributions off–centered with the amplitudes $\overline{A}_x$ and $\overline{A}_y$, in units of the sigma of the corresponding distribution, and a centered Gaussian distribution in the longitudinal plane, the densities are given by:

$$\rho_x(I_x, \psi_x) = \frac{1}{2\pi} e^{-\frac{1}{2}(2I_x + \overline{A}_x^2 - 2\overline{A}_x \sqrt{2I_x} \cos \psi_x)} \tag{4.5}$$

$$\rho_y(I_y, \psi_y) = \frac{1}{2\pi} e^{-\frac{1}{2}(2I_y + \overline{A}_y^2 - 2\overline{A}_y \sqrt{2I_y} \cos \psi_y)} \tag{4.6}$$

$$\rho_s(\delta, \psi_s) = \frac{\delta}{2\pi\sigma_s^2} e^{-\delta^2/(2\sigma_s^2)} \tag{4.7}$$

where $\sqrt{2I_x}$ and $\sqrt{2I_y}$ are expressed in units of the sigma of the corresponding distribution and σ_s is the sigma of the longitudinal distribution. Each sigma corresponds to the square root of the emittance in the respective plane.

4.1.2 The centroid motion and its spectrum

The centroid position and momentum are computed by averaging over the bunch distribution. The turn–by–turn motion of each particle $h_x^-(N)$ is given by eq. (3.38) as a function of his transverse amplitudes and initial phases. The contributions of the amplitude detuning and the chromaticity to the tunes are introduced in that expression. At every turn N the centroid normalized horizontal coordinate is given by the following expression,

$$\overline{h_x^-}(N) = \int_0^\infty dI_x \int_0^\infty dI_y \int_0^\infty d\delta \int_0^{2\pi} d\psi_x \int_0^{2\pi} d\psi_y \int_0^{2\pi} d\psi_s \, \rho_x(I_x, \psi_x) \times$$
$$\rho_y(I_y, \psi_y)\rho_s(\delta, \psi_s)h_x^-(N) \tag{4.8}$$

This integral involves the six variables of the phase space, the densities were introduced in the previous section and $h_x^-(N)$ is given by eq. (3.38) including amplitude detuning and chromaticity. In the appendix A.1 it is described how to solve four of these integrals. It does not seem possible to integrate over I_x and I_y. $\overline{h_x^-}(N)$ can be re–expressed in terms of the remaining integrals as

$$\overline{h_x^-}(N) = L_{1100}(N) - 2i \sum_{jklm} jf_{jklm}L_{(j+k-1)(1-j+k)(l+m)(m-l)}(N) \tag{4.9}$$

where L_{nmlk} are defined by

$$L_{nmlk}(N) = \int_0^\infty dI_x \int_0^\infty dI_y (2I_x)^{n/2}(2I_y)^{l/2} e^{-\frac{1}{2}(2I_x + \overline{A}_x^2 + 2I_y + \overline{A}_y^2)} \times$$
$$I_m(\overline{A}_x \sqrt{2I_x})I_k(\overline{A}_y \sqrt{2I_y})e^{i2\pi(m\nu_x + k\nu_y)N - 2\gamma_{mk}^2 \sin^2(\pi Q_s N)} \tag{4.10}$$

where I_n represents the modified Bessel function of order n, $\gamma_{mk} = (mQ_x' + kQ_y')\sigma_s/Q_s$ contains the effect of chromaticity and ν_x and ν_y do contain only the effect of amplitude detuning.

It has been already mentioned that to measure the resonance terms we have to perform a Fourier analysis of the data. For this reason the Fourier transformation of the centroid turn–by–turn motion, given by eq. (4.9), has to be computed. The Fourier transformation of $\overline{h_x^-}(N)$ is represented by $H_x^-(w)$. Since the Fourier transformation is a linear operator each term of the r.h.s. of eq. (4.9) gives a contribution to $H_x^-(w)$, this is expressed by

$$H_x^-(w) = \int dN \, \overline{h_x^-}(N) \, e^{-iwN} \equiv H_{x,tune}^-(w) + \sum_{jklm} H_{x,jklm}^-(w) \qquad (4.11)$$

The steps to solve this integral are described in the appendix A.2. Notice that by solving this integral a Dirac Delta function appears and this permits to integrate over I_x. Nevertheless it is not possible to solve analytically the integral over I_y. The different terms of the r.h.s. of eq. (4.11) are re–expressed as

$$
\begin{aligned}
H_{x,tune}^-(w) &= \mathcal{A}_{x,tune}^-(w) \, e^{-\gamma_{10}^2} I_0(\gamma_{10}^2) + & (4.12) \\
&\quad \sum_{q=1}^{\infty} e^{-\gamma_{10}^2} I_q(\gamma_{10}^2) [\mathcal{A}_{x,tune}^-(w + q2\pi Q_s) + \mathcal{A}_{x,tune}^-(w - q2\pi Q_s)] \\
H_{x,jklm}^-(w) &= \mathcal{A}_{x,jklm}^-(w) \, e^{-\gamma_{(1-j+k)(m-l)}^2} I_0(\gamma_{(1-j+k)(m-l)}^2) + \\
&\quad \sum_{q=1}^{\infty} e^{-\gamma_{(1-j+k)(m-l)}^2} I_q(\gamma_{(1-j+k)(m-l)}^2) \times \\
&\quad [\mathcal{A}_{x,jklm}^-(w + q2\pi Q_s) + \mathcal{A}_{x,jklm}^-(w - q2\pi Q_s)] & (4.13)
\end{aligned}
$$

where the functions $\mathcal{A}_{x,tune}^-(w)$ and $\mathcal{A}_{x,jklm}^-(w)$ are defined in eqs. (A.21) and (A.22) and still contain an integral over the coordinate I_y. The functions $\mathcal{A}_{x,tune}^-(w)$ and $\mathcal{A}_{x,jklm}^-(w)$ are single peak distributions with their maximums close to the frequencies ν_x and $(1-j+k)\nu_x + (m-l)\nu_y$ respectively. Their amplitudes contain the generating function terms and the reduction factor $|(1-j+k)\nu_{xx}' + (m-l)\nu_{yx}'|$. These factors are due to the decoherence and increase the difficulty to measure the resonance terms since they reduce the signal of interest. The functions $H_{x,tune}^-(w)$ and $H_{x,jklm}^-(w)$ are equal to $\mathcal{A}_{x,tune}^-(w)$ and $\mathcal{A}_{x,jklm}^-(w)$ when the chromaticity is zero. From their expressions one can read that the effect of chromaticity is to add an infinite number of sidebands at $\pm q2\pi Q_s$ from every line. The shape of the sidebands is the same as the one of the main peak and their amplitudes decrease as q increases.

These expressions represent the furthest analytical solution for the general case. The remaining integral over I_y should be done numerically. Nevertheless simpler expressions are found when considering only one transverse dimension or when looking at special spectral lines.

One transverse dimension

When only one of the transverse planes is relevant analytical expressions of the functions $\mathcal{A}^-_{x,tune}(w)$ and $\mathcal{A}^-_{x,jklm}(w)$ can be achieved. Considering only the horizontal plane, the integrals over I_y from eqs. (A.21) and (A.22) are dropped and I_y is set to zero, resulting in

$$\mathcal{A}^-_{x,tune}(w) = \frac{1}{|\nu'_{xx}|}\sqrt{2I_x(w)}e^{-\frac{1}{2}(2I_x(w)+\overline{A}^2_x)}\mathrm{I}_1\left(\overline{A}_x\sqrt{2I_x(w)}\right) \quad (4.14)$$

$$\mathcal{A}^-_{x,jk00}(w) = -\frac{2ijf_{jk00}}{|(1-j+k)\nu'_{xx}|}(2I_x(w))^{(j+k-1)/2} \times$$
$$e^{-\frac{1}{2}(2I_x(w,I_y)+\overline{A}^2_x)}\mathrm{I}_{(1-j+k)}\left(\overline{A}_x\sqrt{2I_x(w)}\right) \quad (4.15)$$

$$2I_x(w) = \frac{1}{(1-j+k)\nu'_{xx}}(w/2\pi - (1-j+k)\nu_{x0}) \quad (4.16)$$

To obtain the total $H^-_x(w)$, with the chromaticity sidebands, the $\mathcal{A}^-(w)$ of eqs. (4.12) and (4.13) is replaced by these given above. To compare the former $\mathcal{A}^-_{x,jk00}$ to the single particle case the Fourier spectrum of the motion of a single particle, see eq. (3.38), is given with a similar notation,

$$h^-_{x,tune}(w) = \overline{A}_x\delta_{Dirac}(w/2\pi - \nu_x) \quad (4.17)$$

$$h^-_{x,jk00}(w) = -2ijf_{jk00}(\overline{A}_x)^{(j+k-1)/2}\delta_{Dirac}(w/2\pi - (1-j+k)\nu_x)$$

where δ_{Dirac} is the Dirac delta function and the oscillation amplitude of the single particle is $\sqrt{2I_x} = \overline{A}_x$. It is observed that each spectral line of eqs. (4.17) becomes a distribution divided by the factor $|(1-j+k)\nu'_{xx}|$ due to having taken into account the particle distribution and the amplitude detuning. The spectrum is usually normalized to the tune line (1,0) to easily compare to experiments. The normalized amplitude of the line $(m,0)$ from particle distributions is reduced by a factor of $|m|$ compared to the single particle case. These factors are called decoherence factors and are described below.

Decoherence factors

Both in the two–dimensional and the one–dimensional calculations reduction factors of the spectral lines appear due to the amplitude detuning. These factors depend only on the frequency of the spectral line and the amplitude detuning coefficients. The decoherence factor corresponding to the horizontal spectral line (m,n) is defined as

$$\left| m + n\frac{\nu'_{yx}}{\nu'_{xx}} \right| \quad (4.18)$$

and represents the reduction factor of the normalized spectral line of a decohered signal when compared to the single particle case. In particular, for the one dimensional case the decoherence factor corresponding to the spectral line $(m,0)$ is $|m|$.

The line with zero frequency

The generating term f_{jklm} will be attached to a zero frequency line in the horizontal plane when $1-j+k = 0$ and $m-l = 0$. Calculating the terms $H^-_{x,j(j-1)mm}$, which fulfill the former conditions, is much easier since they are not affected neither by amplitude detuning nor by chromaticity. Notice that they are not a distribution since they are only defined at $w = 0$. Starting from eq. (A.4) and doing the integrals over the transverse phases one obtains

$$
\begin{aligned}
H^-_{x,j(j-1)mm} &= -2ij f_{j(j-1)mm} \int_0^\infty dI_x \int_0^\infty dI_y (2I_x)^{(j-1)} (2I_y)^m \times \\
&\quad e^{-\frac{1}{2}(2I_x + \overline{A}_x^2 + 2I_y + \overline{A}_y^2)} I_0(\overline{A}_x \sqrt{2I_x}) I_0(\overline{A}_y \sqrt{2I_y}).
\end{aligned} \tag{4.19}
$$

This integral can be exactly computed for all $j > 0$ and $m \geq 0$ leading to hypergeometric functions. For $m = 0$ these hypergeometric functions are simply polynomials of order $2(j-1)$ in $\overline{A}_x$. We show the cases $j = 2$, $m = 0$ and $j = 3$, $m = 0$ which are related to sextupolar and decapolar fields respectively:

$$
\begin{aligned}
H^-_{x,2100} &= -4i f_{2100}(2 + \overline{A}_x^2) \\
H^-_{x,3200} &= -6i f_{3200}(8 + 8\overline{A}_x^2 + \overline{A}_x^4)
\end{aligned} \tag{4.20}
$$

Note that the other spectral lines vanish for $\overline{A}_x = 0$, see (4.15), and that the single particle spectrum of eq. (3.38) is completely flat for a zero oscillation amplitude. Contrary to these cases the (0,0) line exists even for $\overline{A}_x = 0$ when considering particle distributions. To compare to the single particle case the contributions from the sextupoles and the decapoles to the (0,0) line of the single particle spectrum are given by

$$
\begin{aligned}
h^-_{x,2100} &= -4i f_{2100} \overline{A}_x^2 \\
h^-_{x,3200} &= -6i f_{3200} \overline{A}_x^4
\end{aligned} \tag{4.21}
$$

where the oscillation amplitude of the single particle is $\sqrt{2I_x} = \overline{A}_x$. Note that for large values of $\overline{A}_x$ eqs. (4.20) and (4.21) tend to give the same results, contrary to other spectral lines where the decoherence factors appear for any $\overline{A}_x$.

4.1.3 Peak widths

The width of the different lines is an important parameter since its inverse is proportional to the decoherence time of the line. For the following calculation it is assumed that the sidebands introduced by the chromaticity do not mix with the principal line. The width is estimated by evaluating the standard quadratic deviation of the corresponding distribution $\mathcal{A}_x^-(w)$:

$$
\sigma^2_{jklm} = <w^2> - <w>^2 = \frac{\int dw \, w^2 \mathcal{A}^-_{x,jklm}(w)}{\int dw \mathcal{A}^-_{x,jklm}(w)} - \left(\frac{\int dw \, w \mathcal{A}^-_{x,jklm}(w)}{\int dw \mathcal{A}^-_{x,jklm}(w)}\right)^2 \tag{4.22}
$$

In the general case these integrals have to be done numerically but considering only one transverse dimension it is possible to compute them analytically. In table 4.1 the widths of the most important low order lines are shown. A quasi–linear increase of the width with the order of the line is observed.

	$j + k - 1$	$1 - j + k$	σ_{jk00}
Tune Line	1	1	$2\nu'_{xx}\sqrt{2 + \overline{A}_x^2}$
Sextupolar Lines	2	± 2	$4\nu'_{xx}\sqrt{3 + \overline{A}_x^2}$
Octupolar Lines	3	± 3	$6\nu'_{xx}\sqrt{4 + \overline{A}_x^2}$

Table 4.1: Width of the most important low order lines in the horizontal spectrum considering only a horizontal distribution.

4.1.4 Surviving lines

We have seen that the decoherence affects in a different way each line. The main reason is that they have different amplitude detunings, i.e. the spectral line (m,n) which has the tune $\nu = m\nu_x + n\nu_y$ has an amplitude detuning expressed by:

$$\Delta\nu = (m\nu'_{xx} + n\nu'_{yx})2I_x + (m\nu'_{xy} + n\nu'_{yy})2I_y \ .$$

If the terms in brackets cancel out, this line will have no detuning and, as happens to the line (0,0), it will not decohere. This may give a chance to measure certain high order lines which in presence of filamentation are strongly decreased by the decoherence factor.

4.2 Simulations

This section is devoted to comparing some of the analytical expressions derived in section 4.1 to computer simulations. In the previous section the Fourier spectrum of the centroid of a Gaussian beam was described analytically taking into account the amplitude detuning and the chromaticity. In the general case of considering the two transverse dimensions it was not possible to solve analytically all the integrals involved in the calculations. In the simpler case of only one transverse dimension analytical expressions were obtained from the Fourier spectrum. Nevertheless when there is chromaticity and there is no amplitude detuning analytical expressions could also be inferred in the two dimensional case. In order to verify the different predictions two simulations have been performed. The first one contains amplitude detuning but not chromaticity and the second one contains only chromaticity. To do both simulations a common model of an operating accelerator has been used: the Super Proton Synchrotron (SPS) at CERN. A detailed description of the SPS is given in chapter 6.

In the following sections the two computer simulations are described. The results from the analysis of the data has been compared to the analytical expressions obtained in the previous section.

4.2.1   Amplitude detuning

Description of the simulation

To obtain the horizontal evolution of the centroid a large number of particles having an off–center Gaussian distribution in the horizontal phase space have been tracked. The turn–by–turn position of the centroid is given by the average position of the particles. The program used for the single particle tracking was SixTrack [23]. This program simulates the trajectory of a particle all around the accelerator. Each element is described using a symplectic map, i.e. it preserves the area in the phase space. The program used to compute the Fourier transform of the data was SUS-SIX [24] which contains the recent developments [5] that allow a precise determination of the spectral lines. Particle distributions are considered neither in the vertical nor in the longitudinal plane. Amplitude detuning was created by introducing the extraction sextupoles in the linear lattice. The first four extraction sextupoles were powered to +30 A and the following four extraction sextupoles were powered to –30 A as shown in figure 6.2. All the simulated particles have the energy of the reference particle ($\delta = 0$), therefore chromaticity is not an issue (for the formulas $Q' = 0$). The horizontal sigma of the beam distribution is 0.18 $mm/\sqrt{\beta_x}$, where $\beta_x = 103\ m$. The initial offset of the Gaussian distribution is represented by the quantity $\overline{A_x}$ introduced in the previous chapter. In the experiments a single dipole kick is applied to displace the beam from the center. The simulation was done for various kicks ranging from 2 to 13 mm at $\beta = 103\ m$. As an illustration the simulation data for the case with a kick of 7.3 mm at the same β is shown in figure 4.1. This picture shows the typical pattern of the damped oscillation of the centroid due to beam decoherence due to amplitude detuning.

In a second illustration the Fourier spectrum of the centroid turn–by–turn data is shown in figure 4.2. The labels (m,n) attached to the different peaks mean that the frequency of that line is $m\nu_x + n\nu_y$. The tune line is the (1,0) line and its amplitude is used to normalize the spectrum. The main spectral lines arising from the sextupoles are (–2, 0), (2, 0) and (0, 0) which are proportional to the generating terms f_{3000}, f_{1200} and f_{2100} respectively. The spectral lines (–3,0) and (–1,0) come from octupoles and second order terms of the sextupoles. The line (–4,0) comes from second order terms of the octupoles and third order terms of the sextupoles. The aim of this work is to describe the spectrum up to first order on the non–linearities, therefore we focus on the tune line and the main sextupolar lines. From the figure a couple of conclusions can be drawn: the effect of considering the particle distribution causes the spectral lines to become wide distributions instead of Dirac Delta functions like in the single particle case and the line (0,0) has zero width as stated in section 4.1.2. The detailed comparison of the amplitude and
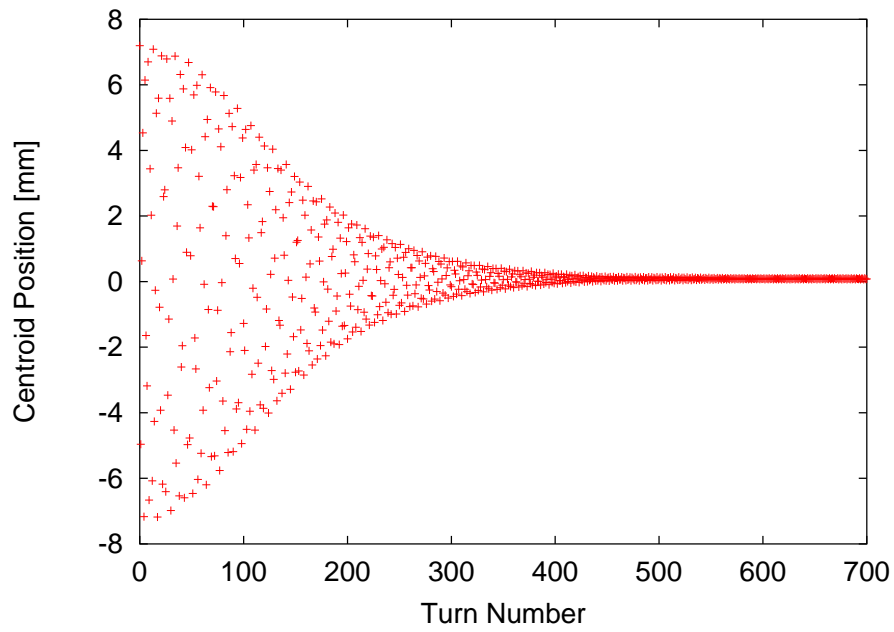
Figure 4.1: Horizontal position of the centroid of the beam versus turn number for the SPS with extraction sextupoles on.
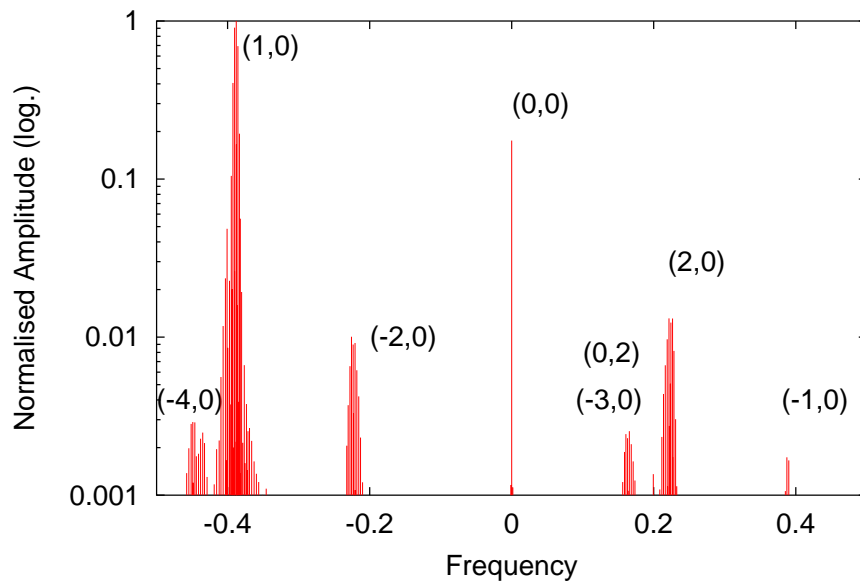

Figure 4.2: FFT spectrum of the horizontal centroid motion of the beam for the SPS with extraction sextupoles on.

shape of the spectral lines to the analytical predictions is done in the next section.

Comparison between model and simulation

In section 4.1.2 the expressions that describe the Fourier spectrum for one transverse dimension are given. The analytical expression describing the line (1,0), the tune line, is given by

$$\mathcal{H}_{x,tune}^{-}(w) = \frac{1}{|\nu'_{xx}|}\sqrt{2I_x(w)}e^{-\frac{1}{2}(2I_x(w)+\overline{A}_x^2)}\,\mathrm{I}_1\left(\overline{A}_x\sqrt{2I_x(w)}\right) \quad (4.23)$$

$$2I_x(w) = \frac{1}{\nu'_{xx}}(w/2\pi - Q_x) \quad (4.24)$$

The parameters needed for the evaluation of this expression are taken from the single particle tracking. These parameters are the horizontal tune for zero oscillation amplitude (Q_x) and the amplitude detuning (ν'_{xx}), i.e. the derivative of the horizontal tune with respect to the square of the oscillation amplitude. Both parameters were obtained by evaluating the tune of the single particle at different oscillation amplitudes and performing a fit. In figure 4.3 the tune line obtained from the Fourier transform of the simulation with the particle distribution is compared to the analytical model. The agreement between the two curves is good enough to suggest that tune measurements might be improved by fitting the predicted curve to the Fourier spectrum of measured data.

The distribution of the line (–2, 0) is given by the term $H_{x,3000}(w)$ which is obtained from eq. (4.15), giving

$$\mathcal{H}_{x,3000}^{-}(w) = -\frac{6if_{3000}}{|2\nu'_{xx}|}2I_x(w) \times$$
$$e^{-\frac{1}{2}(2I_x(w,I_y)+\overline{A}_x^2)}\mathrm{I}_2\left(\overline{A}_x\sqrt{2I_x(w)}\right) \quad (4.25)$$

$$2I_x(w) = \frac{1}{-2\nu'_{xx}}(w/2\pi + 2Q_x) \quad (4.26)$$

The parameters needed for the evaluation of these expressions are the horizontal tune (Q_x), the amplitude detuning (ν'_{xx}) and the generating term f_{3000}. The first two were already obtained above. The generating term was calculated by using the analytical expressions of section 3.3 (given the model) as well as from the FFT of single particle tracking (section 3.4), obtaining the same result. In figure 4.4 the line (–2, 0) obtained from the Fourier transform of the centroid simulation data is compared to the analytical prediction. The frequency of the peak of the curve and its width are well predicted although there is a small discrepancy in the right tail. It remains unclear whether this discrepancy comes from the simulation or from the decoherence model.

The line (0,0) was studied separately in section 4.1.2. Contrary to the previous spectral lines this one has zero width. Therefore the quantity to be compared between simulation and model is the amplitude of the line (0,0) for different kicks.
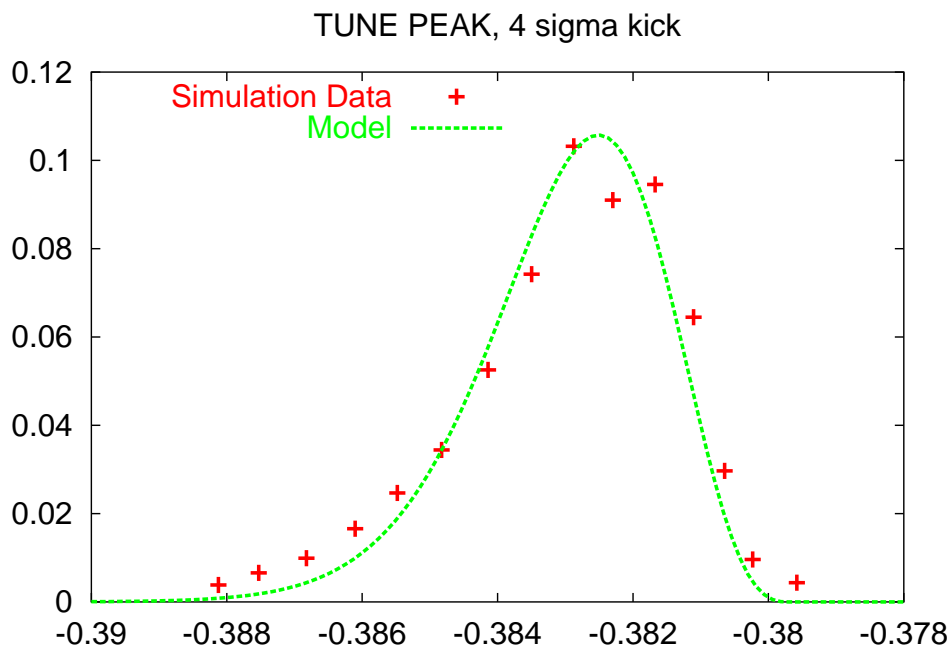
Figure 4.3: Distribution of the tune peak for model and simulation versus frequency (in tune units) for the SPS with extraction sextupoles on.

The amplitude of this spectral line as function of the kick is given by $H_{x,2100}^-$ from eq. 4.21. The amplitude of this line only depends on the generating term f_{2100}, which has been calculated in the same way as the previous term f_{3000}. In figure 4.5 the amplitude of line $(0,0)$ computed from the simulation is compared to the prediction of eq. (4.21). The agreement is excellent. It is important to notice that this line exists even when the kick is zero. This feature is not predicted from the single particle theory, eq. (3.38), it appears only when the beam distribution is considered.

The analytical expressions derived in section 4.1.2 have been compared to a computer simulation. The overall agreement is very satisfactory validating the expressions obtained for the one dimensional case. It remains unclear whether the discrepancies seen in the tails of the distributions are due to the simulation or to the model. No simulation was done for the more general case of two transverse dimensions since it requires a huge amount of CPU time. In the following section the simulation containing chromaticity is discussed.
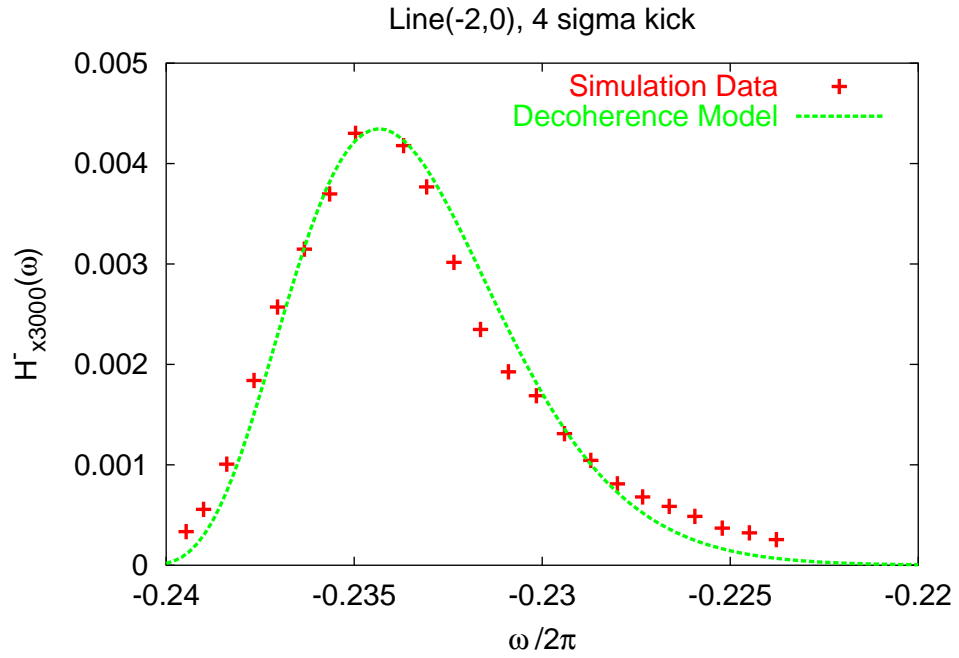
Figure 4.4: Distribution of the line (-2,0) for model and simulation against frequency for the SPS with extraction sextupoles on.
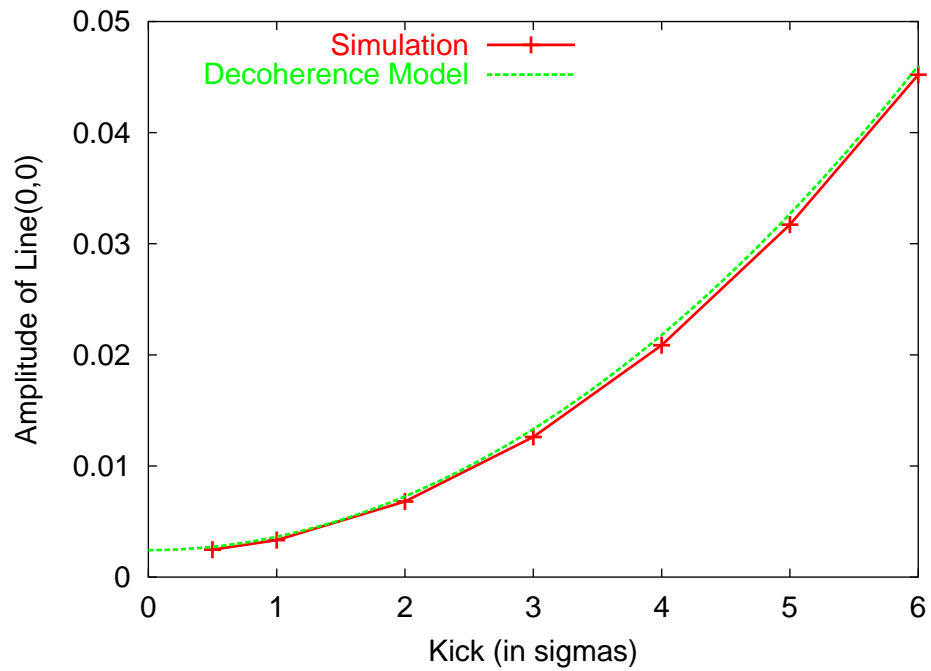

Figure 4.5: Amplitude of the line (0,0) for model and simulation versus the kick $\overline{A_x}$ in sigmas for the SPS with extraction sextupoles on.

4.2.2 Chromaticity

Description of the simulation

To perform simulations of the centroid in presence of chromaticity the program HEADTAIL [25] has been used. This program has been originally written to study the interaction of a bunch with an electron cloud over many turns. The bunch is represented by 10^5 macro–particles which are initialized with a Gaussian distribution in each of the 6 dimensions of the phase space. Each macro–particle executes betatron and synchrotron motion. The betatron motion is simulated by using the linear one–turn map of the accelerator. This feature speeds up the tracking process but discards the introduction of non–linear elements around the ring. The effect of chromaticity is also included by applying a momentum dependent rotation to each macro–particle. In order to ensure the longitudinal–transverse coupling which allows us to see synchrotron sidebands in the spectrum of the centroid motion, it is sufficient to set the chromaticity to a nonzero value. The macro–particles are tracked over 2048 turns, the position of the centroid of the vertical motion is recorded and Fourier analyzed. The parameters used for the tracking are: $Q'_y = 10.64$, $Q'_x = 0$, $Q_s = 0.00686$ and $\sigma_s = 1.62 \times 10^{-3}$. Since only the vertical motion is considered the subindex y is dropped in the following. In figure 4.6 the turn–by–turn motion of the centroid obtained in this simulation is plotted. It shows how the beam decoheres and recuperates the coherence periodically due to the chromaticity and the energy oscillations.

Comparison between the decoherence model and simulation

Since no non–linear elements were introduced in the simulation all the generating terms f_{jklm} are zero and therefore the only spectral line existing is the tune line. The effect of chromaticity on the tune line is to introduce sidebands with frequencies $\nu \pm qQ_s \ \forall q \in \mathrm{N}$ as shown in eq. (A.23), which is re–written as

$$
\begin{aligned}
H^-_{tune}(w) \quad \propto \quad & \mathcal{A}^-_{tune}(w)\,\mathrm{I}_0(\gamma_{10}^2) + \\
& \sum_{q=1}^{\infty} \mathrm{I}_q(\gamma_{10}^2)[\mathcal{A}^-_{tune}(w + q2\pi Q_s) + \mathcal{A}^-_{tune}(w - q2\pi Q_s)]
\end{aligned}
\tag{4.27}
$$

The sidebands have the same shape as the fundamental line, given by the function $\mathcal{A}^-_{tune}(w)$. There are only two parameters in eq.(4.27), the synchrotron tune, ν_s, and $\gamma_{10} = Q'\sigma_s/Q_s$. Both parameters are directly obtained from the input of the numerical simulation. Q_s determines the spacing between the sidebands and γ_{10} determines the number of relevant sidebands appearing via the factor $\mathrm{I}_q(\gamma_{10}^2)$ in front of the sideband of order q. In this simulation there was no amplitude detuning, therefore $\mathcal{A}^-_{tune}(w)$ is a Dirac delta function. Then the shape of the fundamental line and the sidebands will be a narrow peak determined by the FFT resolution. The amplitude of the sidebands from model and from simulation are being compared. To this aim the analytical envelope function is being computed and plotted with
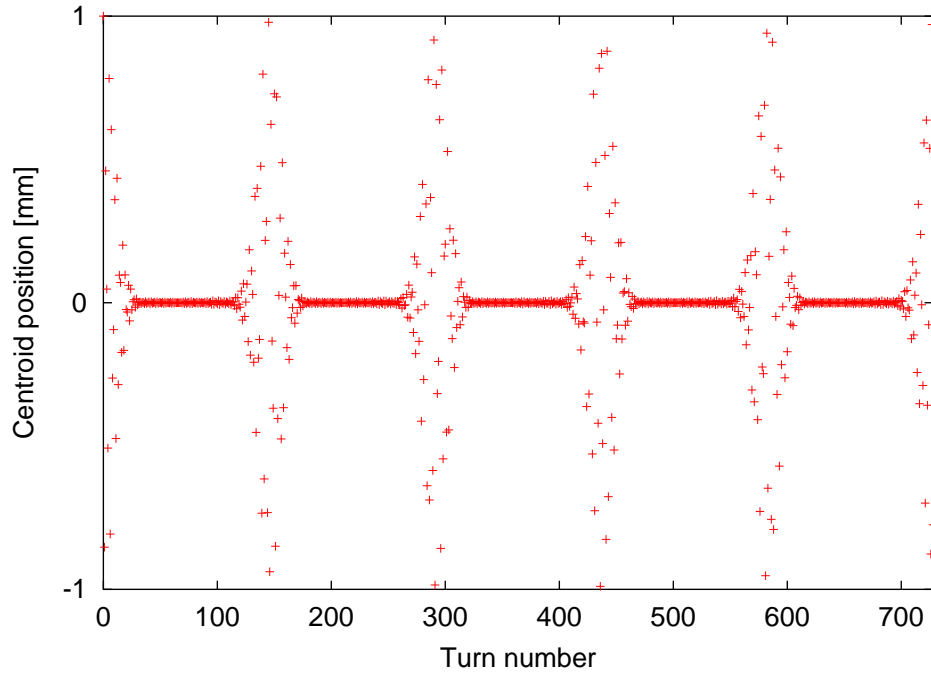
Figure 4.6: Vertical position of the centroid versus turn number for the SPS without any non–linear element.

the FFT of the simulation data. The envelope function $E(w)$ that connects all the peaks of eq. (4.27) is expressed as

$$E(w) = \mathrm{I}_{\frac{w-2\pi\nu}{2\pi Q_s}}\left(\gamma_{10}^2\right) \tag{4.28}$$

note that the variable w is in the order of the modified Bessel function. In figure 4.7 the amplitude of the FFT of the simulation data is plotted together with this envelope function. The simulation and the analytical formula are in excellent agreement.
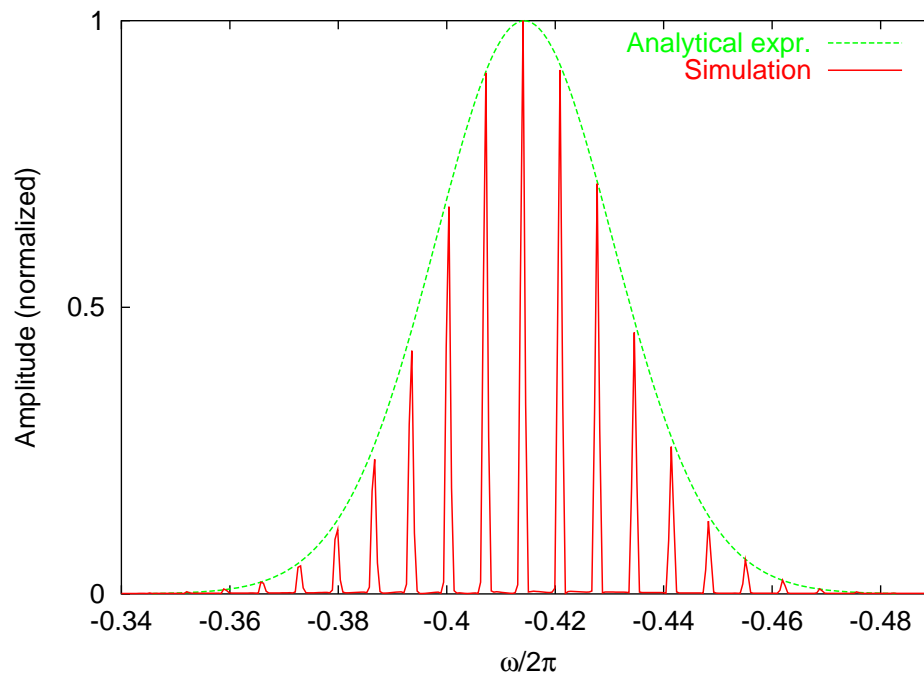
Figure 4.7: Amplitude of the FFT of the vertical centroid motion from simulation and predicted envelope function for the SPS without any non–liner element.

Chapter 5

Localization of Multipoles

The longitudinal variation around the ring of the Hamiltonian and the generating function terms are studied in this chapter. It is shown how measuring the amplitude of the different resonance driving terms along the ring allows the identification of the longitudinal positions of multipolar kicks. Therefore it is possible to identify field errors and their location. This method is of great interest for commissioning an operating an accelerator.

5.1   Longitudinal variation of resonance terms

The dependence of the one turn map on the longitudinal coordinate is studied by constructing two maps starting at two different locations (s_1 and s_2), separated by a linear section M_1 and a non-linear multipole kick $e^{:h_1:}$. The corresponding one turn maps are expressed as

$$
\begin{aligned}
\mathcal{M}^{(1)} &= M_{N+1}e^{:h_N:}M_N e^{:h_{N-1}:}\cdots e^{:h_2:}M_2 e^{:h_1:}M_1 \,, & (5.1) \\
\mathcal{M}^{(2)} &= e^{:h_1:}M_1 M_{N+1}e^{:h_N:}M_N e^{:h_{N-1}:}\cdots e^{:h_2:}M_2 \,. & (5.2)
\end{aligned}
$$

A schematic view of these two maps is shown in figure 5.1. Both maps can be expressed in their respective normalized phase space as follows

$$
\begin{aligned}
\mathcal{M}^{(1)} &= e^{:h^{(1)}:}R \,, & (5.3) \\
\mathcal{M}^{(2)} &= e^{:h^{(2)}:}R \,, & (5.4)
\end{aligned}
$$

where the respective linear one turn maps in the normalized space are the same since they are connected by a similarity transformation which preserves the rotation angle. $h^{(1)}$ and $h^{(2)}$ are obtained from eqs. (3.17) and (3.22), giving

$$
\begin{aligned}
h^{(1)} &= A_1 M_1 h_1 + A_1 M_1 M_2 h_2 + \cdots + A_1 M_1 M_2 \cdots M_N h_N \\
h^{(2)} &= A_2 M_2 h_2 + A_2 M_2 M_3 h_3 + \cdots + A_2 M_2 \cdots M_{N+1}M_1 h_1 \quad (5.5)
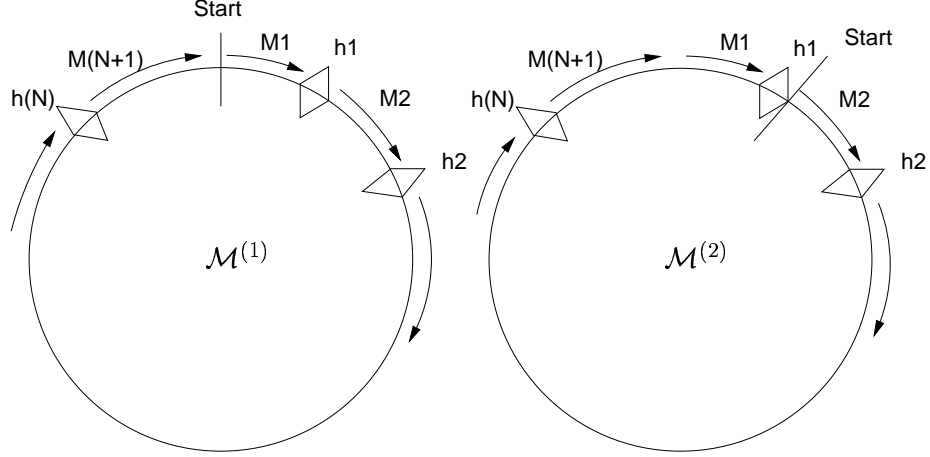\end{aligned}
$$

Figure 5.1: Schematic view of the ring for maps at two different longitudinal start-ing locations. The arrows represent the linear maps and the diamonds the non–linear multipolar kicks.

where A_1 and A_2 are transformations that bring the local coordinates into the nor-malized coordinates. Applying $A_2 M_1 A_1^{-1}$ to h_1 the following relation holds be-tween $h^{(1)}$ and $h^{(2)}$:

$$h^{(2)} = A_2 M_1^{-1} A_1^{-1} h^{(1)} - A_2 h_1 + A_2 M_2 \cdots M_{N+1} M_1 h_1 \qquad (5.6)$$

Using $R = A_2 M_2 \cdots M_{N+1} M_1 A_2^{-1}$ and grouping terms with h_1 the following relation is obtained,

$$h^{(2)} = A_2 M_1^{-1} A_1^{-1} h^{(1)} + (R - 1) A_2 h_1 \qquad (5.7)$$

which expresses the relation between the two Hamiltonians. The generating func-tion for both locations using eq. (3.29) is expressed as

$$F^{(1)} \;\; = \;\; \frac{1}{1-R} h^{(1)} \qquad (5.8)$$

$$F^{(2)} \;\; = \;\; \frac{1}{1-R} h^{(2)} \qquad (5.9)$$

By introducing $h^{(2)}$ from eq. (5.7) into eq. (5.9) and using the fact that R commutes with $A_2 M_1^{-1} A_1^{-1}$, since they are both rotations in the normalized phase space, the relation between $F^{(2)}$ and $F^{(1)}$ is expressed as

$$F^{(2)} = A_2 M_1^{-1} A_1^{-1} F^{(1)} - A_2 h_1 \qquad (5.10)$$

This equation shows how the generating function changes along the ring. If there are no non–linear kicks between the two initial longitudinal positions the term $A_2 h_1$ of eq. (5.10) will vanish and $F^{(1)}$ and $F^{(2)}$ will be smoothly related by the

change of phase given by $A_2 M_1^{-1} A_1^{-1}$. Otherwise when there is a non–linear kick in between, represented by h_1, an abrupt change in the phase and the amplitude of the corresponding generating term can be expected.

As an example a generating function term is computed around the longitudinal position of a ring. The aim of the example is to illustrate the predictions of eq. (5.10). The ring is modeled to be a standard FODO lattice with three sextupoles at the locations $s_1 = 0.33$, $s_2 = 0.49$ and $s_3 = 0.70$ (in arbitrary units). Sextupoles create, among others, the generating function term f_{3000} defined in eq. (3.32). The amplitude of this term has been obtained from a tracking simulation by performing the FFT of the turn–by–turn data as explained in section 3.4. In figure 5.2 this amplitude is plotted versus the longitudinal position where the turn–by–turn data is acquired. The steps in the amplitude of f_{3000} occur at the locations of the sextupoles. In the regions between sextupoles the amplitude of the term f_{3000} remains constant. Since the machine is circular the amplitudes of f_{3000} at the beginning and at the end of the lattice have to be the same.
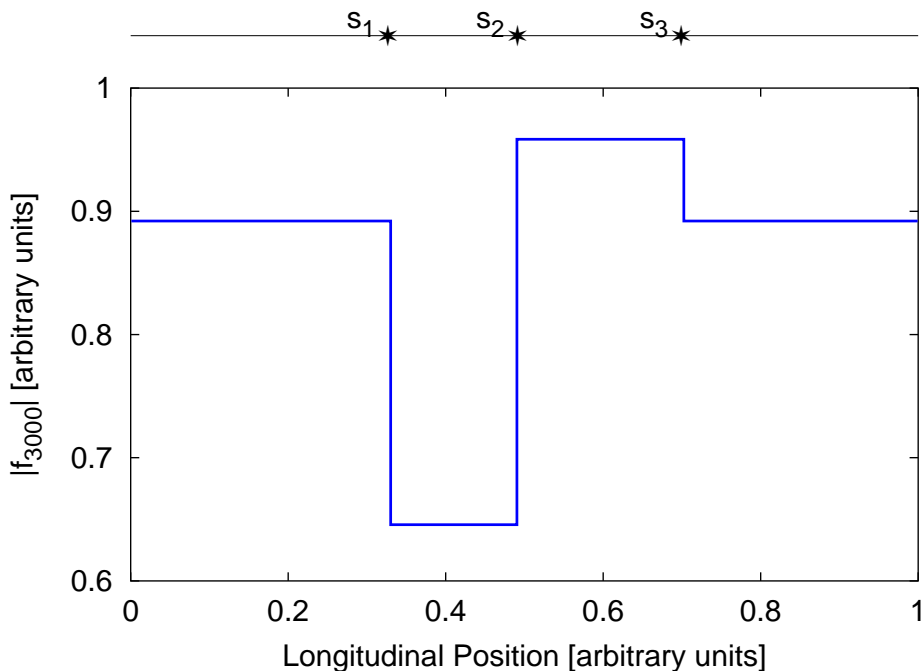

Figure 5.2: Amplitude of the generating term f_{3000} versus the longitudinal coordinate. The location of the three sextupoles is indicated on the top.

An analytical illustration is given by computing the Hamiltonian term h_{3000} at the three different regions ($h_{3000}^{(s_1)}$, $h_{3000}^{(s_2)}$ and $h_{3000}^{(s_3)}$). As given by eq. (5.5) each sextupole contributes to $h_{3000}^{(s_1)}$ with a certain quantity defined in the following expression,

$$h_{3000}^{(s_1)} = h_{1_{3000}} + h_{2_{3000}} + h_{3_{3000}} \, .$$

$h_{3000}^{(s_2)}$ is computed from $h_{3000}^{(s_1)}$ using eq. (5.7) in the following way

$$
\begin{aligned}
h_{3000}^{(s_2)} &= e^{i3\Delta\phi_x} h_{3000}^{(s_1)} + (e^{-i3Q_x} - 1)e^{i3\Delta\phi_x} h_{1_{3000}} \\
&= e^{i3\Delta\phi_x}\left(h_{1_{3000}}e^{-i3Q_x} + h_{2_{3000}} + h_{3_{3000}}\right),
\end{aligned}
\tag{5.11}
$$

where $\Delta\phi_x$ is the horizontal phase advance between s_1 and s_2. $h_{3000}^{(s_3)}$ is computed from $h_{3000}^{(s_2)}$ in a similar way. The amplitudes of the Hamiltonian terms are summarized in the following expression,

$$
\begin{aligned}
|h_{3000}^{(s_1)}| &= |h_{1_{3000}} + h_{2_{3000}} + h_{3_{3000}}|, \\
|h_{3000}^{(s_2)}| &= |h_{1_{3000}}e^{-i3Q_x} + h_{2_{3000}} + h_{3_{3000}}|, \\
|h_{3000}^{(s_3)}| &= |h_{1_{3000}}e^{-i3Q_x} + h_{2_{3000}}e^{-i3Q_x} + h_{3_{3000}}|.
\end{aligned}
\tag{5.12}
$$

Overall phases inside the bars have been omitted. The amplitude of the corresponding generating term $f_{3000}^{(s_i)}$ is obtained by simply dividing $|h_{3000}^{(s_i)}|$ by $|1 - e^{-i3Q_x}|$. By applying this technique to a real machine one can determine the longitudinal position of the strong multipole kicks as long as BPMs are available at either side. In the following section a single particle simulation is done using a realistic model of the SPS.

5.2 Simulation of the longitudinal variation of f_{3000}

The aim of this section is to show the usefulness of this technique when applied to operating accelerators. In particular it is investigated how errors in the powering polarities of non–linear elements can be found. A single particle simulation is done using a realistic model of the SPS with the extraction sextupoles. Apart from the extraction sextupoles the SPS has 108 chromaticity sextupoles used to correct the chromaticity in normal operation. Two settings of the extraction sextupoles are being considered:

- The nominal case, where the extraction sextupoles are powered: $(+30, +30, +30, +30, -30, -30, -30, -30)$ A.

- The opposite case, where the extraction sextupoles are powered: $(-30, -30, -30, -30, +30, +30, +30, +30)$ A.

The code SixTrack is used to track a single particle through the lattice. Turn–by–turn data is obtained at many longitudinal locations of the ring and the amplitude of the spectral line (–2, 0), proportional to f_{3000}, is obtained from the FFT of the data. The results from the first case are shown in figure 5.3. The location of the extraction sextupoles is indicated with vertical lines. The largest abrupt changes of the curve are located where the extraction sextupoles sit as it is expected since these are the strongest sextupoles. Small jumps occur all around the ring due to the chromaticity sextupoles. The variation of the spectral line (–2, 0) for the case
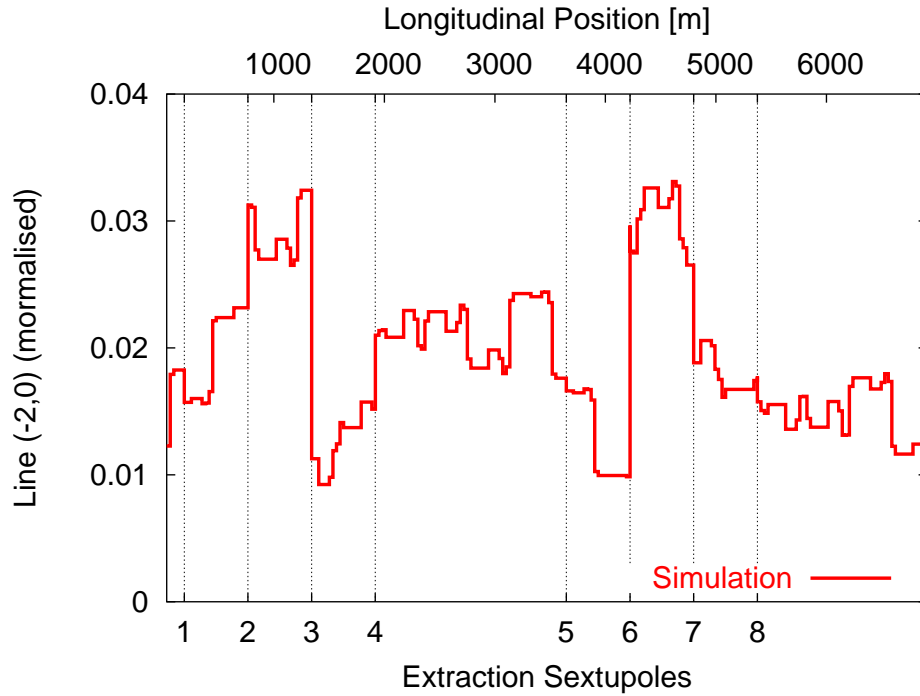
Figure 5.3: Simulated amplitude of the line $(-2, 0)$ versus the longitudinal co-ordinate for the nominal SPS model with extraction sextupoles with polarities: $(+ + + + - - - - 30)$ A. The vertical lines indicate the location of the extraction sextupoles.

with opposite polarities is shown in figure 5.4. The jumps of the curve occur at the same locations than before but clearly the curves of the two cases are different. This difference is enough to determine the polarities of the extraction sextupoles at the SPS by measuring the generating term f_{3000}.
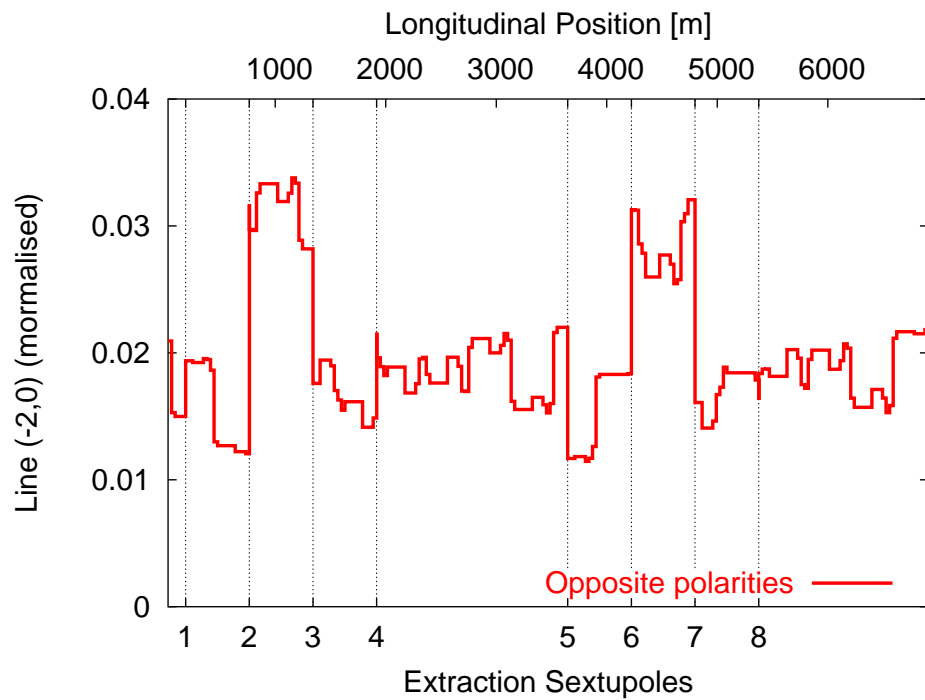
Figure 5.4: Simulated amplitude of the line (–2, 0) versus the longitudinal coordinate considering opposite polarities for the nominal SPS model with extraction sextupoles with polarities: $(- - - - + + + + 30)$ A. The vertical lines indicate the location of the extraction sextupoles.

Chapter 6

Description of the SPS

6.1   The SPS in CERN

The SPS is part of the complex of accelerators at CERN. The largest accelerator at CERN will be the LHC. The LHC beam will be supplied by a chain of proton accelerators, shown in figure 6.1. The SPS receives the proton beam from the CERN Proton Synchrotron (PS) at an energy of 26 GeV and will accelerate the beam up to 450 GeV to inject it into the LHC.

The SPS is a proton synchrotron with an average radius of 1100 m. Its lattice consists of 108 FODO cells. A FODO cell consists of a focusing quadrupole and a defocusing quadrupole separated by dipoles. The phase advance per cell is almost $\pi/2$. Therefore the nominal tunes are around 27, e.g. 26.62 in the horizontal plane and 26.58 in the vertical. A more detailed description of the SPS could be found in [26].

6.2   SPS instrumentation

The SPS is equipped with a large collection of instruments used to control the beam and measure its parameters. In the following sections a brief description of the instruments used in the experiments is given. The location of some of these instruments is shown in the schematic SPS layout of figure 6.2 [27].

6.2.1   BPM and MOPOS system

BPMs are used to measure the transverse excursion of the centroid of the beam. The majority of the BPMs of the SPS are of electrostatic type. These monitors basically consist of two conductor plates at both sides of the beam pipe. An illustration of an SPS pick–up is shown in figure 6.3. When the beam goes through the BPM its position is inferred from the potential difference between the plates. The SPS is equipped with about 110 BPMs in either transverse plane and they are uniformly distributed around the ring. The phase advance between consecutive

CMS

LHC

COMPASS

North Area

SPS

ALICE

ATLAS

West Area

LHC-b

neutrinos

ISOLDE

CNGS

East Area

AD

pbar

PSB

PS

TT10

LINAC2

LINAC3

LEIR

p   Pb ions

Gran Sasso (I)
730 km

protons
antiprotons
ions
neutrinos to Gran Sasso (I)

LHC: Large Hadron Collider
SPS: Super Proton Synchrotron
AD: Antiproton Decelerator
ISOLDE: Isotope Separator OnLine DEvice
PSB: Proton Synchrotron Booster
PS: Protron Synchrotron
LINAC: LINear ACcelerator
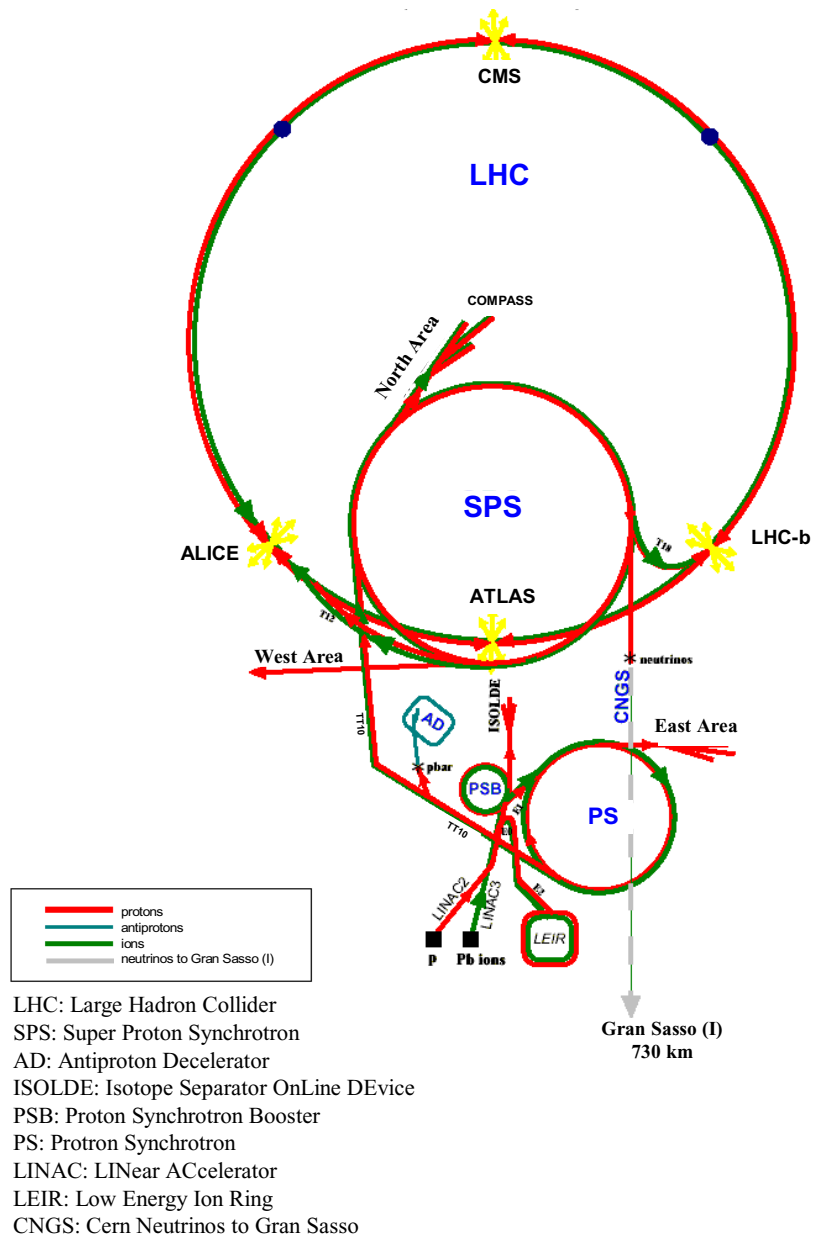LEIR: Low Energy Ion Ring
CNGS: Cern Neutrinos to Gran Sasso

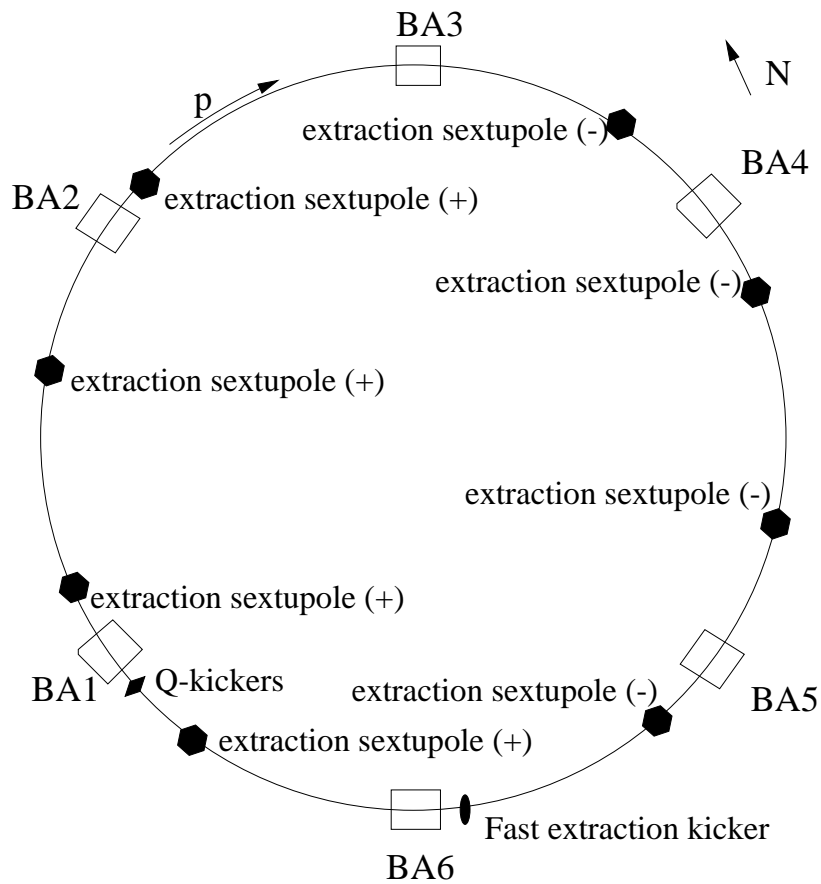Figure 6.1: Accelerator complex in CERN.

Figure 6.2: Simplified SPS layout. The eight extraction sextupoles and the kicker magnet are shown at their locations in the SPS. The signs in brackets denote the usual polarity of the sextupole during the experiments. BA stands for access hall.

Figure 6.3: An SPS pick–up installed in the beam pipe.

pick–ups is almost $\pi/2$ and the typical beta functions at the pick–ups are shown in table 6.1. The signal coming out of the BPMs is electronically processed and collected by the Multi Orbit Position System (MOPOS) system. Detailed descriptions of this system can be found in [28] and [29]. 1000 turn data from all the available pick–ups is acquired by using the code MTmeasure [30]. The code MTmeasure can save the multi–turn BPM data in different formats and can perform some orbit analysis. In order to obtain a reliable BPM signal during the experiments the timing parameter and the gain of the electronics had to be carefully adjusted [31].

6.2.2   Q–kickers

Kickers are magnets that produce a constant transverse magnetic field when the beam is going through. They are normally used to excite horizontal or vertical betatron motion by producing the appropriate magnetic field during a single turn. The SPS is equipped with a horizontal and a vertical Q–kickers. They are called Q–kickers since in normal operation they are used to measure the transverse tunes. The relevant magnetic parameters of these kickers are shown in table 6.2 [32] and the lattice functions are shown in table 6.1. In our experiments these kickers are used to excite the transverse motion for energies of 80 GeV or below.

6.2.3   Extraction kicker

This horizontal kicker is more powerful than the Q–kickers. In normal operation it is used for the fast beam extraction. In our experiments at 120 GeV this kicker was used to excite the horizontal betatron motion. At its maximum voltage of 15 KV its kick strength is 0.129 Tm. The lattice functions at the location of this kicker are shown in table 6.1. Recently this kicker has been removed from the SPS to reduce the total impedance [33] of the machine.

6.2.4   Extraction sextupoles

In normal operation these sextupoles are used for the slow or resonant extraction of the beam. The SPS is equipped with eight extraction sextupoles. A technical description of these elements can be found in [34]. In our experiments they were used to create a controllable amount of non–linearity. The lattice functions at the location of these elements are shown in table 6.1.

6.2.5   Skew quadrupoles

A skew quadrupole is a normal quadrupole rotated by 45 degrees. The SPS is equipped with six skew quadrupoles powered in series. In normal operation they are used to compensate the coupling errors of the machine. The lattice functions at the location of these elements are shown in table 6.1.

BPMs			
type	$\beta_x[m]$	$\beta_y[m]$	
BPMH	103.4	20.4	
BPMV	20.4	103.4	
Kickers			
name	$\beta_x[m]$	$\phi_x[2\pi]$	$\beta_y[m]$	$\phi_y[2\pi]$
MKQH	64.5	1.96	37.0	2.02
MKQV	33.8	2.00	70.0	2.05
MKE	87.4	24.89	25.0	24.83
Extraction sextupoles				
name	$\beta_x[m]$	$\phi_x[2\pi]$	$\beta_y[m]$	$\phi_y[2\pi]$
LSE.1060	97.761	0.737	21.775	0.729
LSE.1240	97.718	2.955	21.827	2.942
LSE.2060	97.748	5.173	21.797	5.158
LSE.2240	97.754	7.390	21.812	7.371
LSE.4060	97.663	14.047	21.782	14.018
LSEN.424	97.764	16.265	21.864	16.233
LSE.5060	97.676	18.484	21.760	18.449
LSE.5240	97.780	20.703	21.866	20.664
Skew quadrupoles				
name	$\beta_x[m]$	$\phi_x[2\pi]$	$\beta_y[m]$	$\phi_y[2\pi]$
LQSA.129	21.902	3.552	97.271	3.575
LQSA.229	21.89	7.98	97.197	8.005
LQSA.329	21.90	12.42	97.110	12.435
LQSA.429	21.91	16.86	97.099	16.866
LQSA.529	21.92	21.30	97.172	21.297
LQSA.629	21.91	25.73	97.260	25.726

Table 6.1: Relevant lattice functions of the different SPS elements.

Magnet	MKQH	MKQV
Deflection direction	horizontal	vertical
Magnetic flux density (25 KV) [T]	0.074	0.0246
Kick strength (25 KV) [Tm]	0.0357	0.0250
Maximum voltage [KV]	25	25
Magnet filling time [μs]	0.38	0.112

Table 6.2: Relevant parameters of the SPS Q–kickers.

Chapter 7

SPS experiments

A series of experiments to measure resonance driving terms in the SPS has been performed during the years 2000, 2001 and 2002 . Prior to this study pioneering experiments were carried out [35, 36]. Since the SPS is a very linear machine the extraction sextupoles were used to create a controllable amount of non–linearities. Furthermore the skew quadrupoles were also used to create and to correct coupling. In the following sections these experiments are discussed in chronological order.

7.1   Experiments at 26 and 120 GeV in 2000

Energy [GeV]	26	120
Intensity [number of protons]	2×10^{10}	2×10^{12}
Number of bunches	1	84
Nominal Tunes $[Q_x, Q_y]$	26.62, 26.58	26.62, 26.58
Chromaticities $[Q'_x, Q'_y]$	0.3, 0.3	0.52, 0.16

Table 7.1: Measured beam conditions for the experiments during 2000.

7.1.1   Measurement of linear coupling at 26 GeV

The experiments at 26 GeV were mostly focused on the measurement of linear coupling. The beam conditions are shown in table 7.1. There are two resonances contributing to the linear coupling: (1,–1) and (1,1). Resonance (m,n) means that $mQ_x + nQ_y = p$, being m, n and p integer numbers. The tunes of our experiments are much closer to the resonance (1,–1) than to the (1,1). For this reason the target of our experiments is the resonance (1,–1). The first order resonance term driving this resonance is h_{1001} as can be seen from eq. (3.32). The contribution of this term to the linearly normalized horizontal variable is given by eq.(3.38)

$$h_x^-(N) \quad = \quad \sqrt{2I_x} e^{i(2\pi\nu_x N + \psi_{x_0})} - 2i f_{1001} \sqrt{2I_y} e^{i(2\pi\nu_y N + \psi_{y_0})} . \quad (7.1)$$

By virtue of this equation the term f_{1001} can be inferred by measuring the spectral line with frequency ν_y in the horizontal signal. The procedure adopted in the experiment is now described. For a given skew quadrupole strength and a constant ratio of horizontal to vertical kick strength the amplitude of the spectral line (0,1) has been recorded from the Q–kicker monitor display. The BPM data could not be used due to a poor adjustment of the electronics. For each value of the skew quadrupole strength we have averaged over a number of injections shots (40–50). The results of the measurement on the 18th June 2000 are depicted in figure 7.1. It is not clear why such an averaging procedure is needed but in this way we could determine the optimal skew quadrupole setting to a good precision. In fact, we could demonstrate that with this technique we had achieved a closest tune approach of $(2 \pm 1)10^{-4}$ which is a factor of five better than previously. Another problem is the fact that the slopes of the lines in figure 7.1 differ by a factor of two (see later section 7.2.2 for an explanation).

7.1.2   Measurement of resonant terms and amplitude detuning at 120 GeV

The experiments at 120 GeV were focused on the measurement of resonance terms and amplitude detuning. The beam conditions are shown in table 7.1. At this energy the extraction kicker was used to excite the betatron motion. The previously discussed method to compensate the coupling was used, obtaining a closest tune approach of 2×10^{-3}. The extraction sextupoles were powered to 140 A with polarities $(+ + + + + - - - -)$. Various sets of BPM data, from all the available BPMs, for different oscillation amplitudes were recorded for off–line analysis. For this analysis the complex signal constructed from two adjacent pick–ups is Fourier analyzed by using the SUSSIX [24] code. The first result from this analysis is the variation of the tunes with the horizontal oscillation amplitude. In figure 7.2 the horizontal and vertical detunings are plotted versus the square of the betatronic amplitude ($\epsilon_x = A_x^2/\beta_x$). In this figure the experimental results are compared to two models, one containing the known sextupolar sources and the other one containing an optimized octupolar component. The octupolar component was set to match the measured amplitude detuning since the origin and location of this component is unknown. For the horizontal tune both models give similar results and they are in good agreement with the measurements. For the vertical tune only the optimized model shows a good agreement.

From the Fourier analysis the amplitude of the spectral lines due to the sextupolar resonances are also computed. The resonances (3,0) and (1,0) are driven by the terms h_{3000} and h_{1200} respectively. They produce the spectral lines (–2, 0) and (2, 0) in the horizontal motion. The amplitude of these spectral lines normalized to the amplitude of the tune line are linear in the oscillation amplitude as derived from eq. (3.38). This normalization is needed to get rid of the uncertainties of the calibration of the pick–ups. In figures 7.3 and 7.4 the normalized amplitude of the spectral lines (–2, 0) and (2, 0) averaged over all pick–ups are plotted versus
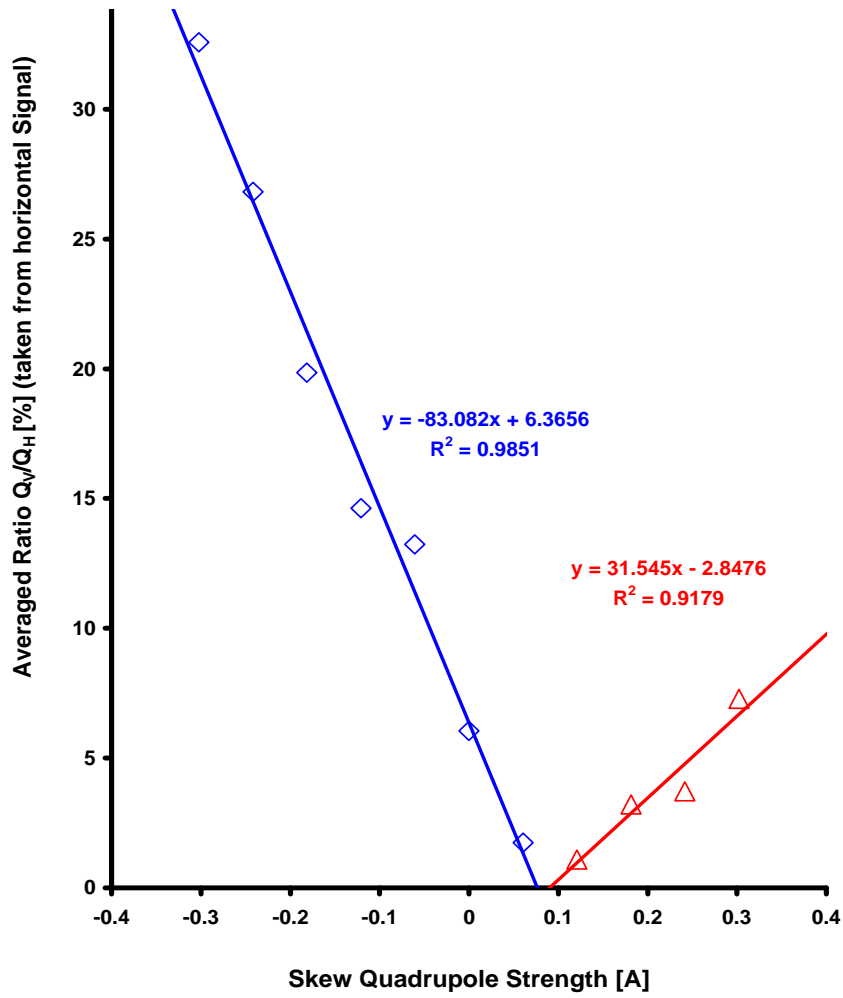
Figure 7.1: Normalized amplitude of the spectral line (0,1) from the horizontal signal versus the strength of the skew quadrupoles.
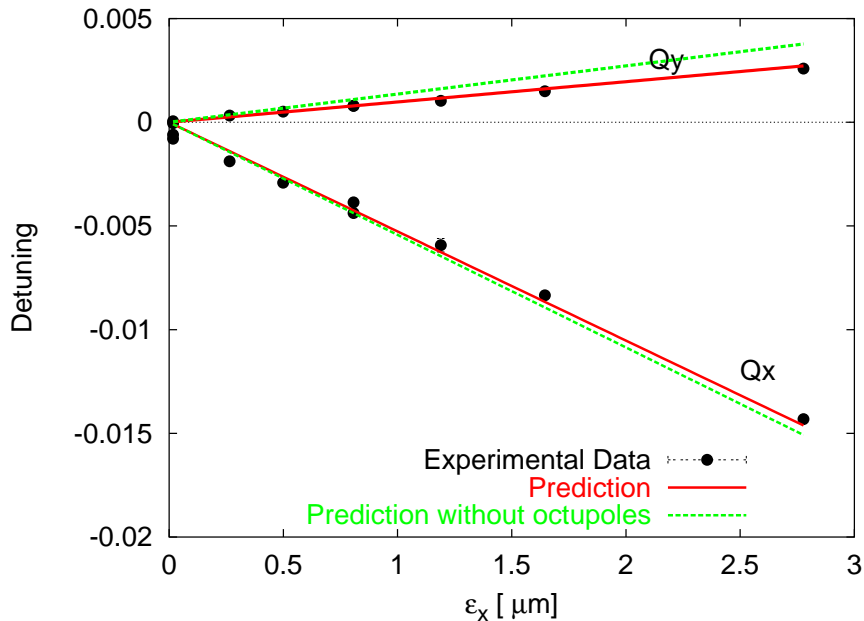
Figure 7.2: Horizontal and vertical detuning as a function of $\epsilon_x = A_x^2/\beta_x$.

$\epsilon_x^{1/2}$ from model and experiment. The experimental values are multiplied by the decoherence factor of 2 to compare to the single particle model. The error bars represent the computed rms from the longitudinal variation. The agreement in the average value and in the rms is excellent.   As derived in chapter 5 the resonance driving terms vary around the ring. In figure 7.5 the normalized amplitude of the spectral line (–2, 0) computed for all the BPMs for a middle kick amplitude is plotted versus the longitudinal location. In the figure the prediction from the nominal model is also shown and the location of the extraction sextupoles is represented by the vertical lines. The agreement between model and experiment on the average is good and the abrupt changes occur at the same places but the shape of the curves are clearly different. This discrepancy could be explained if the extraction sextupoles had opposite polarities than those of the chromaticity sextupoles. In figure 7.6 the same plot is presented but using the opposite polarities for all the extraction sextupoles. Since the agreement had largely improved hardware checks were done confirming that the polarities of these sextupoles were reversed. This was the first success of this technique in finding lattice errors.

7.1.3   Measurement of spectral distributions

In chapter 4 analytical expressions were given describing the shape of the different spectral lines in presence of decoherence processes. In principle, by fitting these expressions to the measurements beam parameters like the beam size could be
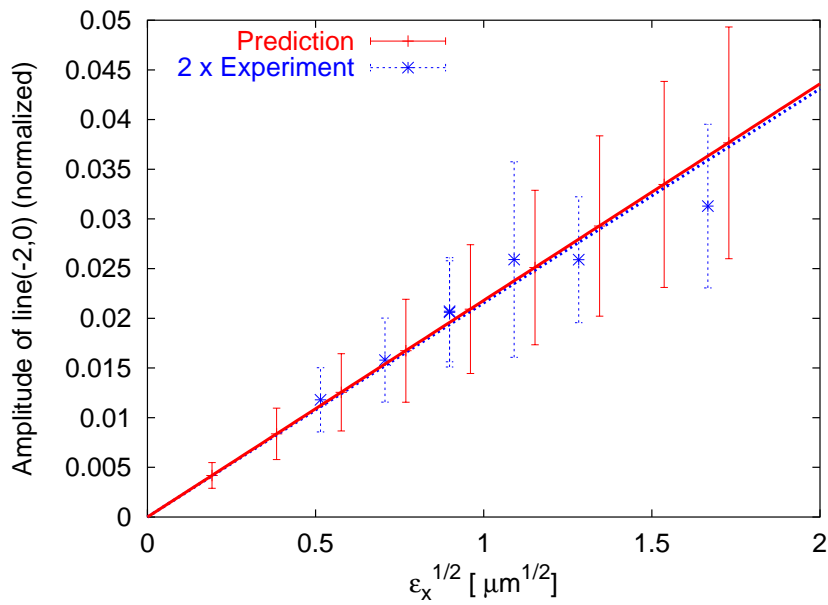
Figure 7.3: Normalized Amplitude of the spectral line (–2,0) averaged over all pick–ups versus $\epsilon_x^{1/2}$ from model and experiment. The bars represent the computed rms from the longitudinal variation.
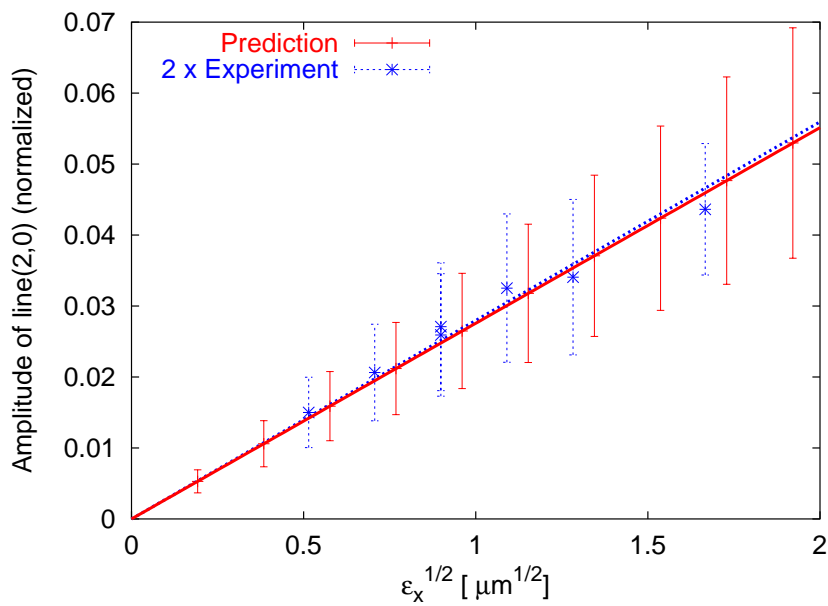

Figure 7.4: Normalized Amplitude of the spectral line (2,0) averaged over all pick–ups versus $\epsilon_x^{1/2}$ from model and experiment. The bars represent the computed rms from the longitudinal variation.
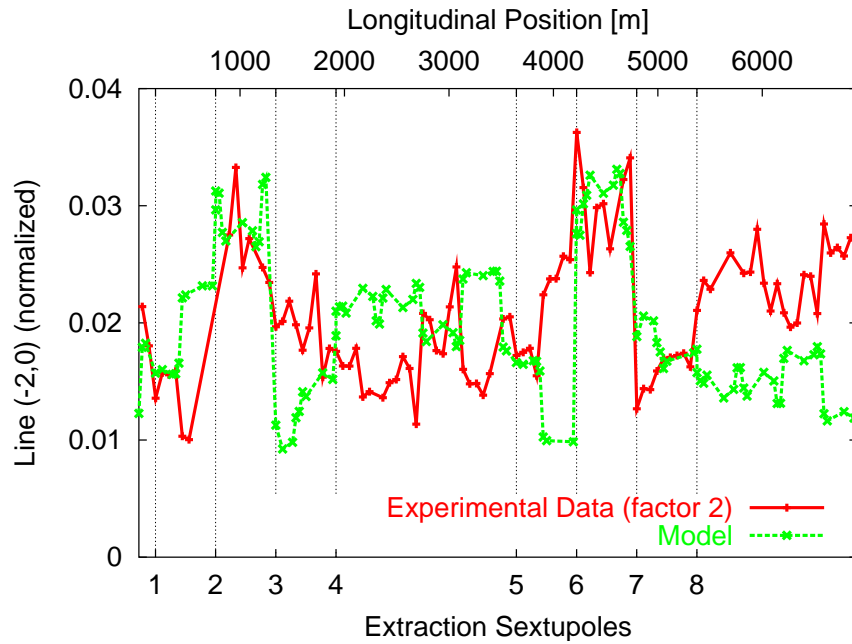
Figure 7.5: Longitudinal variation of the spectral line (–2,0) from experiment and from the nominal model.
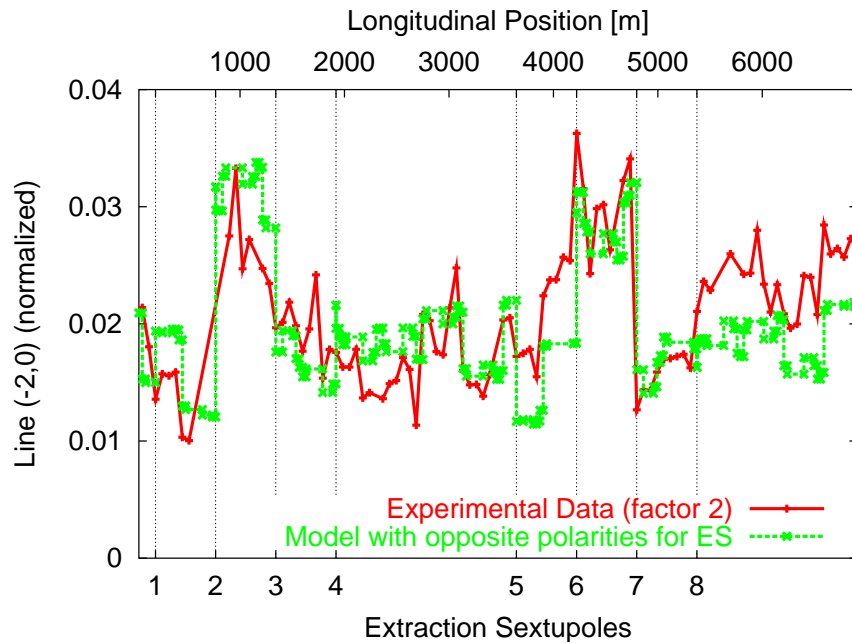

Figure 7.6: Longitudinal variation of the spectral line (–2,0) from experiment and model with opposite sextupole polarities.

obtained. Although amplitude detuning has the negative effect of introducing the decoherence factors there would be a positive side if these beam parameters could be measured. For this reason measurements of the spectral distributions have been performed.

The analytical expression describing the shape of the tune line in presence of amplitude detuning is given by eq.(4.14)

$$\mathcal{A}^-_{x,tune}(w) \quad = \quad \frac{1}{|\nu'_{xx}|}\sqrt{2I_x(w)}e^{-\frac{1}{2}(2I_x(w)+\overline{A}^2_x)}\,\mathrm{I}_1\left(\overline{A}_x\sqrt{2I_x(w)}\right)\,, \quad (7.2)$$

$$2I_x(w) \quad = \quad \frac{1}{\nu'_{xx}}(w/2\pi - Q_x)\,. \tag{7.3}$$

A fit of this analytical expression is done to the measured tune line from the experimental data. The free parameters in the fit are the tune at zero amplitude Q_x, the amplitude detuning coefficient ν'_{xx} and the kick in beam sigmas $\overline{A}_x$. The experimental and the fitted curve are shown in figure 7.7. The numerical results of the fit compared to the measurements of other available methods are presented in table 7.2. Unfortunately, due to time limitations, the beam size could not be measured with other method during the experiment. This explains the two missing entries of the table. The agreement between the results from the fit and those from other methods is satisfactory. It is also important to note that the errors of the fitted quantities are relatively low indicating the suitability of the model.
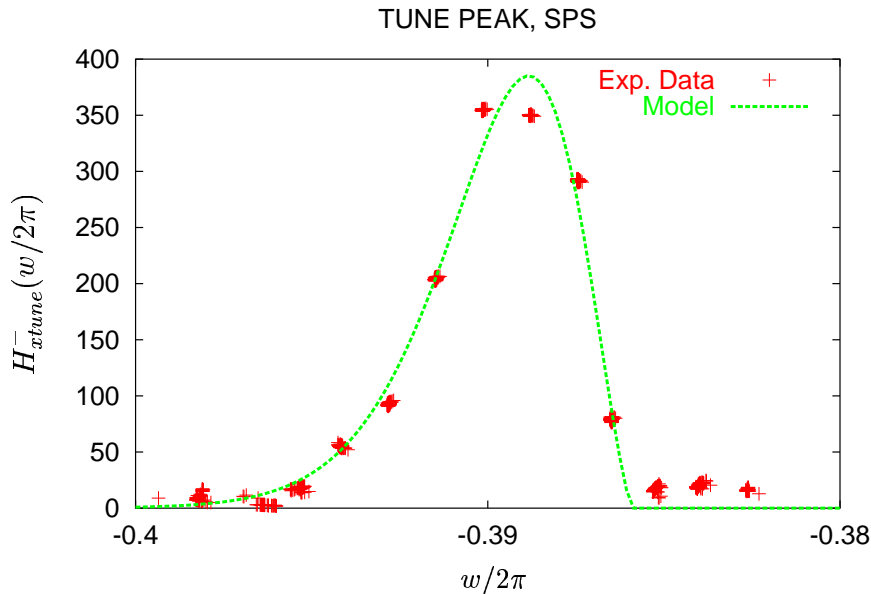

Figure 7.7: Spectral tune line obtained from experimental data together with a fit of the predicted curve.

Magnitude	Fit res.	Other Meth.
Q_x	$-0.38593 \pm 5 \cdot 10^{-5}$	-0.3859
$\nu'_{xx}[\sigma^{-2}]$	$(-3.6 \pm 0.1) \cdot 10^{-4}$	$-3.71 \cdot 10^{-4}$ [†]
$\overline{A}_x[\sigma]$	2.66 ± 0.08	
$\sigma_x[mm/\sqrt{\beta_x}]$	0.266 ± 0.008*	

Table 7.2: Results from the fit compared to other measurements.
[†] σ taken from this fit.
* Kicker Calibration used.

7.2   Experiment at 26 GeV in 2001

The beam conditions during the experiments in 2001 are listed in table 7.3. The experiments are divided in three parts: machine set–up, measurement of the coupling resonance and measurement of sextupolar resonances. During the machine set–up the RF parameters were optimized, the tunes were set to the nominal tunes, the closed orbit and the chromaticities were corrected and the amplitude detuning was compensated using the Landau octupoles. This part was carefully carried out since we learned from the previous year that a proper set–up of the machine is fundamental for the success of this experiment.

Once the machine set–up is finished the linear coupling is measured and corrected. During this part of the experiment horizontal and vertical single kicks were applied to the bunch few seconds after the injection. The amplitude of the kicks is constant during the coupling measurement. For various skew quadrupole strengths the amplitudes of the coupling spectral lines, i.e. the vertical tune line in the horizontal plane and the horizontal tune line in the vertical plane, are evaluated via Fourier analysis. The optimal skew quadrupole setting was determined to minimize the linear coupling of the machine. Results from this part are discussed in section 7.2.2. Prior to this discussion the BPM pre–analysis needed to detect noisy pick–ups is presented in section 7.2.1.

Energy [GeV]	26
Intensity [number of protons]	2×10^{10}
Number of bunches	1
Nominal Tunes $[Q_x, Q_y]$	26.62, 26.58
Chromaticities $[Q'_x, Q'_y]$	1.3, 0.4

Table 7.3: Measured beam conditions for the experiments in 2001.

The last part of the experiment was devoted to the measurement of sextupolar resonance driving terms for different sextupole configurations and tunes. The

extraction sextupoles were used to create a controllable amount of non–linearity. The procedure for each different configuration was to apply a single kick in the horizontal plane and record the BPM data for off–line analysis. This is done for various kick amplitudes ranging from 1 mm to the maximum kick determined by the loss of the beam. The analysis of these data is discussed in section 7.2.3.

7.2.1 BPM Pre–analysis

In order to find and to reject faulty or noisy pick–up signals a BPM pre–analysis was carried out. The Fourier spectrum of the turn–by–turn signal of an ideal pick–up should have well localized peaks but noisy or faulty pick–ups will have a randomly populated Fourier spectrum. In particular the rms of the amplitude of the background of the Fourier spectrum is larger for the more noisy BPMs. This feature is used to identify the noisy pick–ups. The rms of the background of the Fourier spectrum is estimated by computing the rms of the amplitudes of the spectral lines within a spectral window. This window is chosen in such a way that an ideal pick–up would not contain any peak in that window. It is also important to avoid that the spectral window contains the zero frequency. For our experiments, with the fractional tunes being 0.62 and 0.58, the window was chosen to be delimited between 0.02 and 0.16. The observable used for indicating the noise level of the pick–up is the rms of the amplitudes of the lines contained in the chosen spectral window. This technique is illustrated in figure 7.8. This rms based observable is computed for all the signals from all the pick–ups and by examination a threshold value is chosen to decide what is a bad pick–up. In figure 7.9 the number of signals having a certain rms observable is plotted versus this rms for a sample of 51000 signals. From this figure it was decided to reject all the BPMs with an rms larger than 8 μm. As a result a third of all the BPM signals, 17000, mainly coming from the pick–ups of the last two sextants of the SPS were rejected. The reader will notice this lack of information in the figures of next sections.

7.2.2 Measurement of linear coupling

The technique of coupling correction consists of measuring the amplitudes of the coupling lines, normalized to the amplitude of the fundamental line, as a function of the strength of the skew quadrupoles. In figure 7.10 the coupling lines from the horizontal and vertical signals are plotted versus the skew quadrupole strength. The systematic error corresponds to the rms value of the measured magnitude from all the available pick–ups. The random error corresponds to the rms value of the measured magnitude from the different injections. The total error is calculated by adding quadratically the systematic plus the random errors. The optimum setting of the skew quadrupoles is then inferred by finding the minimum coupling line amplitude. Note that the two minima of the coupling lines of figure 7.10 correspond to the same skew quadrupole strength. Similar to the results of the previous year the slopes at either side of the minimum are different. A revision of the theory
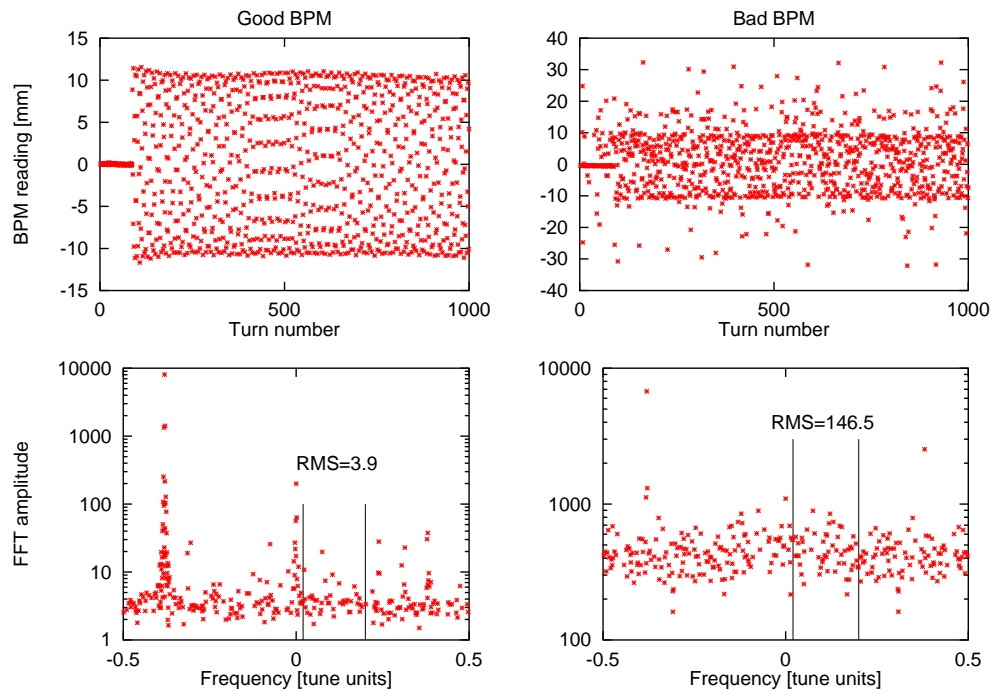
Figure 7.8: Examples of good (left) and bad (right) pick–up signals and spectra. An appropriate window to compute the noise level with the particular values is shown.
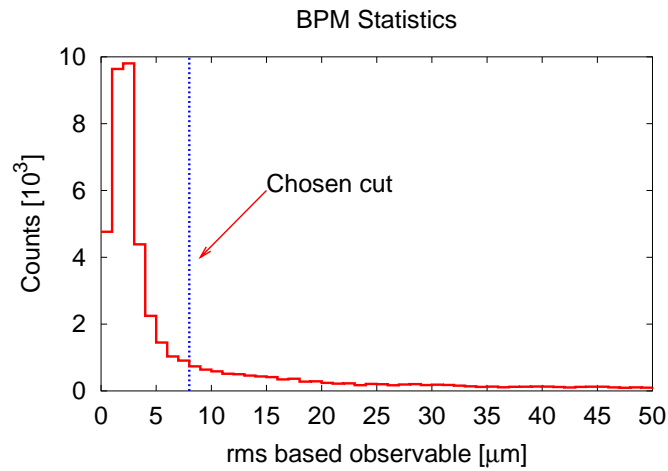

Figure 7.9: Number of BPM signals having a certain rms of the amplitudes of the spectral lines within the spectral window delimited between 0.02 and 0.16. The sample contains a total of 51000 signals.
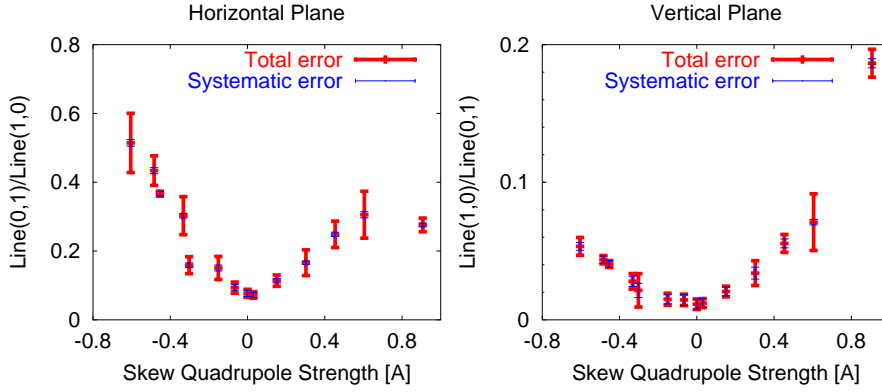
Figure 7.10: Coupling lines versus the strength of skew quadrupoles. On the left, the amplitude of the vertical tune line normalized to the horizontal tune line from the horizontal signal. On the right, the amplitude of the horizontal tune line normalized to the vertical tune line from the vertical signal.

will be given next how to explain this puzzle and how to define a more appropriate observable. The turn–by–turn horizontal and vertical coordinates in first order in the coupling resonance term f_{1001} are given by

$$
\begin{aligned}
\hat{x}(N) - i\hat{p}_x(N) &= \sqrt{2I_x}e^{i(2\pi\nu_x N + \psi_{x0})} \\
&\quad - 2if_{1001}\sqrt{2I_y}e^{i(2\pi\nu_y N + \psi_{y0})} \ , \\
\hat{y}(N) - i\hat{p}_y(N) &= \sqrt{2I_y}e^{i(2\pi\nu_y N + \psi_{y0})} \\
&\quad - 2if_{1001}^*\sqrt{2I_x}e^{i(2\pi\nu_x N + \psi_{x0})} \ ,
\end{aligned}
\tag{7.4}
$$

where f_{1001}^* is the complex conjugate of f_{1001}. The measurable amplitudes of the fundamental horizontal and vertical tunes are represented by line$(1,0)_H$ and line$(0,1)_V$ respectively. The measurable amplitude of the spectral line with the vertical tune in the horizontal plane is represented by line$(0,1)_H$ and corresponds, in the previous equations, to the quantity $|2f_{1001}\sqrt{2I_y}|$. Accordingly, the measurable amplitude of the spectral line with the horizontal tune in the vertical plane is represented by line$(1,0)_V$ and corresponds to $|2f_{1001}\sqrt{2I_x}|$. From these equations it can be seen that the normalized amplitude of the vertical tune line from the horizontal plane is $2\sqrt{I_y/I_x}|f_{1001}|$ and the normalized amplitude of the horizontal tune line from the vertical plane is $2\sqrt{I_x/I_y}|f_{1001}|$. Therefore the best way to measure $|f_{1001}|$ independently of the actions is multiplying the former two observables. Thus,

$$
2|f_{1010}| = \sqrt{\frac{\text{line}(0,1)_H}{\text{line}(1,0)_H}\frac{\text{line}(1,0)_V}{\text{line}(0,1)_V}} \ .
\tag{7.5}
$$

In fig. 7.11 this new observable is plotted versus the strength of the skew quadrupoles together with the prediction from the model and a fit to the formula $m|x - x_0|$. The fitted parameters are indicated in the figure as well. The model contains only the skew quadrupoles but we can compare it to the measurements since the optimum setting is very close to 0 A. The agreement between measurement and prediction is excellent and the slopes are the same on both sides of the minimum.
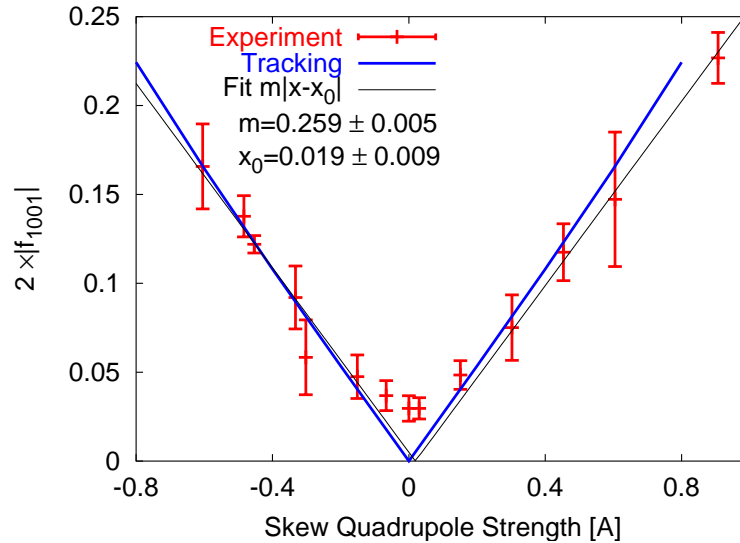

Figure 7.11: Coupling resonance term versus skew quadrupole strength. Results from experiment and tracking simulation.

This means that the difference found in the previous year between the slopes was entirely due to the variation of the oscillation amplitudes with the strength of the skew quadrupoles. This variation is due to the fact that by varying the coupling the eigen–planes at the kickers rotate. Consequently the oscillation amplitudes vary with the coupling even though the kick strengths are constant. It is important to note that for the particular case of fig. 7.11 the minimum coupling corresponds to a skew quadrupole strength of 0.019 A but this value varies from experiment to experiment.

7.2.3   Measurement of sextupolar resonance terms

To measure sextupolar resonance driving terms the beam is kicked to different amplitudes and the turn–by–turn complex signal is Fourier analyzed to obtain the amplitudes of the different spectral lines. For every pick–up the normalized amplitudes of the sextupolar spectral lines are plotted versus kick strength and a line is fitted constrained to go through the origin. As an illustration a plot from this procedure is shown in figure 7.12 for a particular pick–up and for the spectral line (–2, 0). Three measurements for every kick strength were done to assess random
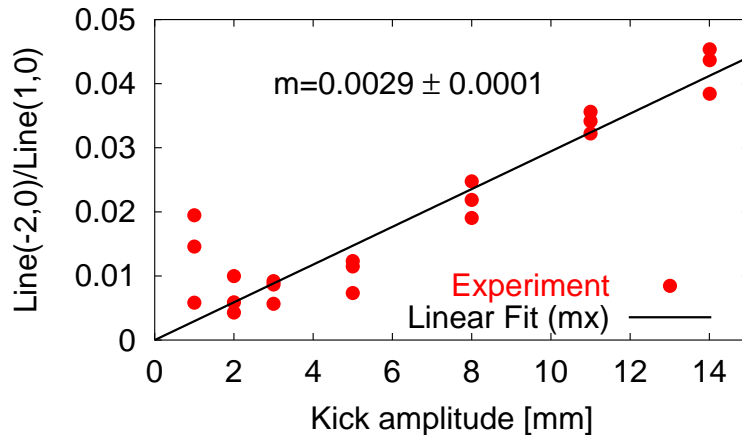
Figure 7.12: Normalized amplitude of the spectral line (–2,0) versus horizontal kick amplitude for one pick–up.

errors. The slope of the fitted line is related to the corresponding resonance term in the following way (3.38),

$$|f_{3000}| = \frac{1}{6}\left(\frac{m_{(-2,0)}}{0.094}\right)\,[\mu m^{-1/2}]\,,$$
$$|f_{1200}| = \frac{1}{2}\left(\frac{m_{(2,0)}}{0.094}\right)\,[\mu m^{-1/2}]\,. \tag{7.6}$$

where the m is the measured slope and its subscript denotes the spectral line from which this slope originates. The factor 0.094 comes from the calibration of the horizontal kicker. These relations hold as far as the beam does not experience any decoherence. When the centroid oscillations are completely damped due to decoherence caused by amplitude detuning, the spectral lines $(\pm 2, 0)$ are reduced by a decoherence factor of two. The sextupolar resonance terms are measured for different machine set–ups. The first set–up was the baseline machine with the nominal tunes $Q_x = 26.62$ and $Q_y = 26.58$. The amplitude detuning was compensated with the Landau octupoles to avoid additional decoherence of the signal. In figure 7.13 the measured amplitude of the sextupolar resonance terms f_{3000} is plotted versus the longitudinal position together with the prediction from the simulation. The error bars correspond to the errors given by the linear fit. On average, experiment and model agree and the location of the jumps (which correspond to sextupole locations) are the same in both curves. Nevertheless in some regions the curves differ in amplitude.

In another set–up of the machine the first four extraction sextupoles were powered to $+30$ A and the following four extraction sextupoles were powered to -30 A, i.e. $(+ + + + - - - -30$ A$)$. The horizontal tune was moved to 26.69. The beam oscillations were damped due to decoherence, therefore the decoherence factor is applied to compare experiment and model. In figure 7.14 (top) the measured amplitude of the sextupolar resonance term f_{3000} is plotted versus the longitudinal
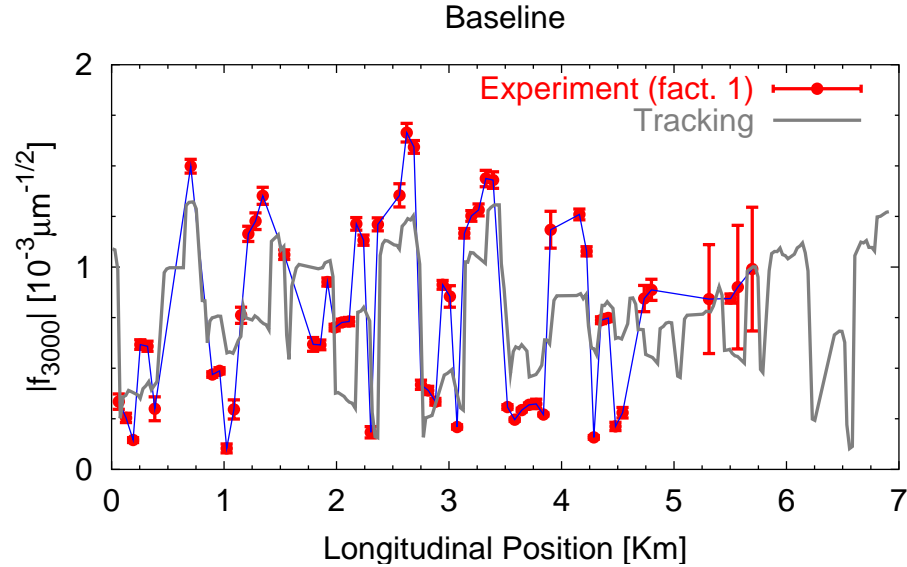
Figure 7.13: Amplitude of the term f_{3000} versus longitudinal position along the SPS ring from experiment and tracking simulation for the baseline machine. The beam data are not decohered.

position together with a tracking model. The disagreements in this plot requires an improvement of our model. If the closed orbit does not go through the center of a sextupole there is multipole feed–down and the particle observes a quadrupolar field proportional to the offset. This quadrupolar filed originates a beta–beating, i.e. changes the nominal optic functions of the machine. Finally this beta–beating changes the strength of the resonances. For this reason the displacements of the sextupoles with respect to the closed orbit were measured at the pick–ups and added to the model. A first test of this improvement of the model can be done by comparing the phase advance between adjacent pick–ups from model and experiment. This phase advance gives also an estimate of the beta–beating as presented in [37]. The phase advance between two pick–ups is measured by computing the difference in the phase of the tune lines of the respective Fourier spectra. The displacement of the closed orbit at the extraction sextupoles is provided by the readings of BPMs. In figure 7.15 the phase advance is compared for model and experiment for the baseline and for the model with extraction sextupoles displaced. The agreement is satisfactory enough to validate the improvement of the model. This new model is used to compute the resonance term. The agreement between the experiment and the new model improved considerably as shown in figure 7.14 (bottom). A similar agreement is observed for other sextupolar resonances. For example the amplitude of the term f_{1200} is shown in fig. 7.16.

Measurements were also done for a different setting of the extraction sextupoles. The horizontal tune is moved to 26.662 to be close to the third order resonance. The extraction sextupoles are powered to $(+ + + + + + + +)3$ A. In fig. 7.17 the measured amplitude of the sextupolar resonance term f_{3000} is plotted
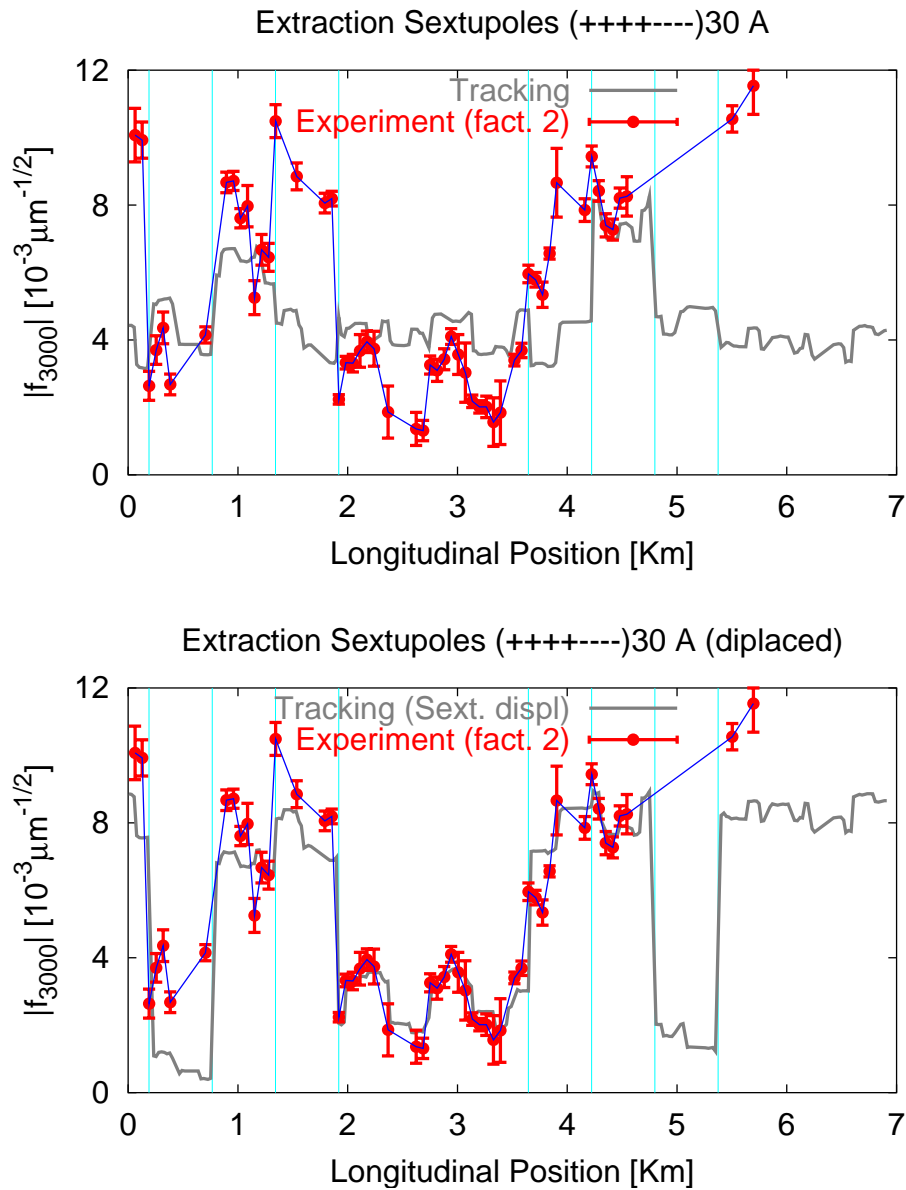
Figure 7.14: Amplitude of the term f_{3000} versus longitudinal position with extraction sextupoles on. Top: Experiment and nominal model with decoherence factor. Bottom: Experiment and model with displaced sextupoles and decoherence factor. The vertical lines show the position of the extraction sextupoles.

Figure 7.15: Comparison between the phase advance in adjacent pick-ups from model and experiment for two SPS settings: The baseline machine (top) and with the extraction sextupoles connected and displaced (bottom). The vertical lines show the position of the extraction sextupoles.
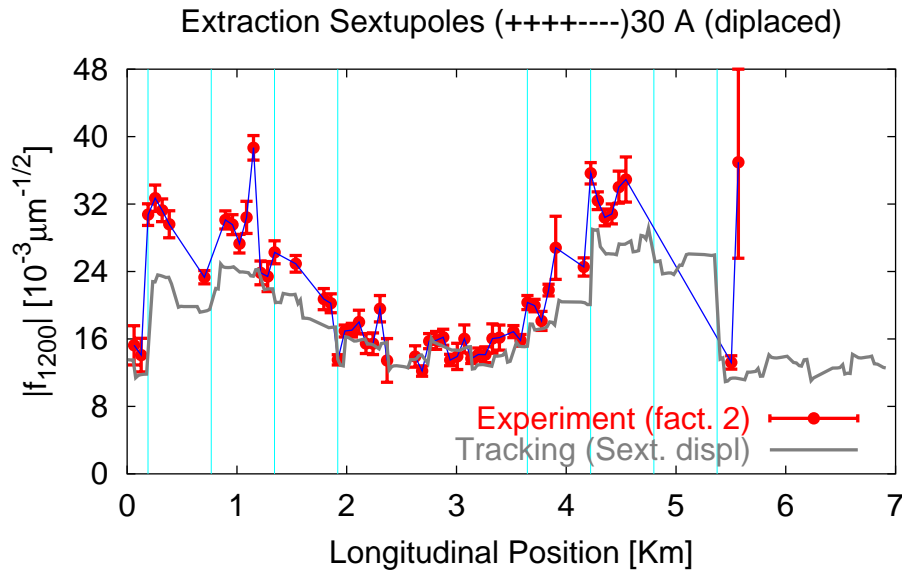
Figure 7.16: Amplitude of the term f_{1200} versus longitudinal position from experiment and tracking with displaced sextupoles and decoherence factors. The vertical lines show the position of the extraction sextupoles.
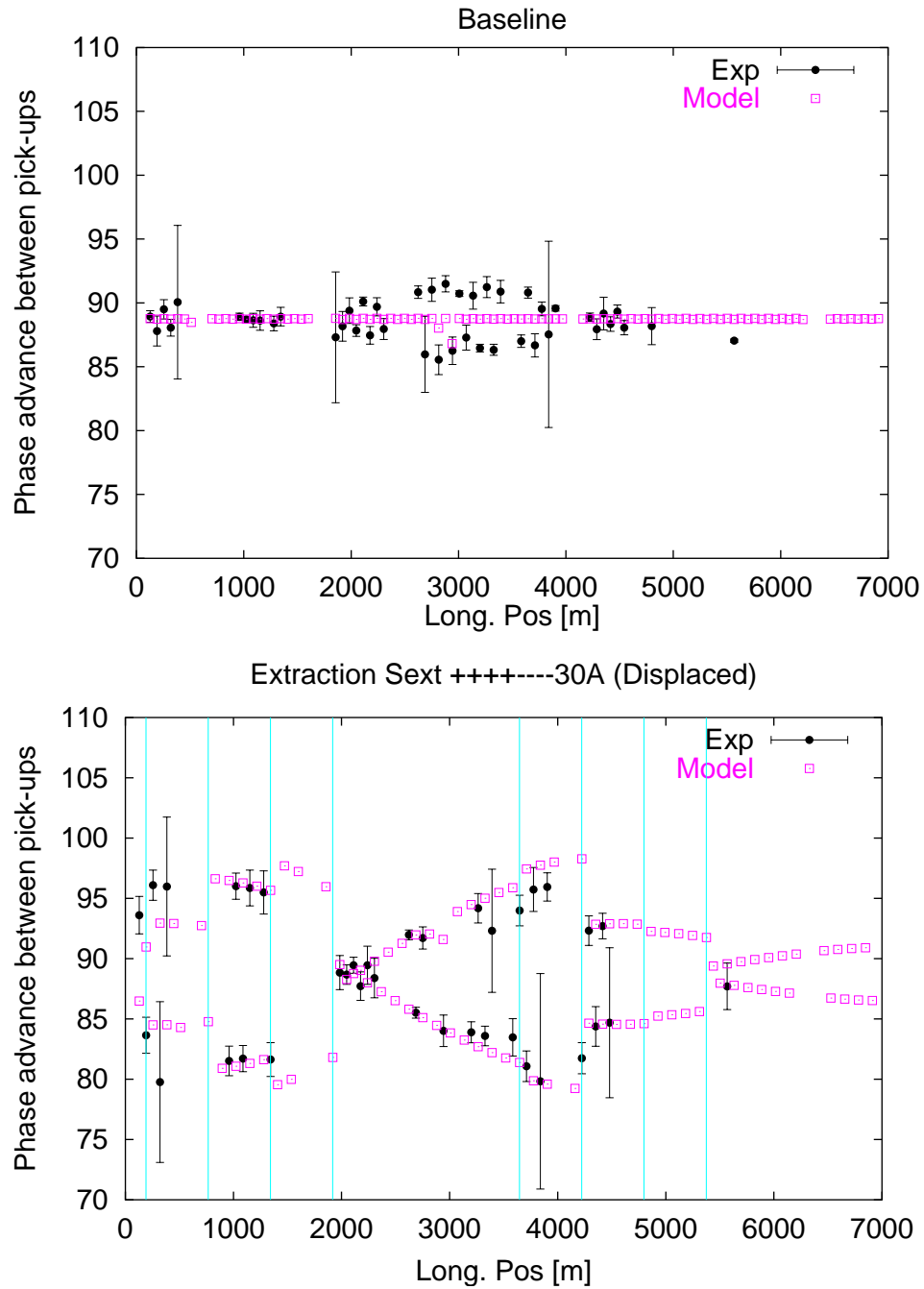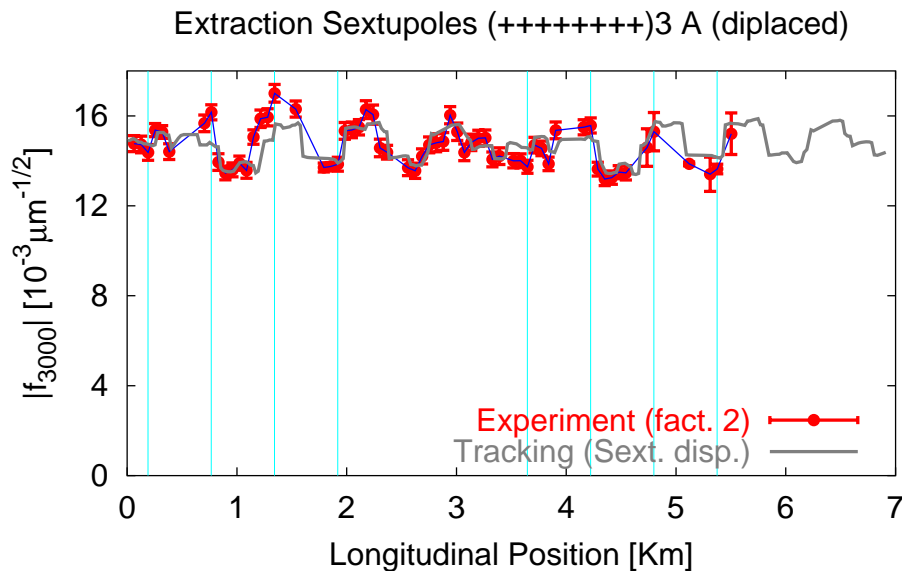

Figure 7.17: Amplitude of the term f_{3000} versus longitudinal position from experiment and the tracking model with the extraction sextupoles $(+ + + + + + + +)3$ A. The decoherence of two is applied to the experimental data. The horizontal tune is 26.662. The blue line is used to connect the experimental points. The vertical lines show the position of the extraction sextupoles.

versus the longitudinal position together with the tracking model containing the closed orbit at the extraction sextupoles. Since the beam data were decohered a factor of two had to be applied to the experimental values. As predicted by the theory, the closer the tune is to the third order resonance the smaller the relative variation of $|f_{3000}|$ is around the ring.

7.3   Experiments at 26 and 80 GeV in 2002

Energy [GeV]	26	80
Intensity [number of protons]	$[0.5, 6] \times 10^{10}$	3.5×10^{10}
Number of bunches	1	1
Nominal Tunes $[Q_x, Q_y]$	26.18, 26.22	26.18, 26.22
Chromaticities $[Q'_x, Q'_y]$	1.3, 1.3	1.0, 1.0

Table 7.4: Measured beam conditions for the experiments in 2002.

During the previous year the measurement of sextupolar resonance driving terms could not be done in some regions of the SPS due to the failure of the BPM system. As well, local discrepancies between model and experiment could not be explained. These discrepancies may arise from linear lattice errors, incorrect strengths of lattice sextupoles, remanent fields in the dipoles or collective effects. In 2002 the goals were to have measurements from all the BPMs of the ring by optimizing the system [31] and to try to determine what are the most likely sources of disagreement. The effect of remanent fields should decrease with the increase of the energy of the beam. Then by performing the measurements at different energies, 26 and 80 GeV, we expected to see the effect of these remanent fields. Collective effects vary with the intensity of the beam, therefore measurements were performed at different intensities to exclude those contributions to the measurement that are not related to nonlinearities. Furthermore important aspects of the technique needed to be studied in detail in order to ameliorate it, e.g. the possibility of measuring higher order resonance driving terms and the phases of the sextupolar resonance terms.

The beam conditions during the experiments in 2002 are listed in table 7.4. The procedure of the experiments carried out this year is almost identical to that of 2001, already described in section 7.2. In particular the BPM pre–analysis reveals this time very few bad BPMs, compared to the previous year when almost all the BPMs of two sextants of the machine had to be discarded. In the following the results from the different studies are discussed and compared to predictions from the model.

7.3.1 Measurement of linear coupling at 26 GeV

In 2001 the technique for the measurement and compensation of the linear coupling was optimised, see section 7.2.2. In figure 7.18 (top) the average amplitude of the coupling resonance term is plotted versus the strength of the skew quadrupoles. The smaller error bars, compared to those from the previous year, are due to the improvement of the BPM system. The optimum setting is obtained by performing the fit shown in the figure. In the same figure (bottom) the amplitude of the coupling term is plotted versus the longitudinal position for two settings of the skew quadrupoles. It is interesting to note that for the optimum setting this term varies smoothly around the ring, therefore the coupling sources should be distributed around the ring. The first spike (from left to right) appearing on this figure has been identified as a bad pick–up. The second spike involves 4 pick–ups and it was investigated weather this could be due to a rotated element found on that region. This spike disappeared in measurements done later which makes it difficult to conclude about the significance of these peaks.

7.3.2 Measurement of sextupolar resonance terms at 26 GeV

The amplitude of the sextupolar term f_{3000} for the baseline machine is computed as explained in section 7.2.3. The result compared to the model is shown in figure 7.19. The level of agreement is similar to that obtained in previous measurements but with smaller variations which is a consequences of chosing a different working point.

The quality of the data also allows a measurement of the phase of the spectral line (–2, 0). An insight into the properties of the phases of the spectral lines follows. From eq. (3.38) the amplitude and phase of the spectral line $(1-j+k, m-l)$ are given by the following complex quantity,

$$-2ij\,f_{jklm}(2I_x)^{\frac{j+k-1}{2}}(2I_y)^{\frac{l+m}{2}}e^{i[(1-j+k)\psi_{x0}+(m-l)\psi_{y0}]}\,. \tag{7.7}$$

The term f_{jklm} is proportional to the sum over all non–linear elements of the same type, i.e.

$$\sum_n k_n e^{i[(-j+k)\psi_{xn}+(m-l)\psi_{yn}]}\,, \tag{7.8}$$

where all the factors as beta functions and strenghts are contained in k_j. Using these expressions the change in the phase of the spectral line $(1-j+k, m-l)$ over a region free of non–linear sources is computed. Let the betatron phases change by $\Delta\psi_x$ and $\Delta\psi_y$ over this region. Then all the ψ_{xj} and ψ_{yj} change by $-\Delta\psi_x$ and $-\Delta\psi_y$ respectively. The changes in the phase of the spectral line are given by the sum of the change of the phase of the term f_{jklm} plus the change of the phase of the exponential part of eq. (7.7), which yields

$$(j-k)\Delta\psi_x + (l-m)\Delta\psi_y + (1-j+k)\Delta\psi_x + (m-l)\Delta\psi_y = \Delta\psi_x\,. \tag{7.9}$$
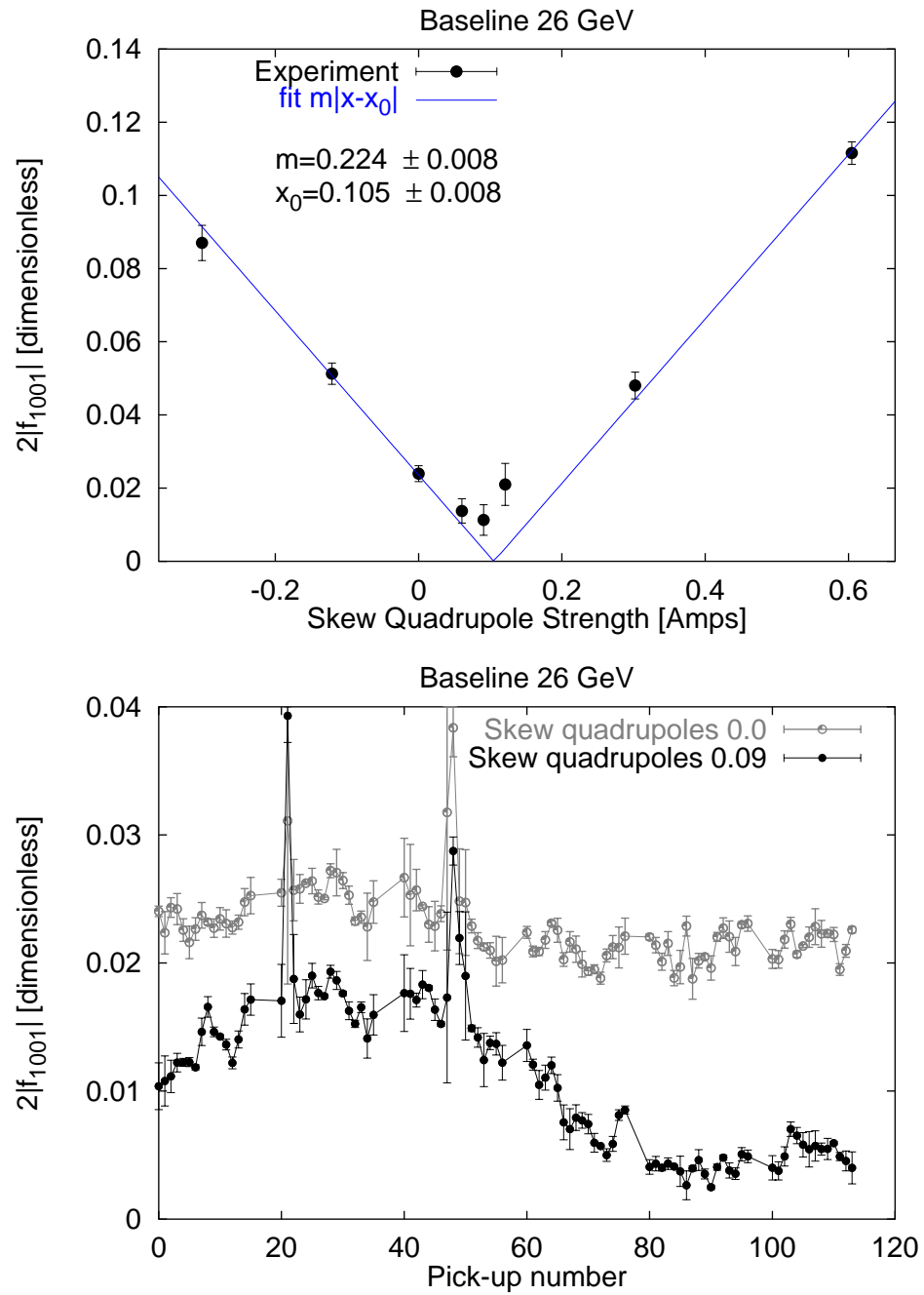
Figure 7.18: Top: Coupling resonance term versus the strength of skew quadrupoles. Bottom: Coupling term as a function of the longitudinal position for two different strengths of skew quadrupoles.
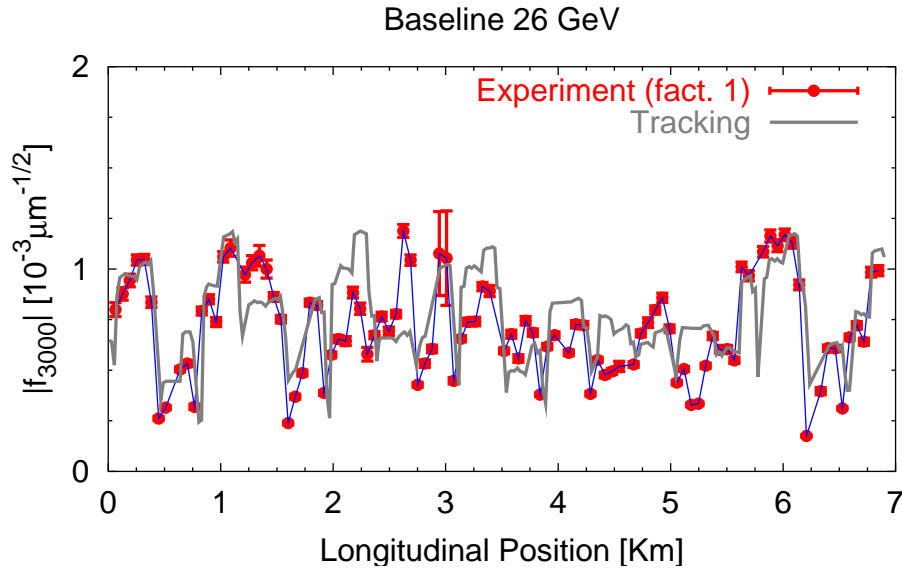
Baseline 26 GeV

Figure 7.19: Amplitude of the generating function term f_{3000} versus longitudinal position from experiment and tracking model for the baseline machine at 26 GeV. The blue line is used to connect the experimental points.

This means that the phase of all the spectral lines from the horizontal motion changes by the same amount, $\Delta\psi_x$, over a region free of non–linear sources. In particular this is apparent for the horizontal tune line. Therefore, the following observable remains constant along sections free of non–linear sources for any m and n,

$$\phi(m, n) - \phi(1, 0) \ , \tag{7.10}$$

where $\phi(m, n)$ represents the phase of the spectral line with frequency $mQ_x + nQ_y$. This phase observable changes abruptly at the location of the non–linear sources as can be seen from eq. (5.10). The use of this phase observable in conjuction with the amplitude of the spectral line allows the unambiguous localisation of non–linear fields. In figure 7.20 this phase observable as measured from one single run is plotted together with the model prediction versus the longitudinal location for the baseline machine at 26 GeV. Due to the fact that experiment and model have different phase origins a constant quantity had to be added to the experiment values to meet the model prediction.

As in previous years measurements were also done with the extraction sextupoles powered to $(+ + + + - - - -)$ 30 A. In figure 7.21 the amplitude of the term f_{3000} is plotted versus the longitudinal location together with the prediction from the model. Since the data was decohered, a factor two is applied to the experiment in order to compare to the single particle simulation. The closed orbit offsets at the extraction sextupoles were introduced in the model as in the previous year.
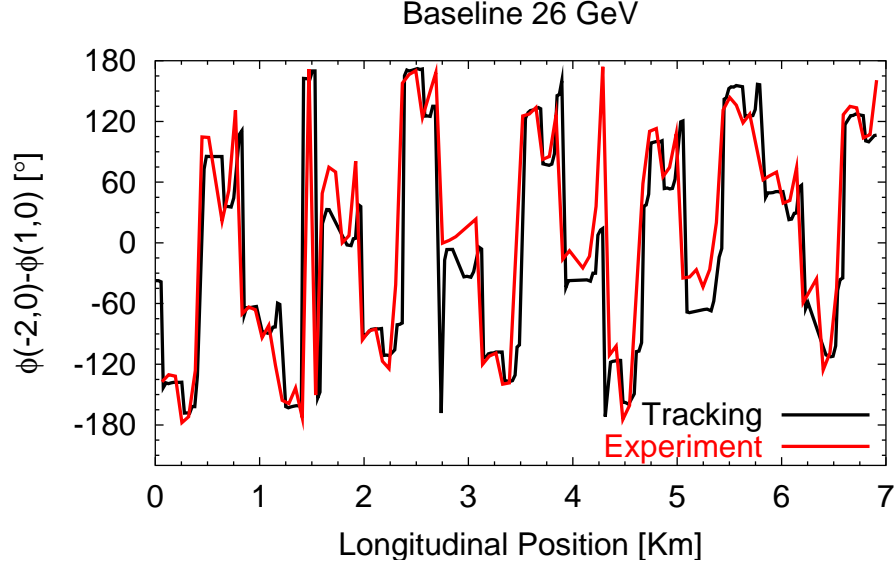
Figure 7.20: Phase of the spectral line (–2,0) minus the phase of the spectral line (1,0) versus longitudinal position from experiment and tracking model for the baseline machine at 26 GeV.

The eigth locations of the sextupoles are clearly seen by the abrupt changes of the measurement and model. The higher amplitudes measured show to be systematicly smaller than the model prediction by around a 20%. This disagreement has not been understood and no possible improvement of the model has been found. On the contrary the smaller amplitues are in very good agreement with the model.

In figure 7.22 the phase of the spectral line (–2, 0) minus the phase of the spectral line (1,0) is plotted versus the longitudinal position for experiment and model. The overall agreement is also good but the curve from the measurement is clearly more ragged than the one from the model.

Sextupoles also introduce non–linear coupling, the horizontal component of the magnetic field is proportional to the product of the transverse coordinates, as shown in eq. (2.10). This monomial introduces, among others, the term h_{0120} in the Hamiltonian and this term contributes to the vertical motion in the following way,

$$
\begin{aligned}
h_y^-(N) \quad = \quad & \sqrt{2I_y}e^{i(2\pi\nu_y N+\psi_{y_0})} \\
& -4if_{0120}(2I_x)^{\frac{1}{2}}(2I_y)^{\frac{1}{2}}e^{i[-(2\pi\nu_x N+\psi_{x_0})-(2\pi\nu_y N+\psi_{y_0})]} \quad . (7.11)
\end{aligned}
$$

The term h_{0120} introduces the spectral line (–1,–1) in the vertical turn–by–turn motion. After normalizing to the amplitude of the vertical tune the amplitude of this spectral line is $4|f_{0120}|\sqrt{2I_x}$. This quantity is linear in the horizontal kick. For this reason the amplitude of the term f_{0120} can be measured by performing a linear fit

Figure 7.21: Amplitude of the term f_{3000} versus longitudinal position from experiment and tracking model for SPS with the extraction sextupoles powered to $(+ + + + - - - -)$ 30 A at 26 GeV. The blue line is used to connect the experimental points. The vertical lines denote the position of the extraction sextupoles.

Figure 7.22: Phase of the spectral line $(-2,0)$ minus the phase of the spectral line $(1,0)$ versus longitudinal position from experiment and tracking model for SPS with the extraction sextupoles powered to $(+ + + + - - - -)$ 30 A at 26 GeV. The blue line is used to connect the experimental points. The vertical lines denote the position of the extraction sextupoles.
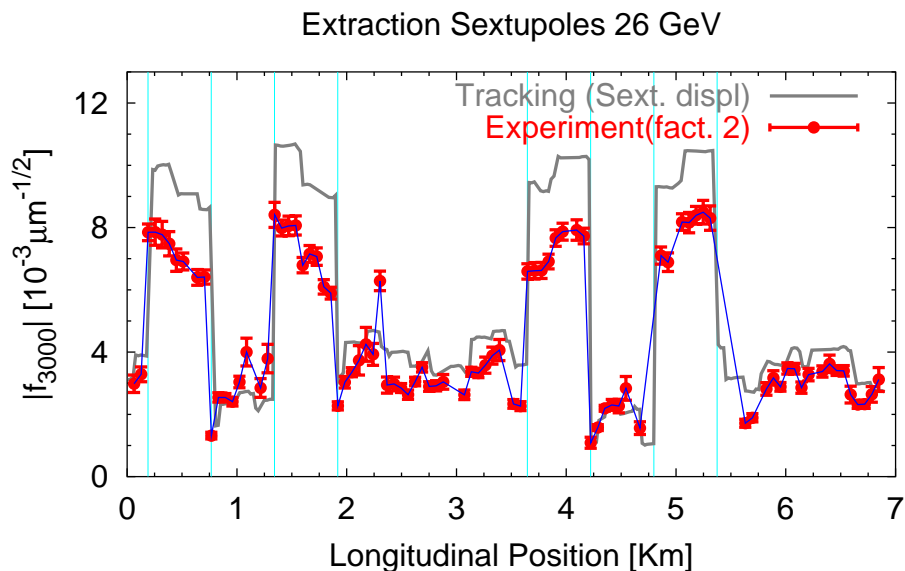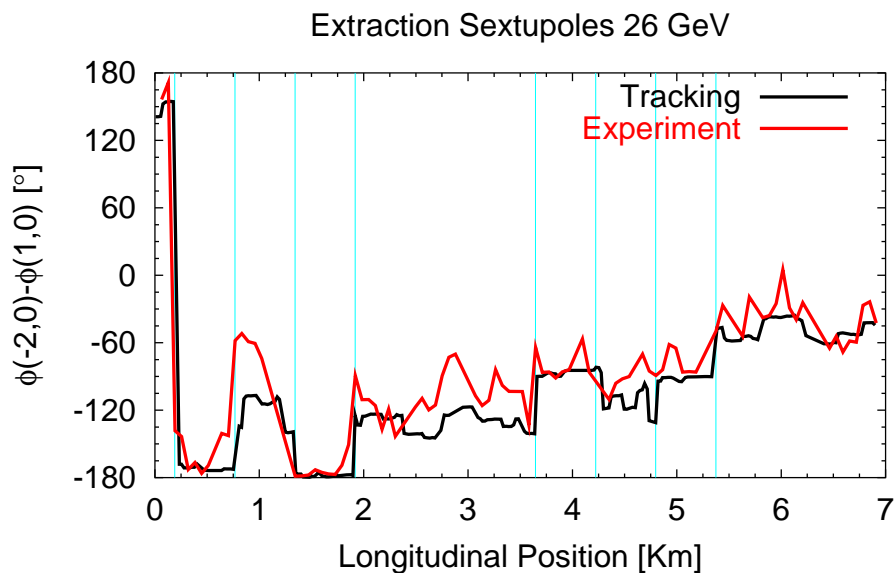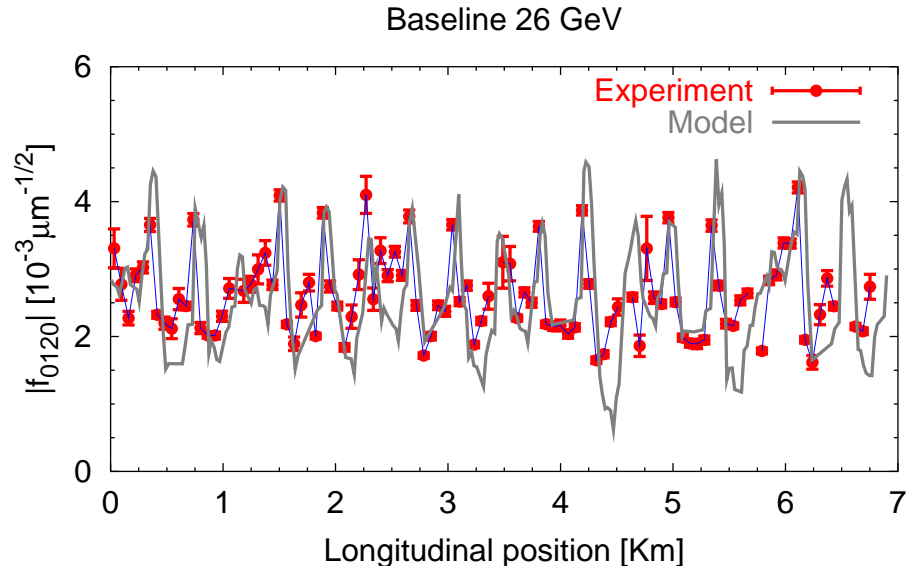
Figure 7.23: Amplitude of the term f_{0120} versus longitudinal position from experiment and tracking model for the baseline machine at 26 GeV. The blue line is used to connect the experimental points.

in a similar way than in section 7.2.3. In presence of decoherence the reduction factor of this spectral line has to be numerically computed since analytical expressions have not been derived here for the two dimensional case. The data acquired for the baseline machine was not decohered therefore it can be directly used to compute this resonance term. In figure 7.23 the amplitude of the generating function term f_{0120} is plotted versus the longitudinal location together with the model. The agreement seems to be better than that obtained for the term f_{3000}, for the baseline machine (see figure 7.19).

7.3.3 Measurement of sextupolar resonance terms at 80 GeV

In this section the measurements are discussed that have been done at an energy of 80 GeV. In figure 7.24 the amplitude of the term f_{3000} is plotted versus the longitudinal position   from experiment and tracking model for the baseline machine. To assess the effect of the energy this is compared to the case at 26 GeV shown in figure 7.19. The level of agreement between experiment and model is similar at both energies, therefore energy effects are not relevant. In figure 7.25 the phase observable $\phi(-2,0) - \phi(1,0)$ is plotted versus the longitudinal position for experiment and model. The level of agreement is similar comparing to the 26 GeV case (see figure 7.20).

Measurements were also done with the extraction sextupoles powered to $(+ + + + - - - -)100$ A. Since the energy is around three times larger than the previous

Figure 7.24: Amplitude of the term f_{3000} versus longitudinal position from experiment and tracking model for the baseline machine at 80 GeV. The blue line is used to connect the experimental points.
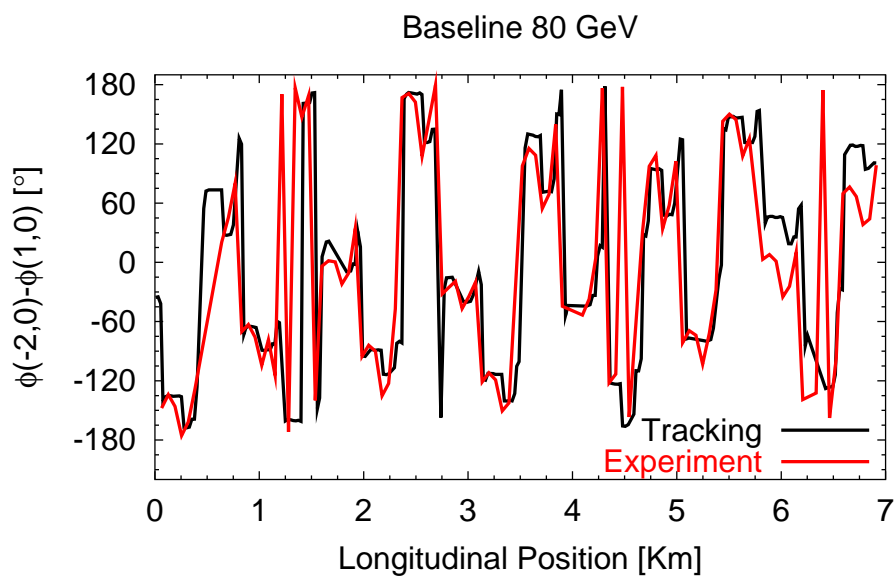
Figure 7.25: Phase of the spectral line (–2,0) minus the phase of the spectral line (1,0) versus longitudinal position from experiment and tracking model for the baseline machine at 80 GeV.

Figure 7.26: Amplitude of the term f_{3000} versus longitudinal position from experiment and tracking model for the SPS with extraction sextupoles powered to $(+ + + + - - - -)100$ A at 80 GeV. The blue line is used to connect the experimental points. The vertical lines denote the position of the extraction sextupoles.
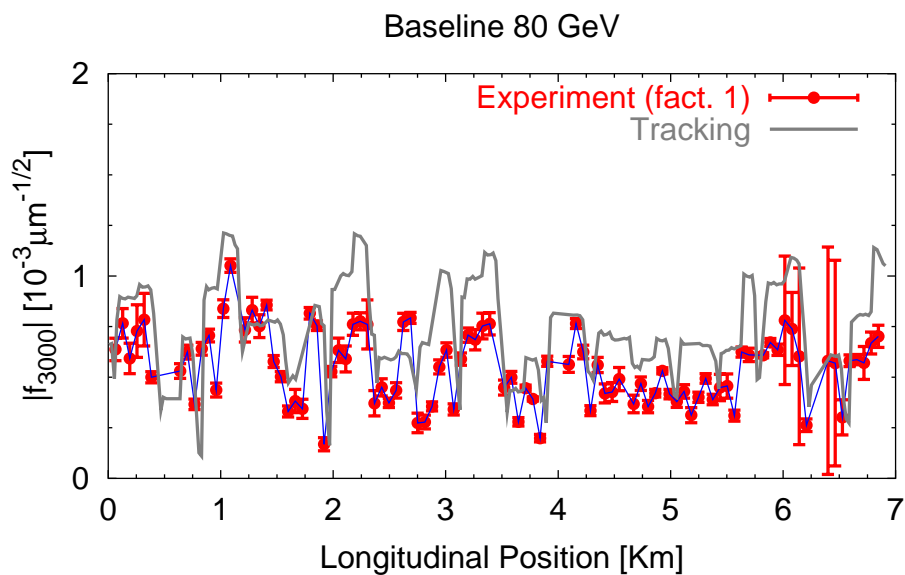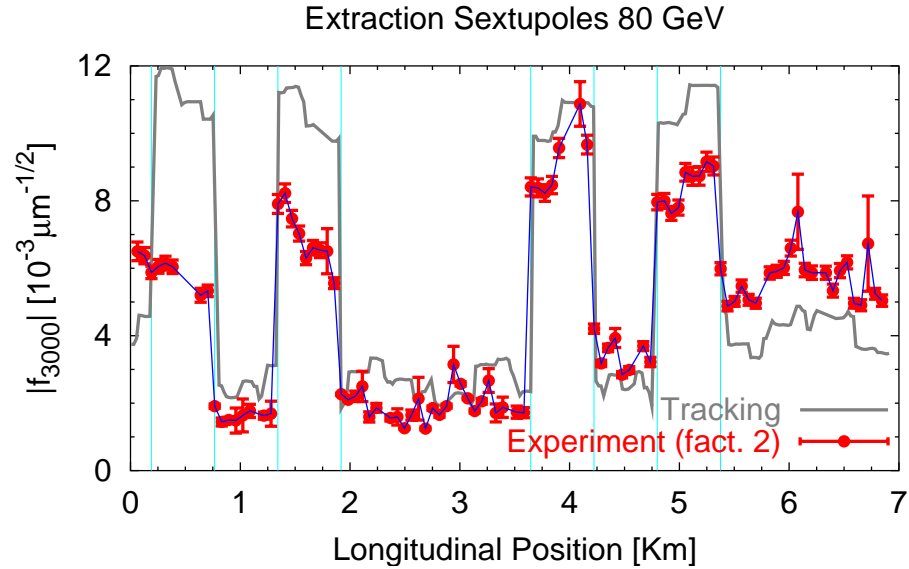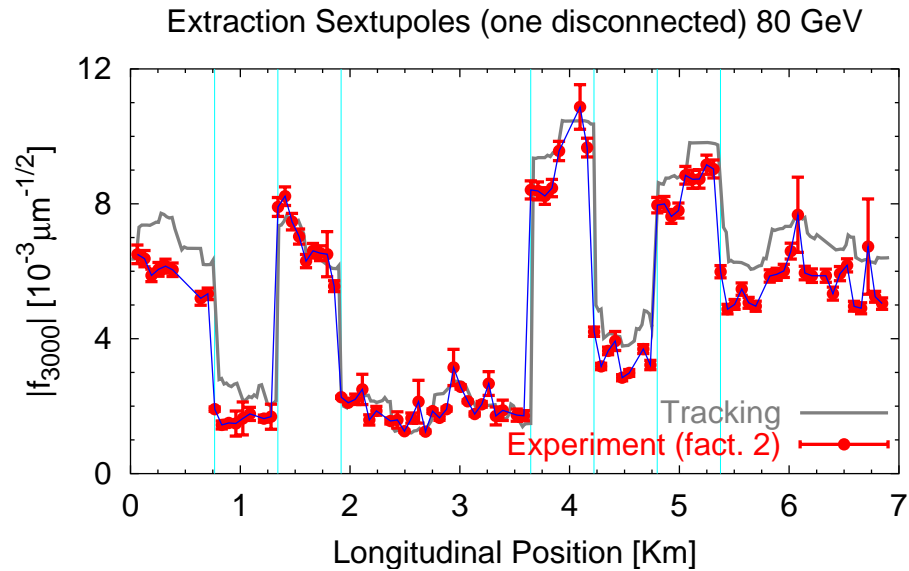

Figure 7.27: Amplitude of the term f_{3000} versus longitudinal position from experiment and tracking model for SPS with one sextupole disconnected $(+ + + - - - -)$ 100 A at 80 GeV. The blue line is used to connect the experimental points. The vertical lines denote the position of the extraction sextupoles. Note that there is one less sextupole with the polarity "+".

26 GeV, also the current in the sextupoles has to be increased by a similar factor to obtain a similar effect in the amplitude. In figure 7.26 the amplitude of the generating function term f_{3000} is plotted versus the longitudinal position together with the model results. A factor two is applied to the data in order to restore the effect of decoherence. Model and measurements show large discrepancies. Looking at the location of the first extraction sextupole a clear discrepancy is observed. Whereas the model predicts a huge change of the amplitude of this term, the measurement keeps constant in that region. These could mean that this extraction sextupole was not connected. A comparison of the data with this new model without the first sextupole shows a good agreement, figure 7.27. This hypothesis of a disconnected sextupole has been confirmed via the SPS alarm system [38]. This is another success of this technique in the sense that we are able to identify on–line a mispowered sextupole.

7.3.4   Comparison of sextupolar terms at different intensities at 26 GeV

The aim of this experiment is to study the effect of the beam intensity in the amplitude detuning and in the measurement of the resonance driving terms. These quantities might depend on the beam intensity due to space charge and impedance effects [39]. During the experiment the beam intensity was changed to different values in the range from 0.5×10^{10} to 6×10^{10} protons. The PS provided the intensity of 6×10^{10} protons and it was reduced in the SPS by scraping with the fast scrapers. Several horizontal single kicks were applied at all the different intensity settings to measure the amplitude detuning and the resonance driving terms.

The tune for every kick amplitude and for every intensity setting is computed by averaging the tune measured from all the pick–ups. To estimate the random errors three sets of data are analyzed for the same kick and intensity settings. In figure 7.28 the detuning curves are shown for the four different intensities with the error bars corresponding to the rms value from the three measurements. The highest intensity has slightly larger detuning. Performing a linear fit for the four curves of figure 7.28 the amplitude detuning is represented by the slope of the fit. In figure 7.29 this slope is plotted versus the intensity with the corresponding errors. There seems to be an effect only for the highest intensity of 6.0×10^{10}. It should be noted that for the resonance driving terms experiments the intensity was always below 3.0×10^{10} protons, i.e. in the region free of any effect.

The resonance (3,0) is driven by the resonance term h_{3000}, or equivalently by the generating function term f_{3000}. This resonance introduces the spectral line (–2, 0) whose amplitude is proportional to the generating term f_{3000}. From theory the amplitude of the spectral line (–2, 0), normalized to the amplitude of the tune line, is proportional to the kick amplitude. In figure 7.30 the normalized amplitude of this spectral line averaged over all pick–ups is plotted versus kick amplitude for the four different intensities. The differences remain inside the error bars. By using the data from all the pick–ups the generating term f_{3000} is obtained around the ring. In figure 7.31 the amplitude of these terms is shown versus the longitudinal
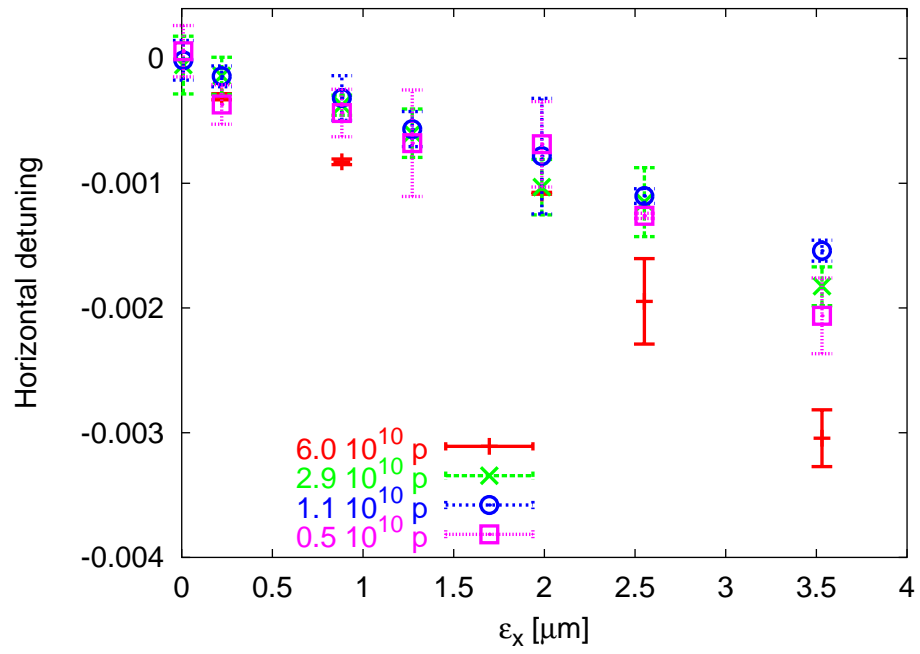
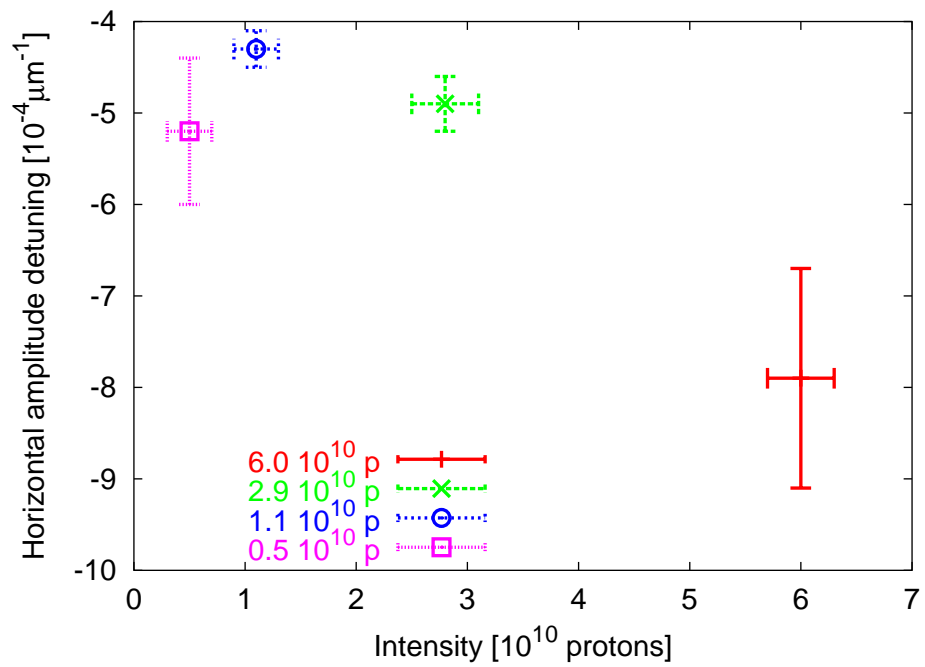Figure 7.28: Horizontal amplitude detuning for the four different intensities.

Figure 7.29: Slope of the amplitude detuning versus beam intensity.
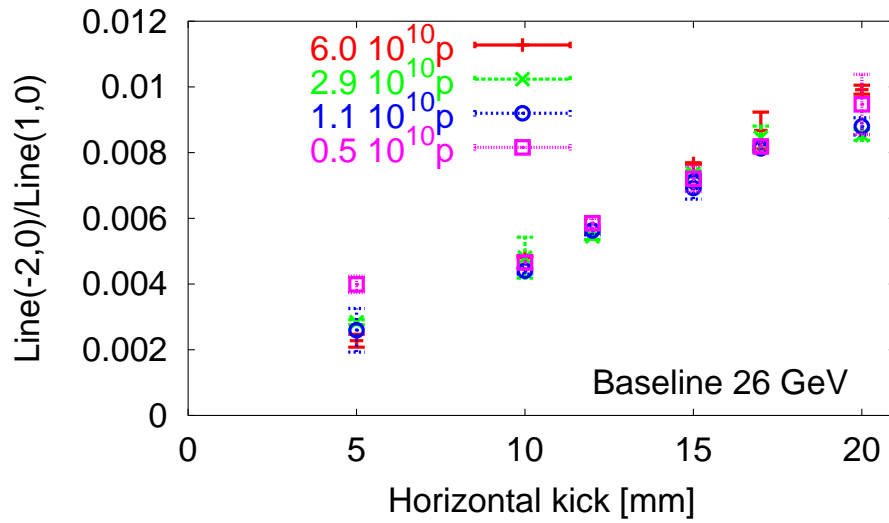
Figure 7.30: Normalized amplitude of the spectral line (–2,0) versus kick amplitude for the four intensity settings.
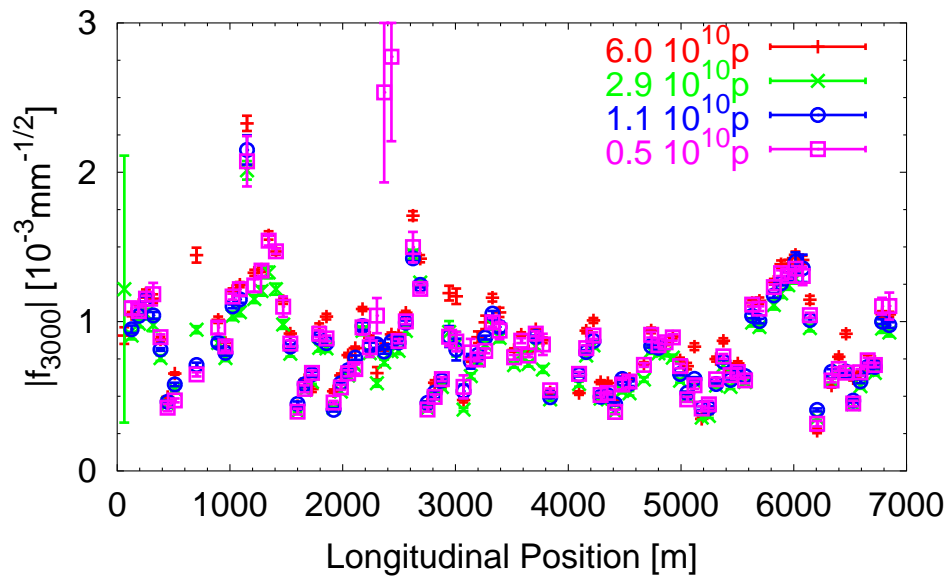

Figure 7.31: Amplitude of the generating function term f_{3000} along the ring for the four intensity settings.

position for the four intensities. The discrepancies of these curves are very small and not correlated to the intensity.

7.3.5 Measurement of octupolar resonance terms at 26 GeV

The resonance driving term h_{4000} drives the resonance (4,0), has associated the spectral line (–3, 0) and is produced in the first order by octupolar fields. The contribution of this term to the horizontal motion is given by the following expression, using eq.(3.38),

$$h_x^-(N) \quad = \quad \sqrt{2I_x}e^{i(2\pi\nu_x N + \psi_{x0})} - 8if_{4000}(2I_x)^{\frac{3}{2}}e^{-i3(2\pi\nu_x N + \psi_{x0})} . (7.12)$$

After normalization the amplitude of the spectral line (–3, 0) is quadratic in the amplitude of the betatron oscillation. In order to compute the resonance term f_{4000} a linear fit in the square of the kick should be performed. The main obstacle for the measurement of this spectral line is the small amplitude that it has at the standard SPS parameters. To enlarge this amplitude the tunes should be moved closer to the fourth integer. During the experiments of this year the fractional part of the tune was moved from 0.18 to 0.26 to enlarge the octupolar effect. Data was acquired for different kick amplitudes. The data is Fourier analyzed and the spectral line (–3, 0) is identified. The amplitude of this spectral line, normalized to the tune line, is plotted versus the square of the kick amplitude in figure 7.32. Data comes from a single horizontal BPM and the error bars are the standard deviation of the value obtained for three different data acquisitions. Note that this spectral line is only visible at large kicks and the error bars are large. From the slope of the fit, $m_{(-3,0)}$, and from eq. (7.12) the amplitude of the term f_{4000} is inferred,

$$|f_{4000}| \quad = \quad \frac{1}{8}\left(\frac{m_{(-3,0)}}{0.094^2}\right) \left[\mu\text{m}^{-1}\right] . \tag{7.13}$$

In figure 7.33 the amplitude of this term for all the pick–ups is plotted versus the longitudinal coordinate together with the prediction from the model containing octupoles and sextupoles. In a few regions the measurement and the simulation differ considerably. This discrepancy maybe due to octupolar unknown sources located at a few places, which might be identified from the plot. It is also important to note that up to now it has been assumed that the octupolar fields are the only ones contributing to the spectral line (–3, 0). But this is not true, second order contributions from the sextupolar fields to the line (–3, 0) are the most important for the SPS. In figure 7.33 the quantity $|f_{4000}|$ is shown for a lattice without octupoles. This shows that second order contributions from the sextupoles are very relevant. Therefore, the small discrepancies found for the sextupolar terms of the baseline machine (see figure 7.19) must show up again as discrepancies for the octupolar terms. In conclusion, the octupolar spectral line has been measured with a larger uncertainty than the sextupolar spectral lines and the observed disagreement when compared to the model could be due to unknown octupolar and sextupolar sources.
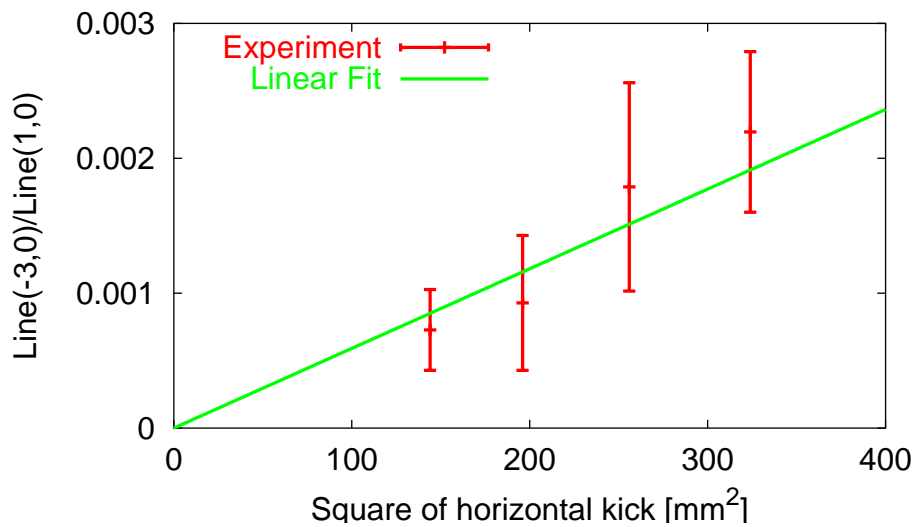
Figure 7.32: Normalized amplitude of the spectral line (–3,0) versus the square of the kick amplitude for SPS at 26 GeV close to the forth order resonance. Experimental data and a linear fit are shown.
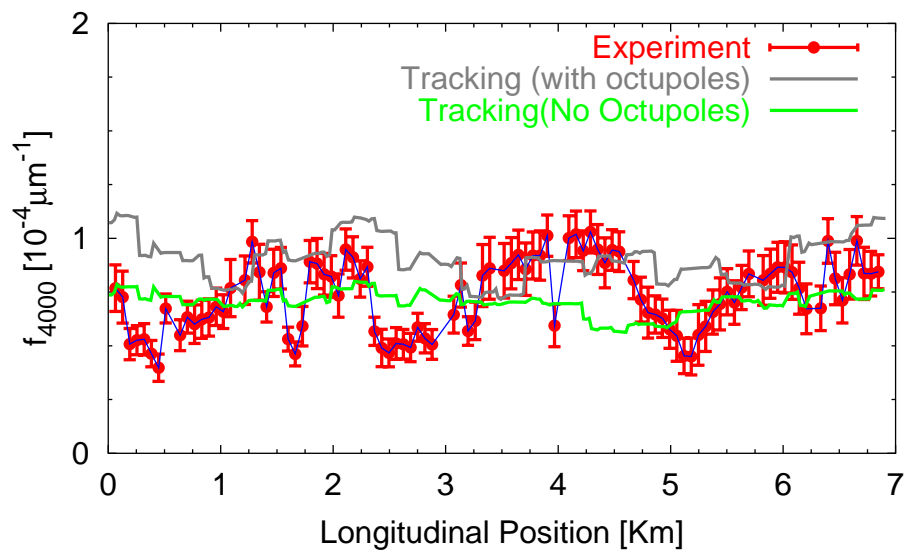
Figure 7.33: Amplitude of the generating function term f_{4000} versus longitudinal position from experiment and tracking model for SPS at 26 GeV close to the forth order resonance.

Chapter 8

RHIC experiment

In a collaboration between BNL and CERN an experiment has been carried out at the RHIC, BNL. The aim of this experiment is to prove the feasibility of the measurement of resonance driving terms in a superconducting machine. The RHIC serves as an ideal testbed for preparing this technique for the LHC. Results of the experiment are presented, including a direct measurement of sextupolar resonances and a comparison to the model.

8.1   Description of the RHIC model

The RHIC tracking model is constructed from an ideal lattice, characterized by a β–function of 10 m at all interaction points. The magnetic field errors are introduced in the arc dipoles and quadrupoles. At injection energy, these field errors dominate the dynamic aperture. The tracking program SixTrack [23] is used for all the analysis.

For the dipoles, cold measurements at 660 A in 58 magnets are used to determine the average and rms values for the systematic field errors [40, 41]. Normal and skew components are measured up to 22–poles with the dipoles powered with 470 A. The measured mean and rms values are used to assign random errors in the lattice. Mean and rms values for the sextupole component, dominated by persistent currents, are determined in a separate measurement, and also used to assign random errors in the lattice.

For the quadrupoles, only systematic errors are considered. The mean and the rms values are measured in 380 magnets powered with 30 A at room temperature. A good correlation is found between warm and cold measurements in these magnets [40, 41]. No additional persistent current error contributions are included in the quadrupoles.

Tunes and chromaticities are set to the values measured during the experiment. Closed orbit errors are disregarded. In the experiment one interaction region sextupole corrector was used as a probe to excite the third order resonance.

Table 8.1: Machine and beam parameters for the experiment.

parameter	unit	value
used ring		Yellow
specie		Au^{79+}
relativistic parameter γ		10.52
ions per bunch N_b	10^9	$0.1 - 0.7$
norm. emittance, 95% $\epsilon_{x,y}$	μm	≈ 10
tunes (ν_x, ν_y)		(28.223, 29.235)
chromaticities (Q'_x, Q'_y)		$\approx (-2, -2)$

8.2   Description of the experiment

The measurement of resonance driving terms was carried out in gold operation
at injection energy. Relevant parameters are displayed in Tab. 8.1. In all cases
the transverse injection oscillations of a single bunch were observed turn–by–turn.
The horizontal oscillation amplitude was varied by changing the strength of the
injection septum. The oscillation amplitudes were increased in steps until most of
the beam was lost in the injection process. Twelve beam position monitors (BPMs)
in either plane recorded 1024 turns after the injection.

   Five sets of data were taken. In each set the horizontal oscillation amplitude
was varied. The first set was taken with the baseline machine. For the other sets,
the single interaction region sextupole used as a probe was powered to a normalized
strength of 0.09, 0.03, –0.03 and –0.09 m^{-2} respectively. This sextupole should
drive first and third order resonances.

   The sextupole that was changed in the experiment is at a location with lattice
functions $(\beta_x, \beta_y) = (143 \text{ m}, 50 \text{ m})$. For comparison, the 72 focusing arc sex-
tupoles are at locations $(\beta_x, \beta_y) = (45 \text{ m}, 11 \text{ m})$ with a normalized strength of
$+0.18 \text{ m}^{-2}$; 72 defocusing arc sextupole are at locations $(\beta_x, \beta_y) = (11 \text{ m}, 44 \text{ m})$
with a normalized strength of -0.39 m^{-2}. The arc sextupoles correct for the nat-
ural chromaticities of $(Q'_{x,n}, Q'_{y,n}) = (-55, -57)$ and the persistent current chro-
maticities $(Q'_{x,b_2}, Q'_{y,b_2}) = (-38, +36)$ [42].

8.3   Experiment versus model

Sextupolar fields introduce three spectral lines in the Fourier spectrum of the hor-
izontal motion: (–2, 0), (2, 0) and (0, 0). The first one is related to the third order
resonance and the other two are related to the first order resonance. An example
of the Fourier spectrum obtained from the experimental data and using the SUS-
SIX [24] code is shown in Fig. 8.1. In this figure the tune line and the three sextupo-
lar spectral lines are seen plus the spectral line (–1,0) which is due to quadrupolar
and octupolar resonances.

   To measure the spectral line (0,0) the closed orbit previous to the excitation of
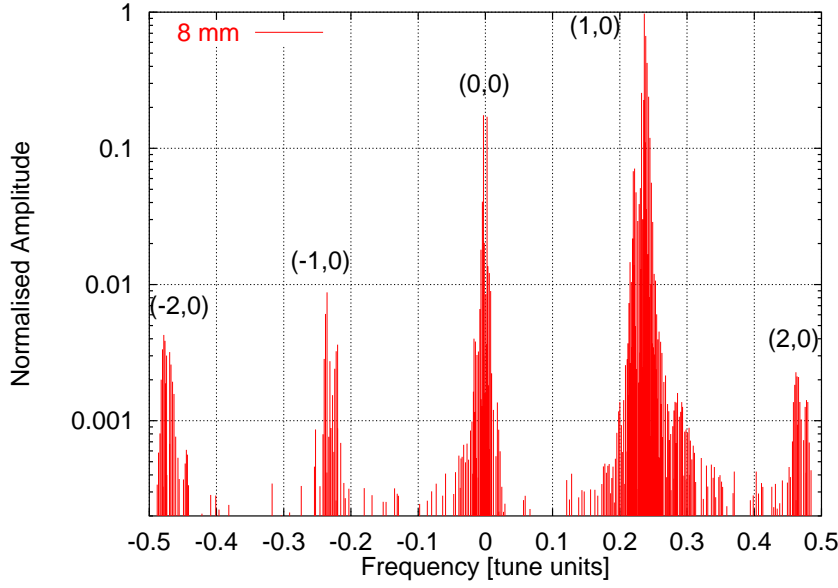
Figure 8.1: Fourier spectrum of the complex signal from pick–ups $yo5$-$bh10$ and $yo5$-$bh12$ for the baseline RHIC machine and for an oscillation amplitude of 8 mm. The label (m,n) means that the frequency is equal to $m\nu_x + n\nu_y$.

the betatron motion is needed. Since in this experiment the betatron motion was excited by injecting with a certain transverse angle, the reference closed orbit is not known. Therefore the line (0,0) cannot be measured. The spectral lines (–2, 0) and (2, 0), normalized to the tune line, are proportional to the oscillation amplitude and to the resonance terms h_{3000} and h_{1200} respectively, as derived from Eq. (3.38). For the different sets of data the normalized amplitude of either spectral line is plotted versus the square root of the single particle emittance. The betatron amplitudes have been measured from the first turns of the BPM data. A beta function of 48 m has been assumed at the BPMs to compute the single particle emittance. Only the data coming from two of the pick–ups could be systematically used for all the different settings. In Fig. 8.2 the normalized amplitude of the spectral line (–2, 0) coming from these BPMs is plotted versus the oscillation amplitude for the five different settings of the interaction region sextupole used as a probe. The experimental values have been multiplied by the decoherence factor of two to compare to the curves predicted by the model. There is a good agreement except for the case with -0.09 m^{-2}. To measure the first order resonance the previous procedure is followed for the spectral line (2, 0). The resulting plots are shown in Fig. 8.3. There is a good agreement for the cases with positive and zero strength. Discrepancies arise for the cases with negative strength. In the case of –0.09 m^{-2} (see Fig. 8.3) the disagreement between experiment and model shows only at large amplitudes.
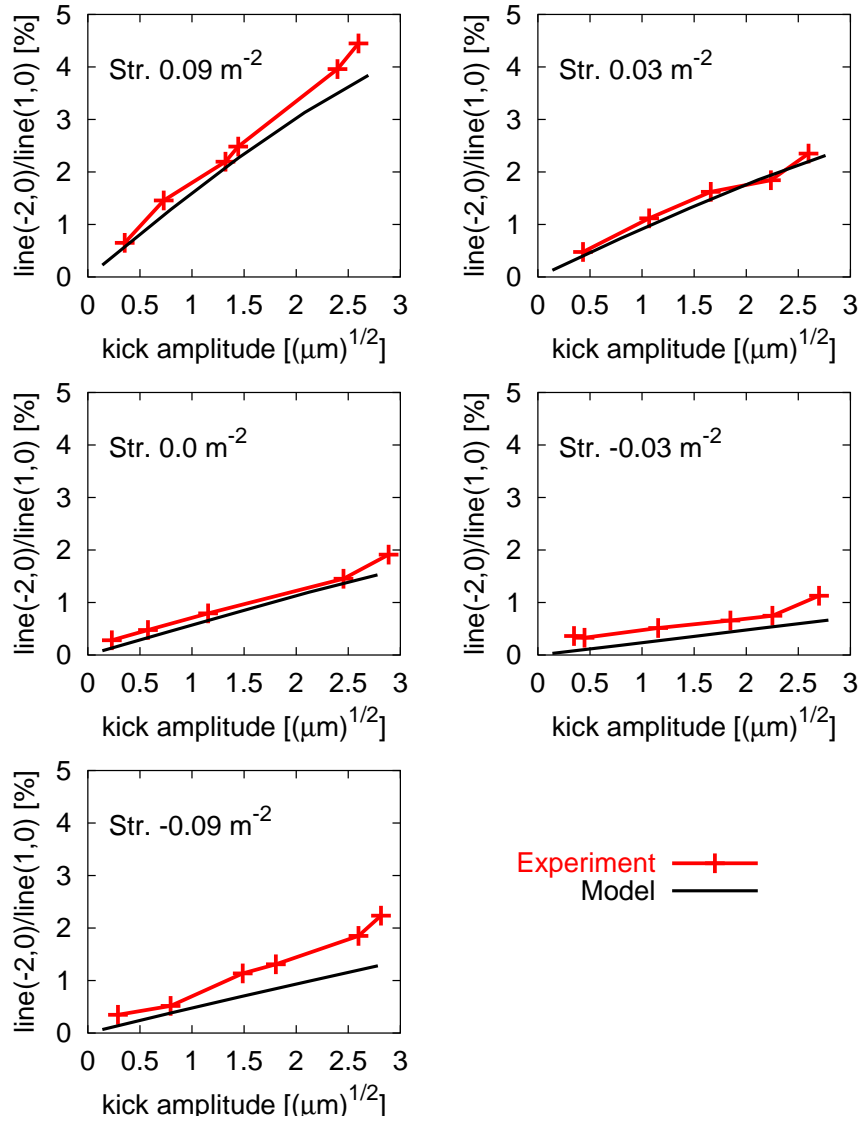
Figure 8.2: Measurement of the third order resonance. The normalized amplitude of the spectral line (–2,0) is plotted versus horizontal betatron amplitude for five different strengths of the probe sextupole. Experimental results are multiplied by the decoherence factor of 2 and predictions from the model are shown.
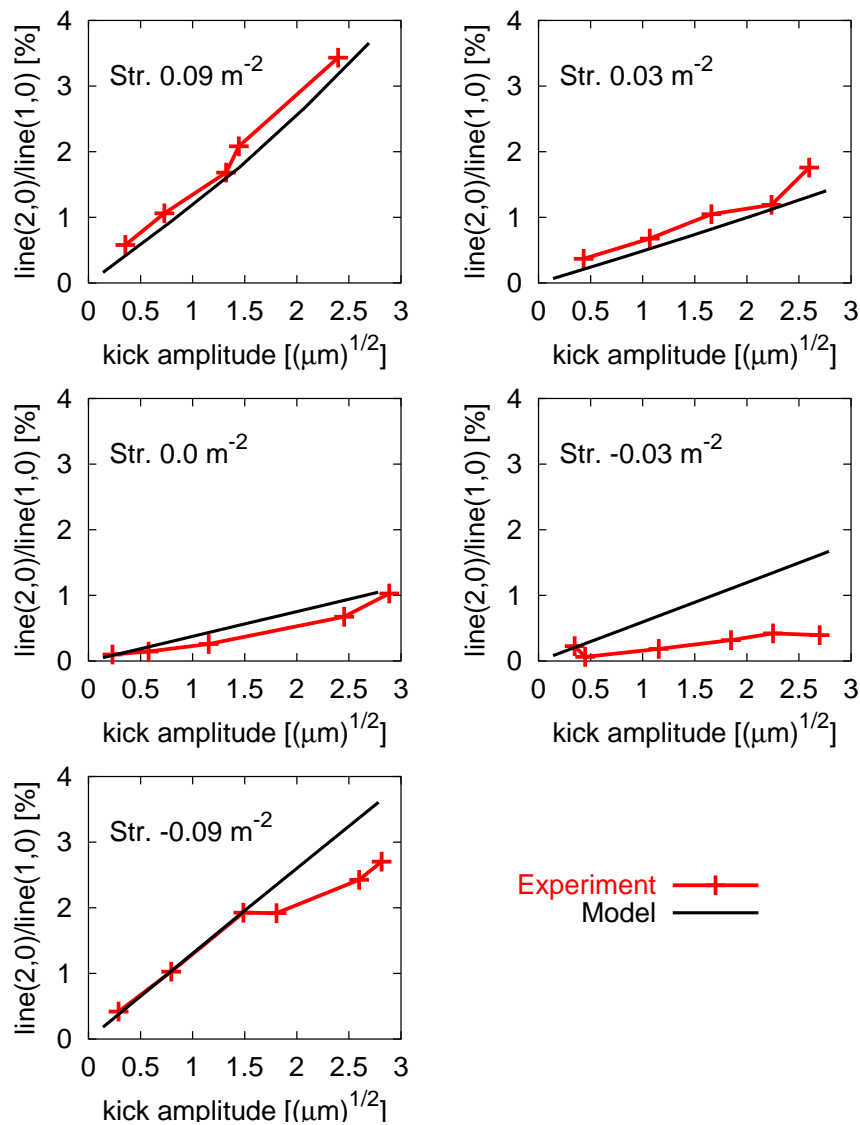
Figure 8.3: Measurement of the first order resonance. The normalized amplitude of the spectral line (2,0) is plotted versus horizontal betatron amplitude for five different strengths of the probe sextupole. Experimental results are multiplied by the decoherence factor of 2 and predictions from the model are shown.

8.4   Summary of the RHIC experiment

For the first time we were able to demonstrate that sextupole driving terms can be measured in RHIC, an operational superconducting machine. We measured two types of horizontal sextupole resonances at RHIC obtaining a good agreement with the model. Important discrepancies for the weaker resonance (1,0) at negative sextupole strenghts remain ununderstood. Due to the non availability of BPM data around the ring the resonance driving terms could be computed only at one location.

Chapter 9

Normal Form of particle motion under the influence of an AC dipole

AC dipoles in accelerators are used to excite coherent betatron oscillations at a drive frequency close to the tune. These beam oscillations may last arbitrarily long and, in principle, there is no significant emittance growth if the AC dipole is adiabatically turned on and off. Therefore the AC dipole seems to be an adequate tool for non–linear diagnostics provided the particle motion is well described in presence of the AC dipole and non–linearities.

Normal Forms and Lie algebra are powerful tools to study the non–linear content of an accelerator lattice. In this chapter a way to obtain the Normal Form of the Hamiltonian of an accelerator with an AC dipole is described. The particle motion to first order in the non–linearities is derived using Lie algebra techniques. The dependence of the Hamiltonian terms on the longitudinal coordinate is studied showing that they vary differently depending on the AC dipole parameters. The relation is given between the lines of the Fourier spectrum of the turn–by–turn motion and the Hamiltonian terms. Furthermore the analytical results are confronted to a tracking simulation using a SPS model.

9.1   Linear motion with an AC dipole.

The simplified Hamiltonian that describes the linear motion of a particle in an accelerator with an AC dipole is given by

$$H_0(x, p_x, s, t) = \frac{1}{2}p_x^2 + \frac{1}{2}K_x(s)x^2 - \delta(s, t)x \ , \qquad (9.1)$$

where x and p_x are the transverse canonical coordinates, s is the longitudinal co-ordinate, $K_x(s)$ is the focusing strength and $\delta(s, t)$ is the time–dependent kick of

the AC dipole placed at the location s_D given by the expression

$$\delta(s,t) = \frac{BL}{(B_0\rho)}\delta_{Dirac}(s - s_D)\cos(2\pi Q_D t + \psi_0) , \qquad (9.2)$$

where BL is the integrated field amplitude, $(B_0\rho)$ is the rigidity, Q_D and ψ_0 are the tune and initial phase of the AC dipole and $\delta_{Dirac}(s - s_D)$ is the Dirac delta function. Note that throughout this chapter the unperturbed linear machine is assumed to be free of transverse coupling to simplify the expressions. A generalization to include linear coupling requires an additional decoupling transformation throughout the formalism [43]. The exact single turn map corresponding to the Hamiltonian of eq. (9.1) at the location just before the AC kick can be found in [44]. Using the Courant–Snyder variables $(\hat{x}, \hat{p}_x)$ this solution is written as function of the turn number N as

$$\hat{x}(N) - i\hat{p}_x(N) = \sqrt{2J}e^{i(2\pi Q_x N + \phi_{x0})} + \delta_- e^{i2\pi Q_D N} - \delta_+ e^{-i2\pi Q_D N} , \quad (9.3)$$

where J and ϕ_{x0} are the linear invariant and the initial phase given by the initial conditions and δ_- and δ_+ are defined as

$$\delta_\pm = \sqrt{\beta_D}\frac{BL}{(B_0\rho)}\frac{e^{\pm i(\pi Q_\pm - \psi_0)}}{4\sin(\pi Q_\pm)} , \qquad (9.4)$$

where β_D is the betatron function at the dipole and $Q_\pm = Q_D \pm Q_x$. Notice that close to the resonance $Q_D = Q_x$ the quantity δ_- is much larger than δ_+.

A general solution for the particle motion at any location of the ring can be computed following the same steps as in [44]. The equivalent expression of eq. (9.3) at the longitudinal location s is given by

$$\hat{x}(N) - i\hat{p}_x(N) = \sqrt{2J}e^{i(2\pi Q_x N + \phi_{x0})} + e^{-i\phi_D}\left(\delta_- e^{i2\pi Q_D N} - \delta_+ e^{-i2\pi Q_D N}\right) , \qquad (9.5)$$

where ϕ_D is the phase advance from the starting location s to the AC dipole. J and ϕ_{x0} are again given by the initial conditions. Notice that ϕ_D has a discontinuity at the AC dipole since right before the AC dipole ϕ_D is zero and right after it ϕ_D equals to $2\pi Q_x$.

9.2   The time–independent linear one–turn map.

In general an explicitly time dependent Hamiltonian can be transformed to a time independent one by introducing an extra degree of freedom (this is equivalent to extend the phase space [45]). The Hamiltonian $H(x, p_x, t)$ generates the same equations of motion for x and p_x as the new Hamiltonian $\overline{H}(x, p_x, \tau, p_\tau)$, defined by

$$\overline{H}(x, p_x, \tau, p_\tau) = H(x, p_x, \tau) + p_\tau , \qquad (9.6)$$

since the solution of the canonical equations for τ is $\tau(t) = t$.

Applying this transformation to the time dependent Hamiltonian of eq. (9.1) a new Hamiltonian independent of time with one extra degree of freedom is obtained. The one turn operator acting on τ is defined to be R_τ, and its action over τ is

$$R_\tau \tau = \tau + 1 \ . \tag{9.7}$$

The total linear one–turn map is the direct product of the one–turn map of the betatron motion with the operator R_τ, this is expressed as $R_x \otimes R_\tau$, where R_x is defined as $R_x \phi_x = \phi_x + 2\pi Q_x$. The turn–by–turn evolution of the particle at the location of the AC dipole is re–expressed as follows

$$\hat{x}(N) - i\hat{p}_x(N) = (R_x \otimes R_\tau)^N [\sqrt{2J} e^{i(\phi_x + \phi_{x0})} + \delta_- e^{i2\pi Q_D \tau} - \delta_+ e^{-i2\pi Q_D \tau}] \ . \tag{9.8}$$

The cross denoting the direct product will be omitted in the following.

9.3 The non–linear one–turn map.

Since the explicit time dependence of the Hamiltonian has been removed the one–turn map including non–linear kicks can be constructed as in [18]. All non–linearities are assumed to be kicks without loss of generality since any Lie map can be factorized into non–linear kicks up to a desired order [46]. The one–turn map is expressed as

$$\mathcal{M} = e^{:\tilde{h}_1:} e^{:\tilde{h}_2:} \cdots e^{:\tilde{h}_N:} R_{x,y} R_\tau \tag{9.9}$$

where $\tilde{h}_n$ are the generating functions of the multipolar kicks written in terms of the eigen–coordinates $(x_n, p_{xn}, y_n, p_{yn})$ at the longitudinal location $s = s_n$. These eigen–coordinates are the quantity inside the square brackets of eq. (9.8) propagated to the location s_n and multiplied by the square root of the beta function at that location. Since eq. (9.8) holds at the location just before the AC dipole, the propagation to s_n is done by applying R_τ and multiplying by an exponential function with the phase advance at s_n. The eigen–coordinates have the following form

$$
\begin{aligned}
x_n - ip_{xn} &= \sqrt{\beta_{xn}} e^{i\phi_{xn}} [\sqrt{2J_x} e^{i(\phi_x + \phi_{x0})} + \delta_{x-} e^{i2\pi Q_{xD}\tau} - \delta_{x+} e^{-i2\pi Q_{xD}\tau}] \ , \\
y_n - ip_{yn} &= \sqrt{\beta_{yn}} e^{i\phi_{yn}} [\sqrt{2J_y} e^{i(\phi_y + \phi_{y0})} + \delta_{y-} e^{i2\pi Q_{yD}\tau} - \delta_{y+} e^{-i2\pi Q_{yD}\tau}] \ ,
\end{aligned}
\tag{9.10}
$$

where β_{zn} and ϕ_{zn} are the beta and phase advance functions at the location of the nth element. The notation has been generalized to include two independent AC dipoles in the horizontal and vertical planes. The set of eigen–coordinates $(x_n, p_{xn}, y_n, p_{yn})$ depends on the initial longitudinal position, which in this case

is just before the AC dipole. In section 9.7 a derivation is presented for an arbitrary initial longitudinal position. Using the Campbell–Baker–Hausdorf theorem, eq. (9.9) can be simplified to

$$\mathcal{M} = e^{:h:} R_{x,y} R_\tau \tag{9.11}$$

where h can be approximated by

$$h = \sum_{n=1}^{N} \tilde{h}_n + \sum_{n,m<n}^{N} [\tilde{h}_m, \tilde{h}_n] + \cdots \tag{9.12}$$

assuming that $\tilde{h}_n$ are small enough. The aim of this study is to derive expressions up to first order in the non–linearities, therefore only the first summation of eq. (9.12) will be kept. In the absence of the AC dipole the standard expansion of h is written as

$$h = \sum_{jklm} h_{jklm} z_x^{+^j} z_x^{-^k} z_y^{+^l} z_y^{-^m} , \tag{9.13}$$

where h_{jklm} are the Hamiltonian terms and $\mathbf{z}$ are the linearly normalized coordinates defined by

$$\begin{aligned}
z_x^{\pm} &= \sqrt{2J_x} e^{\mp i(\phi_x + \phi_{x0})} , \\
z_y^{\pm} &= \sqrt{2J_y} e^{\mp i(\phi_y + \phi_{y0})} ,
\end{aligned} \tag{9.14}$$

where these oscillations would be obtained by applying a kick in either plane. The expansion of h in the presence of the AC dipole is directly computed by replacing the $\mathbf{z}$ in eq. (9.13) by the quantities inside the brackets of eq. (9.10), leading to

$$h = \sum_{jklm} h_{jklm} \xi_x^{+^j} \xi_x^{-^k} \xi_y^{+^l} \xi_y^{-^m} , \tag{9.15}$$

with

$$\begin{aligned}
\xi_x^{\pm} &= \sqrt{2J_x} e^{\mp i(\phi_x + \phi_{x0})} + |\delta_{x-}| e^{\mp i(2\pi Q_{xD}\tau - \eta_{x-})} - |\delta_{x+}| e^{\pm i(2\pi Q_{xD}\tau + \eta_{x+})} , \\
\xi_y^{\pm} &= \sqrt{2J_y} e^{\mp i(\phi_y + \phi_{y0})} + |\delta_{y-}| e^{\mp i(2\pi Q_{yD}\tau - \eta_{y-})} - |\delta_{y+}| e^{\pm i(2\pi Q_{yD}\tau + \eta_{y+})} ,
\end{aligned} \tag{9.16}$$

where, for convenience, the quantities $\delta_{x,y\pm}$ of eq. (9.10) have been separated into an amplitude factor $|\delta_{x,y\pm}|$ and a phase factor $\exp(i\eta_{x,y\pm})$. If the AC dipole is adiabatically turned on the betatron oscillation is not excited, i.e. the terms of eq. (9.16) containing $J_{x,y}$ should vanish. Nevertheless a real AC dipole will always excite the betatron motion up to some level. Therefore the terms containing $J_{x,y}$ are kept until the end of the derivation.

9.4 Normal Form Procedure.

The Normal Form technique [17,19] can be applied to the one turn map of eq. (9.11) containing eq. (9.15). Basically, we look for a new map $e^{:F(J,\phi):}$ which by a similarity transformation brings the one turn map into a rotation $R_{x,y}R_\tau e^{:H(I):}$ that only depends on the new invariants of the motion denoted by I. The equation to find the functions F and $H(I)$ is written as

$$e^{:h:}R_{x,y}R_\tau = e^{:F:}e^{:H(I):}R_{x,y}R_\tau e^{-:F:} \ . \tag{9.17}$$

This is represented by the following diagram

$$
\begin{array}{ccc}
\xi & \xrightarrow{\ e^{:h:}R_{x,y}R_\tau\ } & \xi' \\[2pt]
{\scriptstyle e^{-:F(J,\phi):}}\Big\downarrow & & \Big\uparrow{\scriptstyle e^{:F(J,\phi):}} \\[2pt]
\zeta & \xrightarrow[\ e^{:H(I):}R_{x,y}R_\tau\ ]{} & \zeta'
\end{array}
\tag{9.18}
$$

where ζ represents the Normal Form coordinates $(\zeta_x^+,\zeta_x^-,\zeta_y^+,\zeta_y^-)$ and ξ represents $(\xi_x^+,\xi_x^-,\xi_y^+,\xi_y^-)$. The Normal Form coordinates are related to the linear coordinates by the expression

$$\zeta = e^{-:F_r:}\xi \ , \tag{9.19}$$

where

$$
\begin{aligned}
\zeta_x^\pm &= \sqrt{2I_x}e^{\mp i(\psi_x+\psi_{x0})} + |\delta_{x-}|e^{\mp i(2\pi Q_{xD}\tau-\eta_{x-})} - |\delta_{x+}|e^{\pm i(2\pi Q_{xD}\tau+\eta_{x+})} \ , \\
\zeta_y^\pm &= \sqrt{2I_y}e^{\mp i(\psi_y+\psi_{y0})} + |\delta_{y-}|e^{\mp i(2\pi Q_{yD}\tau-\eta_{y-})} - |\delta_{y+}|e^{\pm i(2\pi Q_{yD}\tau+\eta_{y+})} \ .
\end{aligned}
\tag{9.20}
$$

I_x and I_y are the new action invariants. ψ_x and ψ_y are the new phase variables and τ is the same time–like variable as above. By construction the one–turn map of the Normal Form coordinates is an amplitude dependent rotation represented by

$$
\begin{aligned}
e^{:H(I):}R_{x,y}R_\tau\zeta_x^\pm &= \sqrt{2I_x}e^{\mp i(\psi_x+2\pi Q_x(I,\delta)+\psi_{x0})} \\
&\quad +|\delta_{x-}|e^{\mp i(2\pi Q_{xD}(\tau+1)-\eta_{x-})} - |\delta_{x+}|e^{\pm i(2\pi Q_{xD}(\tau+1)+\eta_{x+})} \ ,
\end{aligned}
\tag{9.21}
$$

where $Q_x(I,\delta)$ is the betatron tune with its explicit dependence on all the oscillation amplitudes of eq. (9.20), $I_{x,y}$ and $|\delta_{x,y\pm}|$. The formal solutions from eq. (9.17) for the functions F_r and H up to first order are given by [17]

$$F_r = \frac{1}{1 - R_{x,y}R_\tau}(h - \overline{h}) \tag{9.22}$$

$$H = \overline{h} \tag{9.23}$$

where $\overline{h}$ represents the average of h over the phase angles, including the new variable τ. In order to obtain a detailed expansion of F_r the quantity $(h - \overline{h})$ should be expressed in terms of the eigen–vectors of $R_{x,y}R_\tau$. These eigen–vectors are the summands of the r.h.s. of eq. (9.16) for the initial basis or the summands of the r.h.s. of eq. (9.20) for the Normal Form basis. Nevertheless, in order to deal with simpler expressions this expansion is postponed to the end of the derivation.

9.5   The non–linear motion.

Following the same reasoning as in [6] the motion of the particle is computed expanding the exponential operator of eq. (9.19) up to first order, resulting in

$$\xi \approx \zeta + [F_r, \zeta] \tag{9.24}$$

where the square brackets denote the Poisson bracket. In order to compute this quantity the two following properties are used:

$$\left[\zeta_x^{+j}, \zeta_x^-\right] = -2ij\zeta_x^{+j-1} , \tag{9.25}$$

$$\left[\frac{1}{1 - R_{x,y}R_\tau}g(\zeta), \zeta_x^-\right] = \frac{1}{1 - e^{-i2\pi Q_x}R_{x,y}R_\tau}\left[g(\zeta), \zeta_x^-\right] , \tag{9.26}$$

where $g(\zeta)$ is an arbitrary function of the phase space coordinates ζ which is infinitely differentiable. Therefore the relation of the linearly normalized horizontal coordinate with the Normal Form horizontal coordinate is

$$\xi_x^- = \zeta_x^- - 2i\sum_{jklm} j\frac{h_{jklm}}{1 - e^{-i2\pi Q_x}R_{x,y}R_\tau}\zeta_x^{+(j-1)}\zeta_x^{-k}\zeta_y^{+l}\zeta_y^{-m} . \tag{9.27}$$

As stated above, the eigenvectors of the linear operator $R_{x,y}R_\tau$ are the summands of the r.h.s. of eq. (9.20) but not the ζ. To obtain the expansion as a power series of the eigenvectors the ζ have to be replaced by the expressions of eq. (9.20) and the products and powers of the trinomials have to be expanded. The turn–by–turn motion is obtained by successively applying the one–turn map to eq. (9.27) as done in eq. (9.21).

In the general case, the number of spectral lines arising from eqs. (9.27) and (9.20) in the horizontal motion is large and many Hamiltonian terms contribute to the same spectral line. For instance, the Hamiltonian term h_{jk00} introduces, in the horizontal spectrum, all the lines with the frequencies expressed as

$$(k_1 - j_1)Q_x + (k_2 - k_3 + j_2 - j_3)Q_{xD} , \tag{9.28}$$

k_i and j_i being arbitrary positive integers or zero fulfilling the following conditions:

$$k_1 + k_2 + k_3 = k ,$$
$$j_1 + j_2 + j_3 = j - 1 ,$$

where k and j are the indexes of the Hamiltonian term h_{jk00}. Each of the lines given by eq. (9.28) has associated the resonance condition expressed as

$$(k_1 - j_1 - 1)Q_x + (k_2 - k_3 + j_2 - j_3)Q_{xD} = p , \text{ with } p \in Z . \tag{9.29}$$

As an example using this expression it can be shown that the lowest multipoles driving the resonances $Q_{xD} = p$ and $2Q_{xD} = p$, with $p \in Z$, are the sextupole

and the octupole, respectively. In the appendix B the spectral lines introduced by the Hamiltonian terms h_{3000} and h_{1020} are derived.

Nevertheless, in the ideal case of an adiabatic excitation close enough to the resonance ($Q_D \approx Q_x$) the terms containing either $I_{x,y}$ or $\delta_{x,y+}$ are negligible. Thus eq. (9.27), for only one horizontal AC dipole, simplifies to

$$\xi_x^- \approx |\delta_{x-}|e^{i(2\pi Q_{xD}\tau - \eta_{x-})}$$
$$- \sum_{jklm} \frac{2ijh_{jk00}|\delta_{x-}|^{(j+k-1)}}{1 - e^{i2\pi(-Q_x+(k-j+1)Q_{xD})}}e^{i(k-j+1)(2\pi Q_{xD}\tau - \eta_{x-})} , \quad (9.30)$$

In this simplified case the Hamiltonian coefficient h_{jk00} only introduces the line with frequency $(k-j+1)Q_{xD}$ and the associated resonance condition is

$$-Q_x + (k - j + 1)Q_{xD} = p , \text{ with } p \in Z . \quad (9.31)$$

Although the betatron oscillation has been neglected the resonance conditions still involve Q_x. This is due to the factor $e^{-i2\pi Q_x}$ in the denominator of eq. (9.27).

9.6 A tracking example

In order to check the expressions derived above, single particle simulations have been done. A ring made of 108 FODO cells has been used, which indeed is a simple model of the SPS at CERN. Sextupoles are the only source of non–linearity. A horizontal AC dipole has been introduced with a linear ramping time of 5000 turns and a flat top of 1000 turns. From eq. (9.28) it is concluded that the Hamiltonian terms h_{3000}, h_{1200} and h_{2100} (coming from sextupoles) introduce all lines (m, n) with $|m| + |n| \leq 2$ except the line (–1,0), where (m, n) corresponds to the frequency $mQ_x + nQ_{xD}$. In fig. 9.1 the Fourier spectrum of the horizontal motion of the simulation is shown. In the figure all the predicted lines are seen plus the (0,3) and (0,–3) lines which come from the second order of the sextupolar terms.

The approximate expression in eq. (9.30) gives us the means of unambiguously measuring the Hamiltonian terms from the FFT of turn–by–turn data provided the approximation is good enough. The parameters of the simulation were chosen to optimize the study of the third order resonance. The strength of the sextupoles and the Twiss functions at their locations are shown in table 9.1. In fig. 9.2 the prediction of eq. (9.30) is compared to the analysis of the simulated tracking by plotting the normalized amplitude of the line (0,–2) versus the oscillation amplitude $|\delta_-|$ with $\beta_x = 100$ m. The comparison is done for two excitation frequencies. The limit of the normalized amplitude of the line (0,–2) as it approaches the resonance $Q_D = Q_x$ is also shown in the picture. In this limit the motion is equivalent to a free oscillation produced by a single kick. The normalized amplitude of the line (0,–2) with $Q_D = Q_x$ equals the normalized amplitude of the line with frequency $-2Q_x$ from the kicked particle motion.
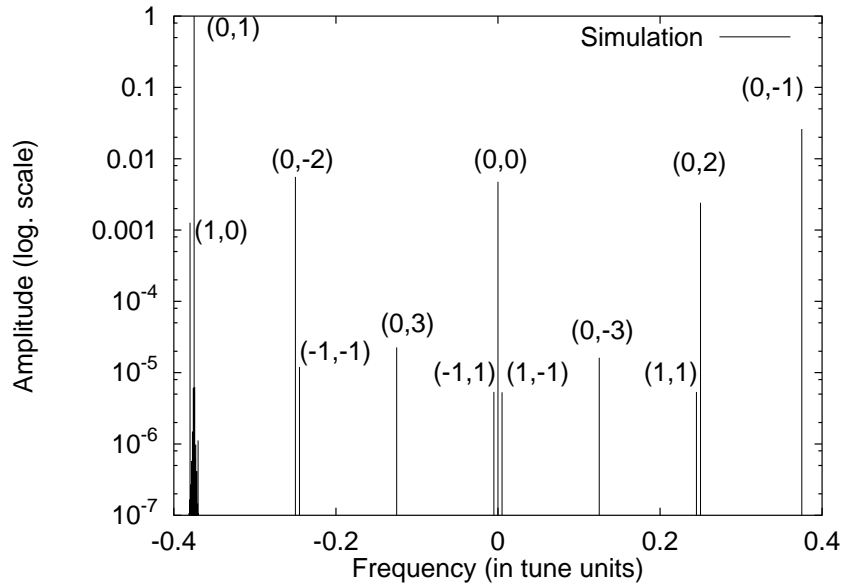
Figure 9.1: Normalized Fourier spectrum of the horizontal motion of a particle. The label (m,n) attached to each line indicates that the frequency of that line is $mQ_x + nQ_D$. For example the line (0,2) is mainly due to the term h_{1200}.

Element	Strength [m^{-2}]	β_x [m]	β_y [m]	ϕ_x	ϕ_y
sext.1	-0.1	42.41	55.96	6.21	6.26
sext.2	-0.2	19.63	107.64	6.53	6.53
sext.3	-0.2	19.65	106.69	6.78	6.78

Table 9.1: Strength of the sextupoles and twiss functions at their locations used in the simulation.
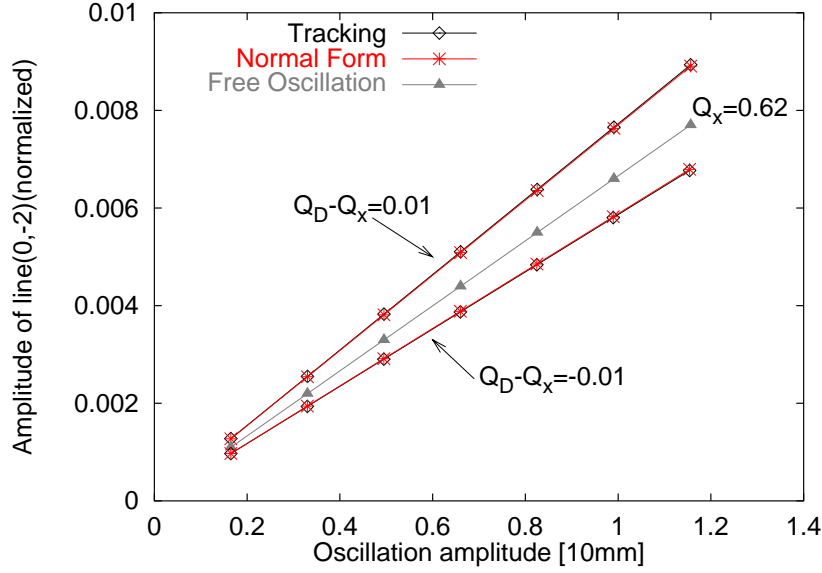
Figure 9.2: Comparison of the normalized amplitude of the line $-2Q_D$ from the horizontal motion of simulated tracking and the approximated model for the two different excitation frequencies $Q_D = Q_x \pm 0.01$. The normalized amplitude of the line $-2Q_x$ in the free oscillation case is also shown. These lines are due to the resonance term h_{3000}.

9.7   Considering an arbitrary initial location

As stated in section 9.3, the eigen–vectors of eq. (9.10) depend on the initial location, i.e. the longitudinal coordinate with zero phase advance. The turn–by–turn motion at an arbitrary location has been calculated in eq. (9.5), rewriting it using the one–turn linear operators yields

$$
\hat{x}(N) - i\hat{p}_x(N) = (R_x \otimes R_\tau)^N [\sqrt{2J} e^{i(\phi_x + \phi_{x0})} \\
+ e^{-i\phi_{xD}} (\delta_- e^{i2\pi Q_D \tau} - \delta_+ e^{-i2\pi Q_D \tau})] . \quad (9.32)
$$

The eigen–coordinates $(x_n, p_{xn}, y_n, p_{yn})$ at the nth element will be given by different expressions depending on whether it is located before or after the AC dipole. To compute them the expression inside the square brackets of eq. (9.32) is propagated to s_n as done in section 9.3, but now R_τ is only applied when $\phi_{xn} > \phi_{xD}$. This is given by the following expressions

$$
x_n - i p_{xn} = \begin{cases} \sqrt{\beta_{xn}} e^{i\phi_{xn}} [\sqrt{2J_x} e^{i(\phi_x + \phi_{x0})} + e^{-i\phi_{xD}} \\ \times (\delta_{x-} e^{i2\pi Q_{xD}\tau} - \delta_{x+} e^{-i2\pi Q_{xD}\tau})] & \text{if } \phi_{xn} < \phi_{xD} \\ \\ \sqrt{\beta_{xn}} e^{i\phi_{xn}} [\sqrt{2J_x} e^{i(\phi_x + \phi_{x0})} + e^{-i\phi_{xD}} \\ \times (\delta_{x-} e^{i2\pi (Q_{xD}\tau + Q_-)} - \delta_{x+} e^{-i2\pi (Q_{xD}\tau + Q_+)})] & \text{if } \phi_{xn} > \phi_{xD} \end{cases}
$$

$$(9.33)$$

Similar expressions hold for the vertical coordinate. Following the steps of section 9.3 the Hamiltonian h is expressed up to first order in $\tilde{h}_n$ as

$$h = \sum_{n=1}^{N_e} \tilde{h}_n(x_n, p_{xn}, y_n, p_{yn}) \ . \tag{9.34}$$

It was possible (see eq. (9.15)) to express the Hamiltonian with an AC dipole using the Hamiltonian terms h_{jklm} because all the elements fell into one of the two possible solutions of eq. (9.33). In the general case of an arbitrary initial location the contribution of each element to h depends on its relative position with respect to the AC dipole. To achieve a similar expansion to eq. (9.15), the Hamiltonian in absence of AC dipole is separated into two summations in the following way

$$h = \sum_{\phi_{xn} < \phi_{xD}} \tilde{h}_n + \sum_{\phi_{xn} > \phi_{xD}} \tilde{h}_n = \sum_{jklm} (h^<_{jklm} + h^>_{jklm}) z_x^{+j} z_x^{-k} z_y^{+l} z_y^{-m} \ , \tag{9.35}$$

where $h^<_{jklm}$ contains the contributions of all the elements before the AC dipole and $h^>_{jklm}$ of the elements after. These new terms can be used in expanding the Hamiltonian containing an AC dipole, leading to the expression

$$h = \sum_{jklm} h^<_{jklm} \xi_{<x}^{+j} \xi_{<x}^{-k} \xi_{<y}^{+l} \xi_{<y}^{-m} + \sum_{jklm} h^>_{jklm} \xi_{>x}^{+j} \xi_{>x}^{-k} \xi_{>y}^{+l} \xi_{>y}^{-m} \ , \tag{9.36}$$

with

$$
\begin{aligned}
\xi_{<x}^{\pm} &= \sqrt{2J_x} e^{\mp i(\phi_x + \phi_{x0})} \\
&\quad + |\delta_{x-}| e^{\mp i(2\pi Q_{xD}\tau + \eta'_{x-})} - |\delta_{x+}| e^{\pm i(2\pi Q_{xD}\tau + \eta'_{x+})} \ , \\
\xi_{>x}^{\pm} &= \sqrt{2J_x} e^{\mp i(\phi_x + \phi_{x0})} \\
&\quad + |\delta_{x-}| e^{\mp i[2\pi(Q_{xD}\tau + Q_-) + \eta'_{x-}]} - |\delta_{x+}| e^{\pm i[2\pi(Q_{xD}\tau + Q_+) + \eta'_{x+}]} \ ,
\end{aligned}
\tag{9.37}
$$

and $\eta'_{x\pm} = \mp(\eta_{x\pm} - \phi_{xD})$. Similar expressions hold for the vertical coordinates. The turn–by–turn motion can be computed in the same way as done in section 9.5 obtaining

$$
\begin{aligned}
\xi_x^- &= \zeta_x^- - 2i \sum_{jklm} j \frac{1}{1 - e^{-i2\pi Q_x} R_{x,y} R_\tau} \\
&\quad \times (h^<_{jklm} \zeta_{<x}^{+(j-1)} \zeta_{<x}^{-k} \zeta_{<y}^{+l} \zeta_{<y}^{-m} + h^>_{jklm} \zeta_{>x}^{+(j-1)} \zeta_{>x}^{-k} \zeta_{>y}^{+l} \zeta_{>y}^{-m}) \ , \tag{9.38}
\end{aligned}
$$

where the coordinates ζ are defined as the coordinates ξ in eq. (9.37) but replacing J_x by I_x and ϕ_x by ψ_x. Again the same approximation can be done as in section 9.5, resulting in the following expression for the horizontal motion in presence of one horizontal AC dipole

$$
\begin{aligned}
\xi_x^- &\approx |\delta_{x-}| e^{i(2\pi Q_{xD}\tau + \eta'_{x-})} \\
&\quad - 2i \sum_{jklm} j \frac{h'_{jk00} |\delta_{x-}|^{(j+k-1)}}{1 - e^{i2\pi(-Q_x + (k-j+1)Q_{xD})}} e^{i(k-j+1)(2\pi Q_{xD}\tau + \eta'_{x-})} \tag{9.39}
\end{aligned}
$$

with

$$h'_{jk00} = h^{<}_{jk00} + h^{>}_{jk00} e^{i(k-j+1)2\pi Q_-} \; . \tag{9.40}$$

This expression shows the difference between the Hamiltonian terms of a lattice with and without an AC dipole. For those locations where all the sources are seen to be either before ($h^{<}$) or after ($h^{>}$) the AC dipole the amplitudes of the two kinds of terms, h' and h, are equal. Notice that as Q_- decreases the terms with an AC dipole tend to the terms without an AC dipole. Also notice that the high order terms, with larger $|k - j + 1|$, will exhibit greater discrepancies between the two kinds of Hamiltonian terms. At the longitudinal location of a magnetic source the corresponding Hamiltonian terms vary abruptly in phase and amplitude [47]. The amplitude remains constant between sources. This property will allow the identification of locations with multipolar kicks in a real machine by using beam position data from the pick–ups along the ring.

A tracking simulation has been performed to check the approximation used in deriving eq. (9.39). The same lattice and method of the previous tracking example in section 9.6 have been used but 108 sextupoles were introduced. Turn–by–turn data are obtained at the different longitudinal locations. The Hamiltonian term h'_{3000} is obtained by evaluating the amplitude of the (0,–2) spectral line of these data (according to eq. (9.39)). The results of this analysis together with the theoretical value of h'_{3000} obtained from the lattice parameters are shown in fig. 9.3. Small discrepancies arise at some locations due to contributions from the terms h_{1200} and h_{2100} to the spectral line (0,–2). These contributions are proportional to the quantity δ_{x+} and they were neglected to arrive at eq. (9.39). To give an idea of the differences between the Hamiltonian terms with and without AC dipole their amplitudes are plotted versus the longitudinal coordinate for the same lattice in fig. 9.4.

9.8   Conclusion

A method to derive the Normal Form of a Hamiltonian with an AC dipole term is presented. To avoid the explicit time dependence of the Hamiltonian a new dimension is introduced. In principle this method works not only for the case of an AC dipole but for all cases where there is a solution of the linear plus the time dependent parts of the Hamiltonian.

The turn–by–turn motion at any location of the lattice is derived using Lie algebra techniques. In the general case various Hamiltonian terms contribute to the same Fourier spectral line of the motion. This is not the desired situation when using the AC dipole for non–linear beam diagnostic. Nevertheless an approximate expression for the turn–by–turn motion is derived under the ideal conditions that the excitation is adiabatic and the AC dipole tune is sufficiently close to the fundamental tune. It has been shown that the Hamiltonian terms in presence of the AC dipole are different to those without AC dipole. Nevertheless the discrepancies
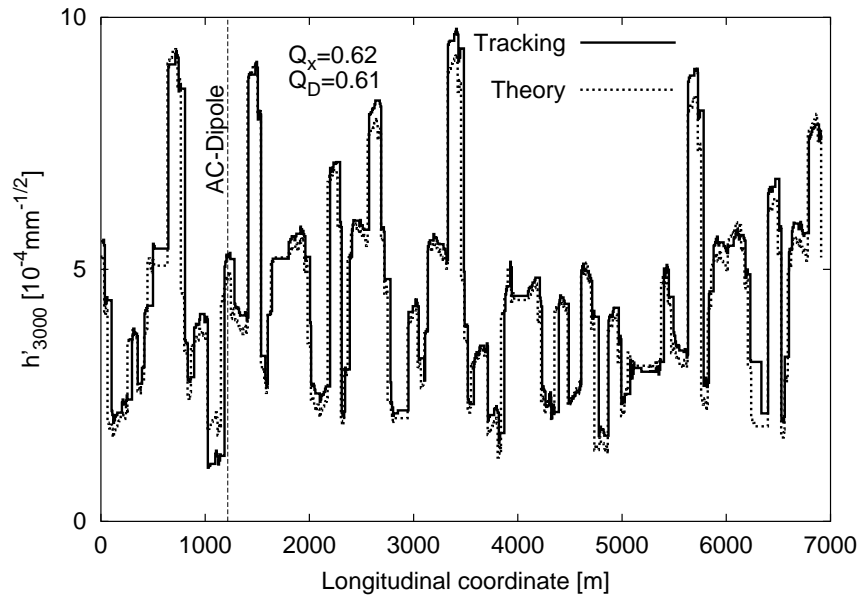
Figure 9.3: Comparison of the amplitude of the Hamiltonian term h'_{3000} computed from tracking and from theory (both with AC dipole) plotted versus the longitudinal position.
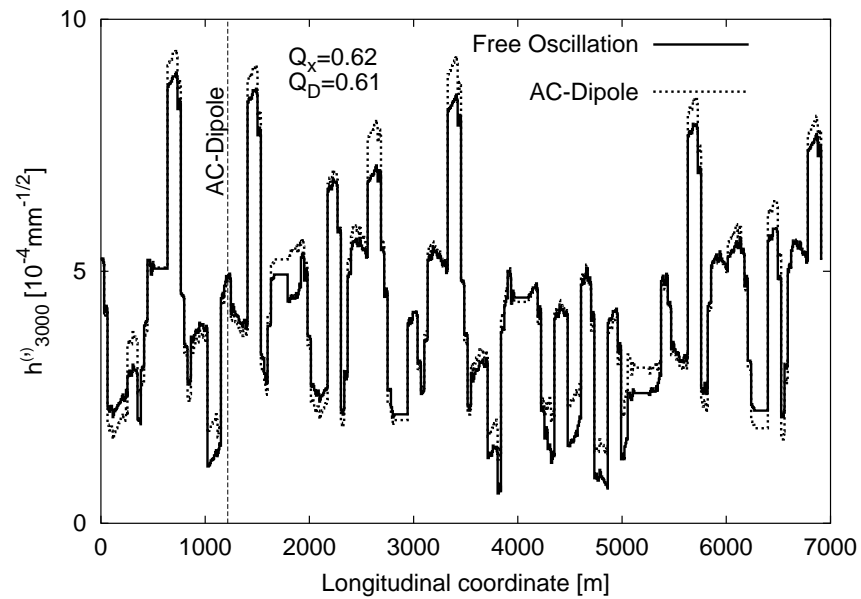
Figure 9.4: Comparison between the theoretical amplitudes of the Hamiltonian terms h'_{3000} (with AC dipole) and h_{3000} (free oscillation) plotted versus the longitudinal position.

should not be large and the local information contained in both cases is equivalent, i.e. it is possible to identify longitudinal locations with multipolar kicks. All this predictions have been compared with tracking simulations in a FODO lattice with sextupoles. In the more academic example where one resonance is strongly excited the agreement was excellent. In the more general case where 108 sextupoles were introduced some small discrepancies arose due to contributions from different resonance terms to the same spectral line. The feasibility of this technique in an operating machine has to be experimentally demonstrated. First experimental attempts to validate this method can be found in [58, 60].

Chapter 10

Comparison with other methods

Presently, various beam–based techniques to measure lattice imperfections or non–linearities are being investigated by other research groups. This chapter gives an overview of the different techniques under investigation. In table 10.1 a classification of these techniques is given based on the kind of perturbation applied to the beam. The different techniques fall into two groups: destructive and non–destructive. The non–destructive methods are suitable for feed–back systems whereas the destructive techniques should be used during the machine set–up only.

Perturbation		Measured quantity	Destructive	Ref.
Orbit bump	Static bump	Tunes	No	[10, 11]
	Wobbling bump	Fourier lines	No	[7]
Energy change	Radial steering	Tunes	Yes	[12]
	Energy kick	Fourier lines	Yes	[48]
	RF phase mod.	Fourier lines	Yes	[49]
Dipole kick	Used as corrector	Orbit	Yes	[13]
	Single kick	Fourier lines	Yes	[6]
		transfer map	Yes	[8]
		frequency map	Yes	[9]
	AC dipole	Fourier lines	No	[58, 59]

Table 10.1: Classification of the different techniques to measure lattice errors and/or non–linearities based on the type of perturbation applied to the beam and whether the method is destructive. The measured quantity and the bibliographic references are given in each case.

To assess the usefulness and the performance of a technique its various advantages and disadvantages have to be taken into account. For example, the methods that provide the local information are more advantageous than those that only give a global average. Other important parameters are the time that the complete measurement process lasts, the need for special instrumentation and the complexity of the measurement. In the following these techniques will be discussed according to the type of beam perturbation as indicated in table 10.1.

10.1 Orbit bumps

An orbit bump is a local modification of the reference orbit by use of dipole correctors. This kind of correctors are available for all accelerators since they are needed to keep the closed orbit close to the reference orbit. For a minimal bump set–up one needs two of these correctors but more sophisticated bumps with several correctors may be used. Orbit bumps are extensively used in a wide range of applications like alignment, K–modulation, impedance measurement, beam–beam effects, beam size measurements, luminosity optimization and, of course, non–linear diagnostics. Orbit bumps can be constant in time (static bump) or can vary harmonically with one or more frequencies (wobbling bump). These two scenarios render different beam dynamics and the information is obtained in a different way.

10.1.1 Static bump

This technique uses the fact that the non–linearity inside the orbit bump acts by feed–down to all lower orders. Its order and magnitude are deduced from the variation of suitable observables with the bump amplitude. The main observables are the tunes but also the degree of the bump non–closure (orbit leakages). An experimental application of this method can be found in [10] and [50]. In these studies a bump is created along a low–β triplet of quadrupoles and the tunes are measured as function of the amplitude of the bump. The multipolar components are found by a polynomial fit of the tunes versus the amplitude. The use of a Phase Lock Loop (PLL) for the tune measurement has advantages since it provides a resolution as low as 10^{-6}. Nevertheless, using a PLL makes this a delicate instrument at the present stage.

It was tried in simulation if this technique can be applied to the case of the LHC [11]. In this study a 7π bump is put along one arc of the LHC and the tunes are measured as function of the bump amplitude in view of optimizing the sextupolar spool pieces correction. The results are promising.

This technique finds the local information corresponding to just those multipoles that are located inside the bump. Therefore, to cover the whole machine, a very large number of bumps are needed which makes this procedure very time consuming. On the other hand it can be made non–destructive in case a PLL is used to measure the tunes.

10.1.2   Wobbling bump

If the bump is set to oscillate with one or more frequencies the non–linearities inside the bump will drive oscillations with frequencies as multiples of the wobbling frequencies. This technique was proposed in [7] and [51] and has been tried out at the COSY cooler synchrotron [52] and at the SPS [53]. Unfortunately, it was difficult to interpret the data in these first attempts. It therefore remains to be seen if this non–destructive technique can be of any use in machine operation.

10.2   Energy change

In this section those techniques are discussed that modify the beam or reference energy. They were initially proposed or used to measure the first order chromaticity but may be of more general use concerning non–linearities. There is also a new technique [54] which is based on the measurement of the oscillation phases of the head and the tail of the bunch after applying a transverse kick.

10.2.1   Radial steering

The radial steering procedure is based on changing the beam energy and the central orbit via frequency modulations of the radio frequency system. The tunes are measured for each of the different energy settings. Similarly to the case of an orbit bump the different multipolar fields induce different dependencies of the tunes versus the energy or, equivalently, the central orbit. Via a polynomial fit global multipolar components may be determined. In this case the bump is across the whole machine. For this reason this technique does not provide any local information, but it is much faster.

An example can be found in [12]. In this study it is assumed that the unknown sources of sextupolar and decapolar fields of the SPS are located at the dipoles and that the sources of octupolar fields are located at the quadrupoles. Another assumption is that all magnets of the same kind have the same multipolar components. The numerical values of the multipoles are chosen to match the machine measurements. The advantage of this technique is that it does not need dedicated instrumentation. Further applications of this technique are found in [55], which also makes use of the methods as described in this thesis.

10.2.2   Energy kick

This method has been recently proposed to measure the first order chromaticity by computing the synchrotron sidebands around the tunes after an energy kick and without the RF feedback. An experiment in the SPS [56] was carried out to test this technique. Unfortunately, it was not yet conclusive. A possible extension of this method is the measurement of resonant driving terms since the energy kick

and the subsequent synchrotron oscillations varies the orbit in the horizontal plane with the synchrotron frequency.

10.2.3 RF phase modulation

In [49] a method to measure chromaticity is proposed based on modulating the phase of the Radio Frequency (RF) cavities. Successful results from an experiment in the SPS are also reported. To determine the sign of the chromaticity a controlled tune modulation should be induced with quadrupoles. This method would largely profit from the use of a PLL.

10.3 Dipole kick

A dipole kick is provided by a dipole field, typically at one location of the ring. This kick is applied as a corrector when it is left constant over time. A single kick is applied only at one turn. On the other hand, an AC dipole provides a kick at every turn with an amplitude varying harmonically in time, mind you that it has to be switched on adiabatically. The aim of all these methods is to move the beam to different locations of the transverse phase space in order to extract the non–linear information.

10.3.1 Dipole kick as corrector

In [13] a technique is presented to measure the multipole components at each low–β triplet inside the IRs of RHIC. The technique is based on measurements of the strength of the overall kick that the orbit naturally experiences at a particular triplet due to the presence of linear and nonlinear errors. To measure the kick strength at the triplet, the action and phase are measured before and after the triplet. This action and phase can be related to the strength of the overall kick at the triplet. Action and phase measurements are done on an orbit obtained from the subtraction of an orbit produced by turning on a dipole corrector and the baseline orbit (difference orbit). This technique does not need any extra instrumentation and it provides the local information. Up to now it has been used in a destructive way but in principle one could do it in a non–destructive manner. Quadrupole components were successfully computed using experimental data but for the nonlinear measurements more experiments are needed to prove its usefulness.

10.3.2 Single kick

After applying a single kick the bunch performs betatron oscillations that are eventually damped due to decoherence processes. As a result the transverse emittance blows up, making this method intrinsically destructive but it gives plenty of high precision information concerning non–linearities with several ways to extract it.

The first way is the subject of this thesis. It has been presented here how by performing the Fourier spectrum of the turn–by–turn data the local information of the non–linearities can be extracted. It has been experimentally confirmed in the SPS and RHIC that quadrupolar and sextupolar resonances can be measured around the ring. The effect of decoherence on this method has been understood and can be incorporated into the measurement. No dedicated instrumentation is needed for this technique.

Another way of analyzing the data is by computing transfer maps [8]. A polynomial fit of the coordinates at a final location as a function of the initial coordinates is performed. The coefficients from the fit correspond to the integrated multipolar kicks between the two locations. The effect of beam decoherence cannot be easily taken into account. Therefore the measurement period has to be restricted to smaller time intervals before the decoherence becomes large. Also in this case there is no dedicated instrumentation needed. No experimental application of this technique has yet been performed.

The Frequency Map (FM) [9] is evaluated by applying several single kicks at different amplitudes. The tunes are computed as function of the horizontal and vertical oscillation amplitudes. The dynamics of the particle motion inside the storage ring can be analyzed by studying the regularity of this map. Therefore it does not provide any local information. This method has been successfully used in the ALS operation [57].

10.3.3 AC dipole

The greatest advantage of using an AC dipole to excite the beam motion is its non–destructiveness, keeping all the advantages of the dipole kick methods to measure non–linearities. A detailed description of the motion in presence of an AC dipole has been presented here in chapter 9 and in [59]. First experimental tests have been performed at the AGS of BNL [58] and more recently at the CERN SPS [60]. However, further experimental studies are required before this method can be applied for routine machine operation.

Chapter 11

Conclusions

In this thesis a beam based method has been studied to measure resonance driving terms using the FFT of BPM data taken from an accelerator in operation. Analytical derivations, computer simulations and experiments have been applied and performed for two different accelerators, i.e. the CERN SPS and RHIC at BNL.

The first new analytical aspect of this thesis consists of evaluating the effect of beam decoherence on the FFT spectra of BPM data. For a Gaussian beam it has been demonstrated that the normalized amplitude of the line $(m, 0)$ decreases by a factor of $|m|$ and its width increases by approximately the same factor if the beam experiences decoherence due to amplitude detuning. It has also been shown that in the context of spectral analysis the chromaticity introduces synchrotron sidebands around all spectral lines. These predictions have been tested against simulations of the centroid motion. The analytical expressions obtained for the shape of the lines have been compared to the lines obtained from the Fourier analysis of the simulation data and have been found in good agreement. There remain some small discrepancies of unknown origin in the tails of the distributions.

A second theoretical achievement is the discovery of a very useful property of the Hamiltonian terms. The amplitude of these terms remains constant along sections free of non–linear elements while their phase varies smoothly. Both amplitude and/or phase may change abruptly at the longitudinal location of non–linear elements. In a real machine this property has been proved to localize lattice errors by comparing the measurements of these terms at the BPMs with the predictions of the model at the same locations.

During three years a series of experiments have been performed to measure resonance driving terms in the SPS. The general and main conclusion is that global and local coupling and sextupolar resonance driving terms have been measured with good precision at the SPS. These measurements are in good agreement when compared to the predictions using the model of the SPS. A short list of the various results are given next. An observable for the coupling was defined based on the amplitude of the normalized secondary spectral lines. This observable is independent of the amplitude oscillations and pick–up calibrations and naturally leads to a fast

way to compensate the coupling resonance. Unexpected sextupole configurations were inferred from the measurements of local sextupolar resonance terms. In particular, it was found that the polarities of the extraction sextupoles were opposite to that of the lattice sextupoles and that in one experiment one of the sextupoles was accidentally disconnected. The validity of applying the decoherence factors has been demonstrated in several examples. Measuring the distribution of spectral lines of a single medium sized kick allowed to determine additional beam parameters like detuning with amplitude and beam emittance. To this end the predicted shape of the tune line in presence of decoherence was fitted to the experimental one. The phase of sextupolar terms has been measured around the ring which actually proves that one can measure both components of a resonance, i.e. amplitude and phase respectively. A two–dimensional sextupolar resonance which produces a non–linear coupling between the two transverse planes was measured as well. It was shown that this technique is not affected by the beam energy in the range between 26 and 120 GeV. Moreover, the results are not dependent on beam intensity in the range between 0.5×10^{10} and 6×10^{10} protons.

For the first time we were able to demonstrate that sextupole driving terms can be measured in RHIC, an operational superconducting machine. We measured two types of horizontal sextupole resonances at RHIC, obtaining good agreement with the RHIC model. More studies are planned at RHIC with an improved BPM system to allow the measurement of the local non–linear resonances.

Presently, this technique is destructive because the applied kick blows up the emittance of the beam. A major improvement can be achieved using AC dipoles which excite the beam adiabatically and close to the betatron frequency causing little emittance blow up. A method to derive the Normal Form of a Hamiltonian in presence of an AC dipole has been developed. The turn–by–turn motion at any location of the lattice is derived using Lie algebra techniques. It has been shown that the Hamiltonian terms including the AC dipole are different to those without an AC dipole. Nevertheless, the discrepancies should not be too large and the local information contained in both cases is equivalent, i.e. it is possible to identify the longitudinal locations of multipole kicks. These predictions have been compared with tracking simulations in a FODO lattice with sextupoles. In the somewhat academic example in which only one resonance is strongly excited the agreement is excellent. In the more general case of the SPS with 108 sextupoles some small discrepancies are observed. These are due to contributions from different resonance terms to the same spectral line.

In this thesis the feasibility of the proposed technique has been shown to detect and correct resonances of non–linear elements. It was also possible to localize these non–linear elements around the ring. Furthermore, one achieves a non–destructive tool when the kicker is replaced by an AC dipole. One can therefore be confident that this techniques has great potential to be very useful in commissioning and running of the CERN LHC which is planned to be started in 2008.

Acknowledgments

I want to express my gratitude to the accelerator physics group of CERN (SL/AP) for giving me the opportunity to make this work in the field of accelerator physics and for the financial support.

Bibliography

[1] R. Wolf "Field error definitions for LHC version 1", CERN AT–MA/AV 94–102, October 1994.

[2] J. Bengtsson, "Non–linear transverse dynamics for storage rings with applications to the Low–Energy Antiproton Ring (LEAR) at CERN", CERN 88–05 (1988).

[3] E. Asseo, J. Bengtsson and M. Chanel, "Absolute and high precision measurements of particle beam parameters at CERN antiproton storage ring LEAR using Spectral analysis with correction algorithms", 4th European Signal Processing Conference (1988), edited by J. L. Lacoume et al., North Holland, Amsterdam, pp. 1317–1320 (1988).

[4] J. Laskar, "Secular evolution of the solar system over 10 million years", Astron. Astrophys. **198**, pp. 341–362 (1988).

[5] J. Laskar, C. Froeschlé and A. Celletti, "The measure of chaos by the numerical analysis of the fundamental frequencies. Application to the standard mapping", Physica D **56**, pp. 253–269 (1992).

[6] R. Bartolini and F. Schmidt, "Normal Form via tracking or Beam Data", LHC Project note 132 (revised December 1999), Part. Accelerators. 59, pp. 93–106, (1998), http://wwwslap.cern.ch/frs/report/lines97.ps.Z.

[7] V. Ziemann, "Identification of Third Order Hamiltonian Coefficients from Forced Coherent Beam Oscillations", CERN SL/95–94 (AP) 1995.

[8] C. Wang and J. Irwin, "Possibility to measure the Poincaré section map of a circular accelerator", SLAC–PUB–7547, 1997.

[9] Y. Papaphilippou, "Frequency Maps of LHC Models", CERN–LHC–Project–Report–299, 1999.

[10] J.P. Koutchouk, F. Pilat and V. Ptitsyn, "Beam based measurement of field multipoles in the RHIC low beta insertions and extrapolation of the method to the LHC", CERN–SL–2001–051–BI, 2001.

[11] M. Hayes, "The Effect of Spool Piece Failure on Dynamic Aperture of the LHC During Injection", CERN–LHC–Project–Report–522, 2001.

[12] A. Faus–Golfe, F. Zimmermann, G. Arduini, P. Collier, "Modelling Nonlinear Optics in the CERN SPS", CERN–SL–2002–036–AP June 2002. Presented at the 8th European Particle Accelerator Conference, Paris, France, June 2002.

[13] J. Cardona, S. Peggs, T. Satogata, F. Pilat, V. Ptitsyn, "Determination of Linear and non Linear Components in RHIC Interaction Regions from Difference Orbit Measurements". Presented at the 8th European Particle Accelerator Conference, Paris, France, June 2002.

[14] Courant E.D. and Snyder H.S., "Theory of the Alternating Gradient Synchrotron", Ann. Phys. (USA) 3 (1958).

[15] "CERN Accelerator School. Fifth general accelerator physics course", CERN 94–01. Editor: S. Turner. September 1992.

[16] É. Forest, "Beam Dynamics: A New Attitude and Framework", Harwood Academic, pp.168–171 (1998).

[17] M. Berz, É. Forest and J. Irwin, "Normal form methods for complicated periodic systems: a complete solution using differential algebra and lie operators", Part. Acc. **24**, pp. 91–107 (1989).

[18] É. Forest, "A Hamiltonian free description of single particle dynamics for hopelessly complex periodic systems", Journ. of Math. Phys., 31, pp. 1133–1144 (1990).

[19] A. Bazzani, E. Todesco, G. Turchetti and G. Servizi, "A normal form approach to the theory of nonlinear betatronic motion", CERN 94–02, (1994).

[20] A. Bazzani et al., "Normal forms for Hamiltonian maps and nonlinear effects in a particle accelerator", Nuovo Cim., B **102**, pp. 51–80 (1988).

[21] R. E. Meller, A. W. Chao, J. M. Peterson, S. G. Peggs and M. Furman, "Decoherence of Kicked Beams", SSC–N–360, 1987.

[22] Editor: S. Turner, "CERN Accelerator School. Fifth general accelerator physics course" Finland 1994, CERN 94–01.

[23] F. Schmidt,"SIXTRACK: Single Particle Tracking Code Treating Transverse Motion with Synchrotron Oscillations in a Symplectic Manner", CERN SL/94–56 (AP).

[24] R. Bartolini and F. Schmidt, "SUSSIX: A Computer Code for frequency analysis of non–linear Betatron Motion", CERN SL–Note–98–017 (AP).

[25] G. Rumolo, F. Zimmermann, "Electron cloud simulations: beam instabilities and wake fields" ECloud'02 proceedings CERN–2002–001.

[26] "The 300 GeV Programme" CERN 1050, 14 January 1972, Geneva, Switzerland.

[27] Courtesy of W. Fisher

[28] C. Boccard et al. "Performance of the new SPS beam position orbit system (MOPOS)" CERN–SL–99–048–BI ; Geneva : CERN , 2 Sep 1999. Presented in: 4th European Workshop on Diagnostics and Instrumentation for Particle Accelerators, Chester, UK, 16 – 18 May 1999 – Daresbury Nucl. Phys. Lab., Warrington, 2000.

[29] C. Boccard, T. Bogey, J. Papis, L. Vos,"Orbit and trajectory measurement with low intensity lead ion beams in the SPS" CERN–SL–95–57 AP, Geneva 19 Jun 1995. Presented in the 2nd European Workshop on Beam Diagnostics and Instrumentation for Particle Accelerators: DIPAC '95, Lubeck–Travemunde, Germany, 28 – 31 May 1995 – DESY, Hamburg, 1995. [DESY–M–95–07 ; DOC–10582].

[30] J. Klem, G. Arduini, G. Morpurgo, "Multiturn Measurements at the CERN SPS" CERN–SL–2000–039–OP, Geneva, Jun 2000. Presented in: 7th European Particle Accelerator Conference, Vienna, Austria, 26 – 30 Jun 2000, European Phys. Soc., Geneva, 2000.

[31] Responsible for the SPS and LHC beam position monitors and tune measurement systems, private communication.

[32] C. Erles, private communication.

[33] F. Caspers, "SPS Kicker impedance, measurements and simulations" CERN–SL–2000–007–DI Geneva, 2000. Presented in 10th Workshop on LEP–SPS Performance, Chamonix, France, 17 – 21 Jan 2000, CERN, Geneva, Feb 2000.

[34] J. Dupin, "Electro–aimants dipoles, quadrupoles, sextupoles et octupoles pour les deux system d'extraction et le systeme de decharge et de rabotage de faisceau du SPS" CERN/SPS/ABT/80–18, Prévessin, December 1980.

[35] X. Altuna et al., "First Measurements of Resonance Driving Terms in the SPS", CERN SL–MD Note 045 (1998).

[36] X. Altuna et al., "Second Experiment to measure Resonance Driving Terms in the SPS" CERN SL–Note–99–017 MD.

[37] G. Morpurgo and J. Klem, "A Method to Measure the Beta–Beating in a 90 Degrees Phase Advance Lattice" CERN–SL–2000–040–OP, Jun 2000.

Pressented in: 7th European Particle Accelerator Conference, Vienna, Austria, 26 – 30 Jun 2000.

[38] G. Arduini, F. Calderini and N. Gonthier, private comunication (2002).

[39] A. Chao, remarks during the LHC Machine Advisory Committee (LHC–MAC 2002).

[40] M. Anerella et al., "The RHIC Magnet System", BNL MDN–610–20, to be published in NIM (2001).

[41] A. Jain, private communication (2002).

[42] W. Fischer, A. Jain, and S. Tepikian, "Beam–based Measurements of Persistent Current Decay in the Relativistic Heavy Ion Collider", Phys. Rev. ST Accel. Beams 4, 041002 (2001).

[43] I. Borchardt, E. Karantzoulis, H. Mais, G. Ripken "Calculation of beam envelopes in storage rings and transport systems in the presence of transverse space charge effects and coupling", DESY–87–161 (1987).

[44] S. Peggs and C. Tang, "Nonlinear diagnostics using an AC Dipole", RHIC/AP/159 (1998).

[45] H. Goldstein "Classical Mechanics" Addison–Wesley, page 368 (1980).

[46] J. Irwin "A multi–kick factorization algorithm for nonlinear maps", SSC–228 (1989).

[47] F. Schmidt, R. Tomás, A. Faus–Golfe, "Measurement of Driving Terms", presented at the 2001 Particle Accelerator Conference, and CERN SL 2001–039 (AP).

[48] G. Rumolo, F. Schmidt, R. Tomás, "Decoherence of a longitudinally kicked beam with chromaticity" CERN–SL–2002–049–AP, Geneva 17 Oct 2002.

[49] O. Brüning, W. Höfle, R. Jones, T. Linnecar, H. Schmickler, "Chromaticity Measurements via RF Phase Modulation and Continuous Tune Tracking" CERN–SL–2002–037–AP Geneva 25 Jun 2002.

[50] F. Pilat, P. Cameron, V. Ptitsyn, J–P. Koutchouk, "Linear and nonlinear corrections in the RHIC interaction regions". Presented at the 8th European Particle Accelerator Conference, Paris, France, June 2002.

[51] V. Ziemann, "Analysis of a method to measure the dodecapole component of the LHC triplet magnets with a wobbling closed bump" CERN–SL–2002–018–AP and CERN–TSL–Note–2002–54, Geneva 13 May 2002.

[52] P. Leunissen, Ph.D. thesis, T. Universiteit Eindhoven 1997.

[53] M. Hayes, J. Wenninger, V. Ziemann, private communication 2002.

[54] S. Fartoukh, R. Jones, "Determination of Chromaticity by the Measurement of Head–Tail Phase Shifts : Simulations, Results from the SPS and a Robustness Study for the LHC" CERN–LHC–Project–Report–602, Geneva 29 Jul 2002.

[55] G. Arduini, R. Tomás, F. Zimmermann, A. Faus–Golfe, N. Iida, "2002 Nonlinear Optics Measurements and Modelling for the SPS at 26 GeV", to be published.

[56] M. Hayes, F. Schmidt and R. Tomás, "Study of a novel method to measure chromaticity", to be published.

[57] C. Steier, D. Robin, J. Laskar, L. Nadolski, "Lattice Model Calibration and Frequency Map Measurements at the ALS" EPAC 2000, Vienna 2000.

[58] M. Bai, S. Y. Lee, J. W. Glenn, H. Huang, L. Ratner, T. Roser, M. J. Syphers, and W. van Asselt, "Experimental test of coherent betatron resonance excitations" Phys. Rev. E **56**, 6002–6007.

[59] R. Tomás, "Normal Form of Particle Motion under the Influence of an AC Dipole", Phys. Rev. ST Accel Beams, volume **5** 54001 (2002) and CERN–SL–2002–008 Geneva, 08 Apr 2002.

[60] N. Catalán, S. Fartoukh, M. Hayes, J–P. Koutchouk, F. Schmidt and R. Tomás, "Experiments with an AC dipole in the SPS", to be published.

Chapter 12

Resumen

12.1   Antecedentes y objetivos

EL futuro Large Hadron Collider (LHC) proporcionará colisiones protón–protón con una energía en el centro de masas de 14 TeV. La circunferencia de esta máquina será aproximadamente 27 km y el campo magnético en los dipolos superconductores será de 8.4 T. El LHC estará compuesto por 1232 dipolos y 386 cuadrupolos así como 20 tipos diferentes de imanes destinados a la inyección y a la corrección. En un imán convencional el campo viene determinado por la forma de los polos ferromagnéticos mientras que en un imán superconductor el campo está definido principalmente por la distribución espacial del cable superconductor en las bobinas. En los imanes convencionales se alcanza una precisión de 0.01 mm en el pulido de los polos mientras que el posicionamiento de los cables superconductores tiene una precisión máxima de 0.1 mm. Debido a esta diferencia los imanes superconductores son intrínsecamente menos precisos que los convencionales. Normalmente las desviaciones del campo real en el imán comparado con el campo ideal se expresan mediante una superposición de multipolos de orden ascendente. Por multipolo de orden n entendemos un imán de n polos en el que el campo aumenta con la potencia $(n-1)$ de las coordenadas transversales. Cada uno de estos multipolos contribuye a la dinámica de las partículas confinadas en el anillo de una forma precisa descrita mediante un conjunto de términos en el Hamiltoniano. Tan sólo la parte lineal del Hamiltoniano, definida por los dipolos y los cuadrupolos, presenta una solución exacta para la trayectoria de las partículas. Básicamente la dinámica lineal es equivalente a la del oscilador harmónico. Los multipolos de orden superior, como el sextupolo o el octupolo, definen la dinámica no lineal. Las soluciones a la dinámica no lineal sólo pueden ser halladas mediante métodos perturbativos en la vecindad de un punto fijo. De hecho, a partir de cierta amplitud de oscilación el movimiento se vuelve caótico e inestable. La región del espacio fásico donde las trayectorias serán estables se denomina apertura dinámica. Por lo tanto la apertura dinámica de la máquina queda determinada por el contenido no lineal. El LHC estará equipado con distintos imanes correctores no lineales destinados a cancelar los

errores de la máquina y maximizar así la apertura dinámica. Por ésto, las técnicas que permitan la medida de estos errores no lineales serán de gran valor a la hora de detectar fallos y optimizar el rendimiento de la máquina.

El objetivo de esta tesis es desarrollar un método para medir los términos resonantes del Hamiltoniano de un acelerador basado en la transformada de Fourier de los datos recogidos por los monitores de posición del haz (BPMs). El primer intento de realizar medidas de este tipo se llevó a cabo en 1988 [2]. Mediante teoría de perturbaciones se estudió la relación de las lineas del espectro de la trayectoria vuelta a vuelta en función de los términos del Hamiltoniano. Un importante prerequisito para este análisis era el desarrollo de una técnica superior para la medición de las frecuencias fundamentales (tonos) de la señal vuelta a vuelta del haz, tanto si la señal proviene de una simulación como de los monitores de posición del haz de un acelerador. Recientemente se han desarrollado técnicas que permiten determinar el espectro de Fourier con una mayor precisión [5]. Estas técnicas ya se han aplicado con éxito en datos provenientes de simulaciones para corregir no linealidades creadas por sextupolos. En la parte teórica de este trabajo se estudia como varían los términos del Hamiltoniano a lo largo del anillo y se desarrollan modelos teóricos que describan con más exactitud el espectro de Fourier de la trayectoria del haz teniendo en cuenta la distribución de partículas en el haz. Estas predicciones analíticas se compararán con simulaciones numéricas.

La parte experimental de esta tesis tiene por objetivo demostrar la viabilidad y la utilidad de esta técnica en un acelerador en funcionamiento. Para realizar los experimentos se ha escogido principalmente el Super Proton Synchrotron (SPS) del CERN por su accesibilidad y adecuada instrumentación. Este acelerador es altamente lineal pero dispone de ocho potentes sextupolos con los que introducir la no linealidad de forma controlada. Estos sextupolos se denominan sextupolos de extracción. También se han realizado experimentos similares en el Relativistic Heavy Ion Collider (RHIC) del Brookhaven National Laboratory (BNL). Este colisionador, al igual que lo será el LHC, está compuesto por imanes superconductores. Por lo tanto es un banco de pruebas ideal para testear esta técnica.

Por último se ha estudiado analíticamente una mejora de este método. Esta mejora consistiría en introducir una oscilacion del haz con una frecuencia ligeramente diferente al tono. Para esto se usa un dipolo alimentado con corriente alterna, llamado "dipolo AC". Gracias a este instrumento esta técnica se podría aplicar sin que la medida sea destructiva, como era el caso anterior.

12.2   Discusión de los resultados

La dinámica de una partícula en un acelerador se describe mediante una órbita de referencia. Esta órbita es la que seguiría una partícula con momento de referencia p_0. Un acelerador está compuesto por diversos elementos magnéticos: los dipolos que determinan la órbita de referencia; los cuadrupolos que se encargan de la focalización del haz y además existen diversos multipolos utilizados para

corregir las distintas aberraciones de la máquina como los sextupolos y los octupo-
los. La dinámica lineal queda determinada por los dipolos y los cuadrupolos y es
básicamente equivalente a la del oscilador harmónico. Las frecuencias fundamen-
tales del movimiento en cada uno de los ejes de referencia se denominan tonos. Al
considerar elementos no lineales, i.e. orden multipolar superior al cuadrupolar, la
trayectoria deja de ser integrable y es necesario considerar los campos no lineales
como perturbaciones del Hamiltoniano. Una de las técnicas más apropiadas para
el tratamiento analítico de las no linealidades es la denominada "Forma Normal"
([17], [18] o [19]), que se basa en la representación de los distintos elementos
magnéticos mediante operadores exponenciales sobre un álgebra de Lie. La idea
fundamental de la "Forma Normal" es que en la vecindad de los puntos fijos y
estables debe existir un cambio de coordenadas que transforme las ecuaciones de
movimiento en las de un oscilador harmónico cuya frecuencia dependa de la ampli-
tud de oscilación. Concretamente se llega a expresar la trayectoria de la partícula
como una superposición de oscilaciones harmónicas [6]. La oscilación en cada uno
de los ejes tiene por frecuencia fundamental el tono correspondiente y su ampli-
tud es la excursión inicial del haz en ese eje. Además aparecen acopladas un gran
número de oscilaciones de menor amplitud. Cada una de estas oscilaciones está
ligada a un término del Hamiltoniano, representado por h_{mnlk}. La frecuencia y la
amplitud de la oscilación quedan determinadas por el término en cuestión. Estas
oscilaciones aparecen en el análisis de Fourier de la posición de la partícula como
lineas espectrales y su medida permite la determinación de los distintos términos
del Hamiltoniano. En una máquina real se obtiene la posición del haz vuelta tras
vuelta mediante monitores de posición del haz distribuidos a lo largo de ésta. El
análisis de Fourier de esta señal contiene la información de las no linealidades de
la máquina.

El estudio detallado de los términos del Hamiltoniano en esta tesis doctoral ha
abierto la posibilidad de una nueva utilidad para este método de medida: la lo-
calización de las no linealidades. Se ha demostrado que estos términos varían en
función de la posición a lo largo de la máquina y concretamente éstos experimen-
tan un cambio brusco allá donde se localizan las fuentes de no linealidad. Esto sig-
nifica que el sistema de monitores de posición del haz a lo largo de la máquina nos
permitirá determinar los distintos términos del Hamiltoniano en cada BPM y así
localizar los campos no lineales e identificar las imperfecciones por comparación
con el modelo.

Otra aportación importante de esta tesis al método de medida es la descripción
analítica del efecto de los distintos procesos de decoherencia en el espectro de
Fourier de la trayectoria del haz vuelta tras vuelta. Los procesos de decoherencia
se observan cuando las frecuencias fundamentales de las partículas que componen
el haz son función de alguna de las variables del espacio fásico. Las fuentes mas
importantes de decoherencia son:

- **El corrimiento del tono con la amplitud**. En este caso los tonos son fun-
  ciones de las amplitudes de oscilación. Esta dependencia se debe exclu-

sivamente a las no linealidades. Tanto los sextupolos como los octupolos provocan una dependencia cuadrática de los tonos en las amplitudes de oscilación. Las contribuciones de multipolos superiores no se han considerado en el modelo analítico.

- **La cromaticidad**. En este caso los tonos dependen de la energía de la partícula. Aquellas partículas con una energía superior a la de referencia sufren una menor desviación en los elementos magnéticos y viceversa para aquellas partículas con una energía inferior a la de referencia. La cromaticidad se define, así, como la derivada del tono respecto del momento relativo de la partícula. Hay que tener en cuenta que la energía de la partícula sigue una oscilación harmónica de frecuencia Q_s, el tono sincrotrón. Por lo tanto los tonos también siguen una modulación en esta frecuencia con una amplitud proporcional a la cromaticidad. Esta aberración se puede corregir mediante familias de sextupolos convenientemente distribuidas a lo largo del anillo.

El haz está constituido por un gran número de partículas que normalmente obedecen una distribución gausiana en los tres planos del espacio fásico. Con el fin de estudiar el espectro de la oscilación en presencia de decoherencia se ha asumido que cada partícula del haz sigue la trayectoria predicha por la "Forma Normal", que los tonos de cada partícula son funciones lineales de la energía y del cuadrado de la amplitud de oscilación y se ha calculado la trayectoria del centroide promediando sobre un haz gausiano. En el caso más general considerado, con las tres dimensiones, se ha conseguido expresar la transformada de Fourier como una sola integral sobre una de las amplitudes del espacio fásico. Considerando sólo el plano horizontal y el longitudinal se ha llegado a una expresión analítica para el espectro de Fourier de la señal. Las diferencias más importantes en comparación con el espectro de una sola partícula debidas al **corrimiento del tono con la amplitud** son: (1) las lineas espectrales ya no son distribuciones de Dirac sino funciones con cierta anchura. Dicha anchura es aproximadamente proporcional al número harmónico de la línea, i.e. la linea de frecuencia $2Q_x$ es 2 veces mas ancha que la fundamental Q_x; (2) la amplitud de la línea espectral con frecuencia $mQ_{x,y}$ se ve reducida por un factor $|m|$ debido a la decoherencia. Este hecho introduce una dificultad añadida a la medida ya que reduce la señal de interés. Las diferencias más importantes entre el espectro del centroide y el de una sola partícula debidas a la **cromaticidad** son: (1) la aparición de bandas laterales en todas las lineas del espectro. Si la frecuencia de la línea es ν las bandas laterales aparecen con frecuencias $(\nu \pm qQ_s)$, donde q es un entero positivo o cero y Q_s es el tono sincrotrón. La amplitud de estas bandas decrece rápidamente a medida que q aumenta; (2) las amplitudes de las diferentes líneas del espectro se ven afectadas por diferentes factores debidos a la cromaticidad. Idealmente se medirá con cromaticidad nula.

Con el fin de testear todas estas predicciones se han realizado distintas simulaciones de la dinámica del centroide. Para ello se ha usado un modelo del SPS del CERN, que básicamente es un anillo de 1100 m de radio cuya estructura es

de tipo FODO [22]. Se han realizado dos tipos de simulaciones, uno para comprobar el efecto del corrimiento del tono con la amplitud y otro para comprobar el efecto de la cromaticidad. En el primer tipo se simula un gran número de partículas con distribución gausiana sólo en el plano horizontal y se utilizan sextupolos como fuentes no lineales. En el segundo caso se consideran distribuciones gausianas en los tres planos del espacio físico pero sin fuentes no lineales. Las expresiones analíticas obtenidas han sido comparadas con distintas simulaciones obteniendo un buen acuerdo.

La parte experimental de esta tesis se desarrolla en dos aceleradores, el SPS y el RHIC. En el SPS se han realizado experimentos sistemáticamente durante los tres años entre el 2000 y el 2002. Con el fin de dar la mayor validez posible a esta técnica de medida los experimentos cubrieron una amplia gama de escenarios: diferentes energías de los protones, diferentes intensidades del haz, diversos tonos horizontal y vertical, diferentes configuraciones de los sextupolos de extracción, etc. En el RHIC se llevó a cabo tan sólo un experimento con el fin de probar esta técnica en una máquina con imanes superconductores, más similar al futuro LHC. En lo que sigue se discuten estos experimentos en orden cronológico.

Descripción del SPS

El SPS forma parte del gran complejo de aceleradores de partículas del CERN. Su misión consistirá en el suministro de protones al LHC. El SPS recibirá el haz de protones del Proton Synchrontron (PS) a una energía de 26 GeV y lo acelerará hasta 450 GeV para inyectarlo en el LHC, el qué, a su vez, lo acelerará hasta 7 TeV.

El SPS es un sincrotrón de protones de un radio promedio de 1100 m. Su estructura consiste de 108 celdas tipo FODO. Una celda FODO esta compuesta por un cuadrupolo focalizante y otro desfocalizante separados por espacios vacíos. La fase de la oscilación betatrónica avanza casi $\pi/2$ por celda por lo que el tono, que es el avance de fase a lo largo de una vuelta, es aproximadamente 27. Los tonos del SPS tienen una gran flexibilidad habiéndose usado durante nuestros experimentos valores comprendidos entre 26.1 y 26.8. Una descripción más detallada del SPS se puede hallar en [26].

El SPS cuenta con una gran colección de instrumentos usados para controlar el haz y medir sus parámetros. En los apartados siguientes se describen brevemente aquellos instrumentos usados en los experimentos para la medida de términos resonantes:

- **Monitores de posición del haz**: Estos monitores proporcionan una medida de la posición del centroide del haz. La mayoría de los monitores de posición del SPS son de tipo electrostático y básicamente consisten de dos placas conductoras a ambos lados de la cámara de vacío. Cuando el haz pasa entre las placas la posición del centroide se puede inferir de las cargas eléctricas inducidas en cada placa. Existen alrededor de 110 monitores por

cada plano transverso y se encuentran distribuidos uniformemente alrededor de la máquina. El avance de fase de la oscilación betatrónica entre monitores consecutivos es de casi $\pi/2$. La mayoría de los monitores se encuentran posicionados allá donde la función betatrónica correspondiente es máxima, i.e. un monitor horizontal tiene típicamente una función betatrónica horizontal de 103 m mientras que la función betatrónica vertical es de 20 m y viceversa para los monitores de posición verticales.

- **Q-Kickers**: Por "kicker" entendemos un imán capaz de producir un campo magnético transverso al paso del haz. Normalmente son usados para excitar oscilaciones horizontales y verticales en el haz mediante la producción del campo magnético apropiado durante una vuelta. El SPS está equipado con un "Q-kicker" horizontal y otro vertical. Se denominan así debido a que normalmente se usan para llevar a cabo la medición de los tonos (Q_x, Q_y). Durante los experimentos de esta tesis en los que la energía es inferior o igual a 80 GeV, los "Q-Kickers" se han usado para excitar oscilaciones betatrónicas en cada uno de los planos.

- **Kicker de extracción**: Es un "kicker" que actúa en el plano horizontal y es más potente que los "Q-kickers". Normalmente se usa para la extracción del haz. Durante los experimentos de esta tesis con una energía de 120 GeV este instrumento se ha usado para excitar oscilaciones betatrónicas horizontales.

- **Sextupolos de extracción**: Durante la operación normal de la máquina estos potentes sextupolos se usan para la extracción lenta o resonante del haz. El SPS está equipado con ocho de estos sextupolos. Una descripción técnica de éstos puede encontrarse en [34]. En los experimentos llevados a cabo para esta tesis estos sextupolos se han usado para crear una no linealidad controlada y conocida.

- **Cuadrupolos "skew"**: Un cuadrupolo "skew" o girado es un cuadrupolo girado 45° respecto al normal. El SPS está equipado con 6 cuadrupolos de este tipo. Su misión es cancelar los errores de acoplamiento transverso de la máquina. En nuestros experimentos además de darles esta utilidad también se usaron para crear una cantidad controlada de acoplamiento lineal.

Los experimentos del 2000 en el SPS

Durante el año 2000 se realizaron experimentos a dos energías diferentes: 26 GeV y 120 GeV. La energía de 26 GeV es de gran relevancia ya que será la energía de inyección en el SPS cuando el LHC entre en funcionamiento. Históricamente este tipo de estudios se realizaba a 120 GeV. La energía de 120 GeV es de carácter excepcional con el fin de discernir el efecto de los remanentes de campo que aparecen a más bajas energías y que a ésta no deben estar presentes. Los experimentos a la energía de 26 GeV estuvieron focalizados fundamentalmente en la medida del acoplamiento lineal que se manifiesta en el término resonante h_{1001}. Este término

resonante produce una linea espectral con la frecuencia del tono vertical en el espectro horizontal. Para la realización de la medida a cada haz inyectado se le aplica un "kick" (campo magnético dipolar durante una sola vuelta) en los dos planos transversos con el fin de producir oscilaciones betatrónicas. La posición del haz se mide vuelta tras vuelta usando los monitores de posición del haz y a continuación se calcula la transformada de Fourier de las señales. Por motivos de carácter técnico en el experimento a 26 GeV sólo se pudo utilizar la señal procedente de un monitor de posición horizontal. A su vez, la lectura de la amplitud de la linea espectral de interés tuvo que hacerse en la pantalla de uno de los ordenadores de la sala de control, por lo cual la medida fue poco precisa. Para contrarrestar esta imprecisión se repitió la medida un gran número de veces. Se determinó de esta manera la amplitud de la linea espectral de acoplamiento en función de la corriente aplicada en los cuadrupolos girados. Ésto permitió encontrar el mínimo acoplamiento, que coincide con el mínimo de amplitud de la linea espectral de acoplamiento. Sin embargo no se entendió entonces porque la pendiente de la curva del acoplamiento en función de los amperios a ambos lados del mínimo era diferente. Veremos más adelante como en años siguientes se mejora el método de medida y se aclara este punto.

En el mismo año se realizó otro experimento con una energía de 120 GeV. Se conectaron los sextupolos de extracción con el fin de generar una gran no linealidad y poder medir términos resonantes de orden sextupolar. Se aplicaron "kicks" con diferentes amplitudes y se almacenaron las medidas de la posición del haz vuelta tras vuelta provenientes de todos los monitores. Una de las lineas espectrales producida por los campos sextupolares tiene por frecuencia el doble del tono horizontal con el signo opuesto. Esta linea se pudo medir para todos los monitores disponibles. Su promedio obtuvo un perfecto acuerdo con la predicción del modelo pero comparando en las distintas posiciones de los monitores se observó una clara discrepancia. Esta discrepancia se resolvía si la polaridad de los sextupolos de extracción se consideraba opuesta a la del modelo inicial. Esto llevó a realizar medidas de la polaridad de estos sextupolos obteniendo que, de acuerdo con nuestra hipótesis, su polaridad era opuesta a la del modelo. Estos datos sirvieron también para comprobar algunas de las predicciones analíticas de la reducción y el ensanchamiento de las lineas espectrales debido a la existencia del corrimiento del tono con la amplitud. Esta propiedad se usó para determinar parámetros del haz tras hacer un ajuste de la fórmula teórica a los datos experimentales. Los parámetros del haz que se pudieron determinar mediante este ajuste son: el tono cuando la amplitud de oscilación tiende a cero, el corrimiento del tono con la amplitud y el "kick" aplicado. Los resultados de la medida de estos parámetros por el método expuesto se compararon con resultados de otros métodos obteniendo un buen acuerdo.

Los experimentos del 2001 en el SPS

Con el fin de mejorar y agilizar las medidas durante los experimentos, especialmente la del acoplamiento, fue necesario desarrollar una aplicación informática que recogiera las medidas de los monitores de posición del haz, calculara la trans-

formada de Fourier y mostrara los resultados en gráficas. Esta tarea se llevó a cabo en la fase de preparación de los experimentos que se realizarían en el 2001. Tanto para la interfaz gráfica como para la representación de gráficas se usaron códigos y librerías estándar mientras que para el cálculo de la transformada de Fourier se usó una modificación del código fuente de SUSSIX [24].

En el año 2001 se dispone de más tiempo experimental y se dedica exclusivamente a la energía de 26 GeV. Todos los datos adquiridos durante este año se ven afectados por un problema del sistema de los monitores de posición. Un porcentaje de estos monitores proporcionaba medidas erróneas de la posición del haz. Tras un estudio detallado se comprobó que los monitores afectados cambiaban de experimento a experimento por lo que no era un problema intrínseco de los monitores. Este hecho llevó a los expertos de instrumentación a realizar un estudio y como conclusión se vio que se trataba de un problema del ajuste de la sincronización entre el sistema de adquisición de datos y el haz [31]. Así pues este problema desaparecería para los experimentos del 2002 pero en los datos adquiridos durante el 2001 se tendrian que encontrar aquellas señales erróneas y descartarlas para el análisis. Para ello se desarrolló un método para identificar aquellas señales no físicas basado en el análisis del espectro de Fourier. Básicamente se escoge una ventana del espectro en la que sabemos (ya que conocemos los tonos) que no deben existir lineas espectrales y se calcula la desviación estándar de las amplitudes de las lineas comprendidas en ese espectro. Aquellas señales no físicas presentarán una mayor desviación estándar que la de las señales físicas. Por supuesto hubo que elegir un limite para dicho valor para decidir si una desviación estándar provenía de una señal física o no. Una vez identificadas las señales no físicas se descartan para cualquier análisis.

La medida del acoplamiento lineal transverso se mejoró gracias: al uso de la aplicación informática "on-line" diseñada al efecto, a que se pudieron almacenar los datos de los monitores de posición del haz (y filtrar posteriormente aquellas señales no físicas) y a que se encontró un observable más adecuado que el usado el año anterior. Este observable se obtiene de las dos lineas espectrales producidas en cada plano transverso debidas al acoplamiento, i.e. la linea con el tono vertical en el plano horizontal y la linea con el tono horizontal en el plano vertical. Este observable proporciona directamente el término resonante y no depende de amplitudes de oscilación ni de la calibración del monitor de posición (debido a la normalización del espectro). Así se resolvió también el problema de la diferencia de las pendientes a ambos lados del mínimo. Esta diferencia se originaba a que la amplitud de oscilación depende no sólo del "kick" aplicado sino también del acoplamiento de la máquina. Por ello introducir un observable independiente de la amplitud de oscilación resolvió esta cuestión.

Al mismo tiempo se llevaron a cabo medidas de términos sextupolares para la "máquina base" (sin no linealidades) y para la máquina con sextupolos de extracción, con diversas configuraciones y tonos. El proceso experimental consistía en aplicar "kicks" con diferentes amplitudes y almacenar los datos. De la teoría se

desprende que las amplitudes normalizadas de las lineas espectrales (-2,0) y (2,0) son proporcionales al kick y a los términos sextupolares h_{3000} y h_{1200} respectivamente. Por lo que tras hacer un ajuste lineal de la amplitud de estas lineas frente a las amplitudes del kick se pueden inferir los términos sextupolares. Procesos similares se llevarían a cabo para medir otro tipo de resonancias. Las medidas realizadas con la "máquina base" mostraron que era posible medir los términos sextupolares en ausencia de potentes fuentes de no linealidad. El acuerdo entre la predicción del modelo y el experimento es satisfactorio: el valor medio a lo largo del SPS coincide pero existen discrepancias locales debido a los otros tipos de errores lineales y no lineales de la máquina no considerados en el modelo.

Con los sextupolos de extracción conectados las discrepancias entre predicción y medida deben ser pequeñas puesto que conocemos las principales fuentes sextupolares. Comparando estas medidas, realizadas del mismo modo que las anteriores, con el modelo obtuvimos inicialmente una severa discrepancia de la que se deducia la necesidad de mejorar el modelo. Tras varios refinamientos del modelo, casi sin influencia, se observó que la órbita de referencia durante los experimentos no había sido suficientemente pequeña como para despreciarla. La buscada mejora del modelo debe pues consistir en introducir la órbita cerrada medida durante el experimento. Ésta se calculó promediando la posición del haz medida durante las vueltas previas al "kick". Para introducir la órbita cerrada en el modelo se asignó a cada sextupolo un desplazamiento opuesto a la órbita medida. Se comprobó a continuación que la órbita cerrada del modelo no difería en mas de un diez por cien de la medida. Gracias a esto se obtuvo un buen acuerdo entre los términos sextupolares provenientes del experimento y del modelo considerando la órbita cerrada.

Es de particular interés la medida de estos términos cuando el tono se encuentra próximo a la resonancia correspondiente ya que, de los desarrollos teóricos de esta tesis se desprende que en este caso la variación relativa a lo largo del anillo del término resonante se reduce, eliminando en parte la información local. Se realizaron medidas con el tono horizontal próximo al tercio de entero con una configuración de los sextupolos de extracción en la que todos tenían la misma polaridad y estaban alimentados con 8 amperios. Se obtuvo un excelente acuerdo entre modelo y experimento, confirmando así las predicciones teóricas.

Los experimentos del 2002 en el SPS

El objetivo de los experimentos del año 2002 en el SPS es tratar de aclarar distintas cuestiones pendientes: posibles influencias de la energía de las partículas y la intensidad del haz, medida de resonancias de orden superior y bidimensionales y, por último, la determinación de la fase de los términos resonantes.

Para examinar una posible influencia de la energía se preparó un ciclo especial del SPS en el que se disponía de un "plateau" inicial a 26 GeV y a continuación se aceleraba hasta 80 GeV. Se realizaron medidas de términos sextupolares a ambas energías para la "máquina base" sin hallarse diferencias relevantes.

Para estudiar la posible influencia de la intensidad se realizaron medidas con haces de diferentes intensidades durante un mismo experimento, entre 0.5×10^{10} y

6×10^{10} protones. Ésto se conseguía inyectando la intensidad más alta, de 6×10^{10} protones, desde el Proton Synchrotron (PS) y a continuación limitando la cantidad de haz en el SPS con una apertura física impuesta por los "scrapers". Permitiendo con estos instrumentos una reducción de intensidad hasta 0.5×10^{10} protones. En este rango de intensidades se observó una pequeña fluctuación de la variación del tono con la amplitud de oscilación pero los términos resonantes medidos no presentaron ninguna dependencia con la intensidad.

Durante el 2002 fue posible realizar medidas de la fase de los términos resonantes de origen sextupolar. Ésto fue debido en parte al buen funcionamiento de los monitores de posición de haz. También, la introducción de un observable apropiado para estas fases (como es la diferencia con la fase de la oscilación fundamental) facilita la confrontación con el modelo y sobre todo muestra un comportamiento similar al de la amplitud, i.e. permanece constante en aquellas regiones libres de fuentes de no linealidad y cambia abruptamente allí donde éstas se localizan. Este comportamiento es de gran importancia para el proceso de localización de una fuente no lineal, ya que, disponiendo de la amplitud y la fase, el cambio abrupto ha de reflejarse en, al menos, una de estas cantidades. El acuerdo entre medidas y predicciones del observable relacionado con la fase es bueno para un gran número de configuraciones de la máquina.

Además se ha estudiado la posibilidad de medir otras resonancias. En particular se ha conseguido medir, obteniendo un excelente acuerdo con el modelo, una resonancia bidimensional, o de acoplamiento no lineal, de origen sextupolar. Para llevar acabo esta medida se excitaron oscilaciones betatrónicas en los dos planos transversos. En el plano vertical es suficiente una amplitud pequeña y constante mientras que en el horizontal se deben adquirir datos a diferentes amplitudes con el fin de poder realizar un buen ajuste. Es un resultado de la teoría que la linea espectral (-1,-1) observada en el plano vertical normalizada a la amplitud de la linea (0,1) es proporcional a la amplitud de oscilación horizontal. La pendiente de esta curva es proporcional al término sextupolar h_{0120}. Haciendo un ajuste lineal de la amplitud de la linea (-1,-1) respecto de la amplitud del "kick" horizontal se determinó el término resonante h_{0120} mostrando un acuerdo excelente con el modelo.

Se ha estudiado también la posibilidad de medir resonancias de orden superior al sextupolar. En el SPS no existen imanes de orden superior al octupolar por lo que se eligió como objetivo la medida de una resonancia octupolar durante un corto espacio de tiempo en un experimento. Los octupoles se ajustaron para cancelar el corrimiento del tono con la amplitud de la "máquina base". Alimentar con mayor potencia estos octupolos, para crear una mayor no linealidad, causaría una excesiva decoherencia. Para maximizar el efecto de los octupolos se movió el tono fraccional horizontal cerca de la resonancia (4,0), desde 0.18 a 0.26. A continuación se realizó la adquisición de datos de una forma análoga a como se hizo para el caso sextupolar. La linea espectral a evaluar es la (-3,0) de la señal horizontal. Desafortunadamente se encontraron dos obstáculos para la determinación del término octupolar. El primero se debe a la pequeña amplitud de la linea (-3,0), que sólo era superior al ruido para los tres "kicks" de mayor amplitud, causando

un gran error tanto en las medidas como en los resultados del posterior ajuste. El segundo obstáculo, de carácter analítico, es que esta linea espectral está dominada por la contribución de segundo orden de los campos sextupolares. Esto imposibilitaría una medida precisa de los términos octupolares. Este, en principio, es un problema exclusivo de las resonancias octupolares ya que se ven afectadas por el segundo orden de las sextupolares, que es grande debido a la existencia de numerosos sextupolos. Resonancias de orden decapolar o superior estarían libres de este efecto. Debido principalmente al primer obstáculo la comparación de la linea espectral (-3,0) del modelo con la misma linea de los resultados experimentales denota un desacuerdo. Sobrepasa a esta tesis el estudio de refinamientos de la técnica que permitieran medir estas resonancias octupolares.

Para finalizar con los experimentos en el SPS citaremos como en el transcurso de éstos se utilizó la técnica presentada para hallar el origen de un desacuerdo entre medida y modelo. Supuestamente se habían efectuado medidas con los ocho sextupolos de extracción conectados pero la medida del término sextupolar f_{3000} daba en claro desacuerdo con el modelo. Estudiando detenidamente la medida se observó que en la posición de uno de los sextupolos no había cambio abrupto del término f_{3000} por lo que esto podría indicar que aquel sextupolo no estaba conectado durante el experimento. Se pudo comprobar, gracias al sistema de alarmas del SPS [38] que, de hecho, este sextupolo permaneció desconectado durante el experimento.

Descripción del RHIC

En el marco de una colaboración entre el CERN y el BNL se realizó un experimento para medir términos sextupolares en el RHIC del BNL. El RHIC es un colisionador de iones pesados de un radio promedio de 610 m. Sus dipolos son imanes superconductores que alcanzan, durante la óptica de colisión, los 3.5 T. RHIC puede proporcionar, entre otras, colisiones oro-oro con una energía de 200 GeV y lleva en operación desde el año 2000 y pretende contribuir al desarrollo de la física en un amplio rango de disciplinas como la física nuclear, la física de partículas, la física de la materia condensada, la astrofísica y la cosmología.

Es necesaria la elaboración de un modelo del RHIC que tenga en cuenta todas las posibles fuentes de campos sextupolares. Además de los sextupolos dedicados a la corrección de la cromaticidad, las componentes sextupolares más importantes provienen de los errores de los dipolos superconductores. Estas componentes y otras de orden superior han sido medidas previamente [40, 41]. En el modelo se incorporan todas estas componentes con los valores procedentes de las medidas. También se introducen en los cuadrupolos del modelo aquellos errores de origen geométrico, sin tener en cuenta cualquier otro tipo de error. Los tonos y la cromaticidad del modelo se ajustan a los observados en el experimento. La órbita cerrada no se tiene en cuenta y se considera despreciable ya que aquellos datos con una gran órbita cerrada fueron descartados. Un sextupolo de una región de interacción fue usado como sonda para introducir distintas fuerzas de las resonancias

sextupolares.

EL experimento del 2002 en el RHIC

El experimento se realizó de forma idéntica a los del SPS con la diferencia de que las oscilaciones transversas se excitaron inyectando fuera de la órbita en lugar de la aplicación de un "kick". El haz estaba compuesto por iones de oro. Se adquirieron datos provenientes de los monitores de posición del haz para cinco fuerzas diferentes del sextupolo sonda. Tras el análisis de los datos y una minuciosa elaboración del modelo (ahora se trata de una máquina superconductora con una gran cantidad de fuentes sextupolares) se obtuvo un buen acuerdo para la resonancia sextupolar (3,0). También se midió otra resonancia sextupolar, la (1,0). En ésta última se encontraron discrepancias entre modelo y experimento para las configuraciones con polaridad negativa del sextupolo sonda, mientras que para los casos con polaridad positiva el acuerdo era bueno. Se desconoce el posible origen de esta discrepancia. Hay que añadir que sólo se pudieron usar los datos provenientes de un par de monitores del haz debido a que el resto de monitores presentaba errores de funcionamiento.

Estudio analítico de la dinámica en presencia de un dipolo AC

La última contribución desarrollada en esta tesis ha sido el estudio analítico de cómo se podría hacer uso de un nuevo instrumento instalado en varios aceleradores, un dipolo AC, para mejorar la técnica descrita anteriormente. Un dipolo AC es un dipolo alimentado con corriente alterna que es capaz de introducir oscilaciones transversales forzadas en el haz con una frecuencia próxima al tono. La gran ventaja de la utilización de este instrumento en sustitución del "kick" es que la medida no es desctructiva, ya que estas oscilaciones se pueden inducir de forma adiabática. Para asegurar la adiabaticidad de este proceso la amplitud de la corriente AC con la que se alimenta el dipolo ha de incrementarse linealmente desde cero hasta el valor deseado de una forma lenta. De igual manera cuando se desea desconectar el dipolo AC la amplitud de la corriente se va disminuyendo lenta y linealmente hasta cero. De esta forma la talla del haz se mantiene constante durante el proceso, en contraposición con lo que ocurre tras la aplicación de un "kick".

En esta tesis se estudia la dinámica transversa de las oscilaciones forzadas por un dipolo AC en presencia de no linealidades. Como herramientas para el desarrollo de las expresiones analíticas se adoptan la "Forma Normal" y el álgebra de Lie. La barrera que supone la dependencia temporal del Hamiltoniano (proveniente del dipolo AC) se salva introduciendo un nuevo grado de libertad. De esta forma se pueden seguir pasos similares a los de [6] para llegar a una expresión de la dinámica vuelta tras vuelta. Una vez que se obtienen las expresiones de la dinámica vuelta tras vuelta se observa la aparición de un gran número de resonancias que involucran la frecuencia del dipolo AC. Estas expresiones son exactas hasta el primer orden perturbativo de las no linealidades pero presenta una gran complejidad debido al gran numero de lineas espectrales emergentes. Una gran parte de estas nuevas lineas espectrales tienen su origen en una oscialación forzada parásita con frecuencia opuesta a la de la fundamental. Si el tono de la máquina y el

tono del dipolo AC se encuentran lo bastante próximos estas oscilaciones parásitas se pueden despreciar frente a las fundamentales, llegando a unas expresiones mas sencillas para la dinámica vuelta tras vuelta. De estas expresiones se concluye que los términos resonantes en presencia de un dipolo AC son numéricamente diferentes a aquellos de la "máquina base". Esto supone una complicación ya que los términos que realmente se desean medir y compensar son los de la "máquina base". En cualquier caso esta diferencia debe ser pequeña y los nuevos términos contienen la información local de igual forma que los ya discutidos. Por lo que el potencial que ofrece este método de medida es enorme teniendo en cuenta que la adquisición de datos puede prolongarse a nuestro deseo ya que el haz no se verá afectado.

Otras técnicas para la medición de no linealidades

Diversas técnicas para la medición de no linealidades, basadas en medidas del haz, se están desarrollando en el presente. En esta tesis se ha querido hacer un compendio de éstas citando algunos de sus ventajas e inconvenientes. En la tabla 10.1 se encuentra una clasificación de estas técnicas basada en el tipo de perturbación aplicado al hacer la medida. Una de las características mas importantes de la técnica de medida es si es destructiva o no, i.e. si el haz que se está midiendo podrá ser utilizado posteriormente en colisiones o no. La clara desventaja de las medidas destructivas es que exigirían el sacrificio de algunos haces. Pero para juzgar la utilidad de los distintos métodos hay que tener en cuenta otros factores como son: si la medida contiene la información local o un promedio global, el tiempo de medida, la necesidad de instrumentación dedicada, etc. En lo que sigue se describen brevemente las distintas técnicas en el mismo orden que se presentan en la tabla 10.1.

- **"Orbit bump" estático**: Un "orbit bump" es una modificación local de la órbita de referencia mediante el uso de dipolos correctores. Este tipo de imanes se encuentra disponible en todos los aceleradores. El principio de esta técnica es que las no linealidades comprendidas en el 'orbit bump" actúan sobre la dinámica del haz de forma medible. Los principales observables son los tonos pero también las alteraciones de la órbita fuera del "orbit bump" sirven para inferir las no linealidades contenidas en él. La información obtenida con este método es local y para cubrir toda la máquina es necesario la aplicación del método repetidas veces. Es de gran relevancia que puede ser no destructivo si se usa un Phase Lock Loop (PLL) para la medición de los tonos.

- **"Orbit bump" oscilante**: Si el "orbit bump" se programa para oscilar con una o más frecuencias las no linealidades comprendidas en él causarán la aparición de lineas espectrales con frecuencias múltiplos de las del "orbit bump" en la dinámica del haz. En principio este método no es destructivo pero aún no se ha conseguido aplicar con éxito.

- **Desplazamiento radial**: Consiste en cambiar la energía del haz para cam-

biar el radio promedio de curvatura, típicamente del orden de 1 a 10 mm. Así pues es como un "orbit bump" global que puede proporcionar medidas de las no linealidades en promedio. Se han realizado estudios experimentales en los que tras suponer la localización de las fuentes se les puede otorgar valores numéricos.

- **"Kick" de energía**: Tras un "kick" de energía, la energía del haz oscila harmónicamente. Debido a la existencia de acoplamiento transverso-longitudinal esta oscilación harmónica se traslada al plano transverso. La información obtenida por este método es similar al presentado en esta tesis y al dipolo AC. Es destructiva y aún no existe aplicación experimental.

- **Modulación de la fase RF**: Modulando la fase de la radio-frecuencia se modula a su vez la energía. Esta técnica es similar a la anterior. Se ha aplicado experimentalmente para medir la cromaticidad en el SPS.

- **"Kick" dipolar como corrector**: Aplicando un corrector dipolar a distintas amplitudes de campo magnético se estudia la respuesta de la órbita cerrada. Proporciona información local y ya se ha aplicado para medir campos de acoplamiento en el RHIC.

- **"Kick"**: Mediante la aplicación de un "kick" se excitan oscilaciones horizontales y verticales en el haz. En este apartado se halla la técnica motivo de esta tesis y muchas otras. Todas ellas son destructivas pero difieren en el análisis. Como ya se ha dicho, la técnica presentada en esta tesis se basa en el espectro de Fourier de los datos de los monitores de posición. Otro tipo de análisis consiste en el cálculo de mapas de transferencia. Entre dos puntos cualesquiera de la máquina se trata de hacer un ajuste polinomial de la aplicación que los conecta. No se han encontrado aplicaciones prácticas de este método. Otro tipo de análisis es el mapa de frecuencias. Se trata esta vez de medir los tonos fundamentales en función de las amplitudes de oscilación. El contenido no lineal del acelerador se plasmará en discontinuidades de esta aplicación. Existen exitosas aplicaciones experimentales en el Advanced Ligth Source (ALS).

- **Dipolo AC**: En esta tesis se ha discutido en profundidad el uso de un dipolo AC para llevar a cabo la medición de no linealidades. La gran ventaja de este instrumento es su capacidad para producir oscilaciones del haz duraderas y no destructivas. Es ideal, pues, para sustituir al "kick" en las técnicas anteriores.

12.3 Conclusión

En esta tesis se ha estudiado y desarrollado un método de medida de términos resonantes del hamiltoniano basado en la transformada de Fourier de los datos proce-

dentes de los BPM. Para llevar a cabo este estudio se han efectuado desarrollos analíticos al igual que experimentos en dos aceleradores: el SPS y el RHIC.

El primer aspecto analítico aquí tratado consiste en evaluar el efecto de la decoherencia en el espectro de los datos provenientes de los monitores del haz. El punto de partida para este estudio es la expresión analítica de la dinámica transversa en presencia de no linealidades [6]. Se ha escogido como modelo del haz distribuciones gausianas de partículas en los tres planos fásicos. Se ha demostrado que la amplitud normalizada de la linea con frecuencia $mQ_{x,y}$ se ve reducida por un factor $|m|$ y que su anchura se incrementa aproximadamente el mismo factor en presencia de decoherencia debida al corrimiento del tono con la amplitud. Se ha demostrado también que la decoherencia debida a la cromaticidad introduce bandas laterales alrededor de todas las líneas espectrales y cambia las amplitudes relativas de las lineas centrales. Ambos tipos de decoherencia son claramente negativos de cara a la medida de los términos del Hamiltoniano vía análisis de Fourier de la trayectoria del centroide en un acelerador real ya que disminuyen la señal.

Un segundo progreso teórico ha sido el descubrimiento de una propiedad muy útil de los términos del Hamiltoniano. Su amplitud permanece constante en aquellas secciones de la máquina donde no hay fuentes no lineales. En estas secciones su fase varía suavemente. Al menos una de estas cantidades, amplitud o fase, cambia abruptamente allá donde se encuentran las correspondientes fuentes no lineales. En una máquina real esta propiedad permitiría localizar imperfecciones comparando las medidas de estos términos en los BPMs con las predicciones del modelo en los mismos lugares.

Durante tres años se han realizado experimentos para medir términos resonantes en el SPS usando el "kick" como método de perturbación. Para realizar dicha medida se usaron: cuadrupolos girados 45 grados para introducir o minimizar el acoplamiento transverso y ocho sextupolos para introducir una cantidad conocida y controlada de no linealidad. Para la medición de las no linealidades las oscilaciones betatrónicas se excitaron mediante la aplicación de "kicks" con los "Q-kickers" y el "kicker" horizontal de extracción. La conclusión principal es que se han medido satisfactoriamente términos resonantes de acoplamiento y sextupolares y que el acuerdo entre estos y los predichos por el modelo ha sido bueno. A continuación describimos los diferentes progresos que han llevado a esta conclusión. Se ha definido un nuevo observable para el acoplamiento basado en la amplitud normalizada de las lineas secundarias de los espectros. Este observable es independiente de las amplitudes de oscilación y de la calibración de los BPMs y, de forma natural, sirve para compensar el acoplamiento. De las medidas de términos sextupolares se pudieron inferir inesperadas configuraciones de los sextupolos de extracción. En particular, se encontró que las polaridades de los sextupolos de extracción eran opuestas a las de los sextupolos de cromaticidad. También se encontró, gracias a esta medida, que durante un experimento uno de los sextupolos permaneció desconectado accidentalmente. Los efectos predichos en el espectro de Fourier debidos a la decoherencia se comprobaron numerosas veces. La fase de los términos sextupolares se midió por primera vez alrededor del SPS. También

se evaluó por primera vez una resonancia de acoplamiento no lineal de orden sex-tupolar. Esta técnica no se vio afectada por la energía de los protones en el rango de 26 a 120 GeV. Tampoco se vio afectada por la intensidad del haz en un rango de 0.5×10^{10} a 6×10^{10} protones.

Por primera vez se pudo demostrar que la medida de términos sextupolares es viable en RHIC, una máquina superconductora como lo será el LHC. Se midieron dos tipos de resonancias sextupolares horizontales obteniendo un buen acuerdo entre el experimento y las predicciones del modelo. Importantes discrepancias para la resonancia mas débil, la (1,0), en polaridades negativas del sextupolo sonda permanecen inexplicadas. Debido a que no se disponía de medidas de todos los BPMs alrededor del anillo los términos resonantes se calcularon solamente en una coordenada longitudinal.

Hasta el momento esta técnica de medida es destructiva ya que debido al "kick" aplicado la emitancia transversal se incrementa. Este problema se podría solu-cionar mediante el uso de un dipolo AC para forzar oscilaciones en el haz, ya que estas se podrían introducir de una forma adiabática. En esta tesis se ha presentado un método para calcular la "Forma Normal" del Hamiltoniano en presencia de un dipolo AC y no linealidades. Se ha llegado a la conclusion de que los términos reso-nantes en presencia de un dipolo AC son diferentes a aquellos de la máquina libre. Pero en cualquier caso sus diferencias no deberían ser grandes y la información local contenida en ambos casos es equivalente. Estas predicciones han sido confir-madas mediante simulaciones en un anillo de estructura FODO con sextupolos. En el caso mas académico en el que sólo una resonancia era excitada el acuerdo es ex-celente mientras que en el caso mas general con 108 sextupolos aparecen pequeñas discrepancias debidas a contribuciones de diferentes términos resonantes.

Las técnicas estudiadas en esta tesis tendrán una directa aplicación en el fu-turo LHC para la detección, corrección y localización de errores de la máquina. El LHC, al igual que el RHIC, estará compuesto por un gran número de imanes superconductores con componentes multipolares de gran influencia para la estabil-idad del haz. De hecho, es posible que se equipe al LHC con un dipolo AC con el principal objetivo de controlar tanto parámetros lineales como no lineales

Appendix A

Spectral response to particle distributions

A.1 Centroid normalized horizontal coordinate

To compute the centroid of a Gaussian beam as a function of the number of turns N the expression of $h_x^- N$, given in eq. (3.38), is integrated over the phase space weighted with the densities:

$$\rho_x(I_x, \psi_x) = \frac{1}{2\pi} e^{-\frac{1}{2}(2I_x + \overline{A}_x^2 - 2\overline{A}_x \sqrt{2I_x} \cos \psi_x)} \tag{A.1}$$

$$\rho_y(I_y, \psi_y) = \frac{1}{2\pi} e^{-\frac{1}{2}(2I_y + \overline{A}_y^2 - 2\overline{A}_y \sqrt{2I_y} \cos \psi_y)} \tag{A.2}$$

$$\rho_s(\delta, \psi_s) = \frac{\delta}{2\pi\sigma_s^2} e^{-\delta^2/(2\sigma_s^2)} \tag{A.3}$$

The horizontal coordinate of the centroid is therefore represented by

$$\overline{h_x^-}(N) = \int_0^\infty dI_x dI_y d\delta \int_0^{2\pi} d\psi_x d\psi_y d\psi_s \rho_x(I_x, \psi_x) \rho_y(I_y, \psi_y) \rho_s(\delta, \psi_s) h_x^-(N) \tag{A.4}$$

Since $h_x^-(N)$ contains a sumation this equation becomes a sumation of integrals:

$$\overline{h_x^-}(N) = L_{1100}(N) - 2i \sum_{jklm} j f_{jklm} L_{(j+k-1)(1-j+k)(l+m)(m-l)}(N) \tag{A.5}$$

where L_{nmlk} are defined as

$$L_{nmlk} = \int dV^6 \rho(I_x, \psi_x, I_y, \psi_y, \delta, \psi_s)(2I_x)^{n/2}(2I_y)^{l/2} \times$$
$$e^{i[m(2\pi\hat{\nu}_x N + \psi_x) + k(2\pi\hat{\nu}_y N + \psi_y)]} \tag{A.6}$$

for any integer n, m, l, k, dV^6 stands for $dI_x dI_y d\delta d\psi_x d\psi_y d\psi_s$ and the tunes $\hat{\nu}_x$ and $\hat{\nu}_y$ are defined by the expressions:

$$\hat{\nu}_x = \nu_{x0} + \nu'_{xx} 2I_x + \nu'_{xy} 2I_y + \Delta\nu_x$$
$$\hat{\nu}_y = \nu_{y0} + \nu'_{yx} 2I_x + \nu'_{yy} 2I_y + \Delta\nu_y \tag{A.7}$$

131

where all these quantities were introduced in eqs. (4.2) and (4.4). The following simplifications may be performed on the term L_{nmlk}.

- **Integral over the longitudinal plane:** Isolating all terms containing ψ_s, one gets

$$\frac{1}{2\pi} \int_0^{2\pi} d\psi_s e^{i2\delta\xi_{mk}\cos(\pi Q_s N + \psi_s)\sin(\pi Q_s N)/Q_s} = J_0(2\delta\xi_{mk}\sin(\pi Q_s N)/Q_s)$$
(A.8)

with $\xi_{mk} = (mQ'_x + kQ'_y)$ and J_0 being the Bessel function of order 0. Grouping all terms containing δ and integrating over this variable one gets

$$\frac{1}{\sigma_s^2} \int_0^\infty d\delta \ \delta J_0(2\delta\xi_{mk}\sin(\pi Q_s)/Q_s)e^{-\delta^2/(2\sigma_s^2)} = e^{-2\xi_{mk}^2\sigma_s^2\sin^2(\pi Q_s N)/Q_s^2}$$
(A.9)

- **Integral over the phases in the transverse planes:** Isolating all the terms containing ψ_x or ψ_y, the integral over these variables stays:

$$\frac{1}{(2\pi)^2} \int_0^{2\pi} d\psi_x d\psi_y e^{\overline{A}_x\sqrt{2I_x}\cos\psi_x + \overline{A}_y\sqrt{2I_y}\cos\psi_y + i(m\psi_x + k\psi_y)} =$$
$$\mathrm{I}_m(\overline{A}_x\sqrt{2I_x})\mathrm{I}_k(\overline{A}_y\sqrt{2I_y}) \quad \text{(A.10)}$$

where the I_n represents the modified Bessel function of order n.

Using these simplifications L_{nmlk} can be expressed as an integral over the two transverse invariants given by

$$L_{nmlk}(N) = \int_0^\infty dI_x dI_y (2I_x)^{n/2} (2I_y)^{l/2} e^{-\frac{1}{2}(2I_x + \overline{A}_x^2 + 2I_y + \overline{A}_y^2)} \times$$
$$\mathrm{I}_m(\overline{A}_x\sqrt{2I_x})\mathrm{I}_k(\overline{A}_y\sqrt{2I_y})e^{i2\pi(m\nu_x + k\nu_y)N - 2\gamma_{mk}^2\sin^2(\pi Q_s N)} \quad \text{(A.11)}$$

with $\gamma_{mk} = \xi_{mk}\sigma_s/Q_s$. Notice that ν_x and ν_y do contain only the amplitude detuning as expressed in eq. (4.2). In the following section the Fourier transform of this expression is computed.

A.2   Fourier transformation of the centroid motion

The Fourier transform of $\overline{h_x^-}(N)$ is represented by $H_x^-(w)$. Since the Fourier transformation is a linear operator each term of the r.h.s. of eq. (A.5) gives a contribution to $H_x^-(w)$, this is expressed by

$$H_x^-(w) = \int dN \ \overline{h_x^-}(N) \ e^{-iwN} \equiv H_{xtune}^-(w) + \sum_{jklm} H_{jklm}^-(w) \quad \text{(A.12)}$$

To compute this transformation in the general case the following integral has to be solved for arbitrary integers m and k,

$$\mathcal{F}_{mk}(w) = \int dN e^{i2\pi(m\nu_x + k\nu_y - w/2\pi)N - 2\gamma_{mk}^2 \sin^2(\pi Q_s N)} \qquad (A.13)$$

To calculate this integral the $\sin^2(\pi Q_s N)$ term is expressed as $(1 - \cos(2\pi Q_s N))/2$ and $e^{\gamma_{mk}^2 \cos(2\pi Q_s N)}$ is expanded in power series, giving

$$\mathcal{F}_{mk}(w) = e^{-\gamma_{mk}^2} \int dN e^{i2\pi(m\nu_x + k\nu_y - w/2\pi)N} \sum_{h=0}^{\infty} \frac{\gamma_{mk}^{2h}}{h!} \cos^h(2\pi Q_s N) \quad (A.14)$$

Taking $\cos^h(2\pi Q_s N)$ as a sum of exponentials,

$$\cos^h(2\pi Q_s N) = \sum_{j=0}^{h} \frac{h!}{(h-j)!j!2^h} e^{i2\pi(h-2j)Q_s N} \qquad (A.15)$$

and introducing this expression into eq. (A.14) we obtain:

$$\begin{aligned}
\mathcal{F}_{mk}(w) &= e^{-\gamma_{mk}^2} \sum_{h=0}^{\infty} \sum_{j=0}^{h} \frac{\gamma_{mk}^{2h}}{(h-j)!j!2^h} \int dN e^{i2\pi(m\nu_x + k\nu_y - w/2\pi + (h-2j)Q_s)N} \\
&= e^{-\gamma_{mk}^2} \sum_{h=0}^{\infty} \sum_{j=0}^{h} \frac{\gamma_{mk}^{2h}}{(h-j)!j!2^h} \delta_{Dirac}(m\nu_x + k\nu_y - w/2\pi + (h-2j)Q_s)
\end{aligned}$$

where $\delta_{Dirac}(m\nu_x + k\nu_y - w/2\pi + (h-2j)Q_s)$ is the Dirac delta function. This last expression can be simplified by changing the sum indexes. Defining $q = (h - 2j)$, j goes from 0 to ∞ and q from $-\infty$ to $+\infty$. The summation over j leads to a modified Bessel function of order q expressed as

$$\sum_{j=0}^{\infty} \frac{\gamma_{mk}^{2(2j+q)}}{(j+q)!j!2^{(2j+q)}} \delta_{Dirac}(m\nu_x + k\nu_y - w/2\pi + qQ_s) =$$

$$I_q(\gamma_{mk}^2) \delta_{Dirac}(m\nu_x + k\nu_y - w/2\pi + qQ_s) \quad (A.16)$$

and writing $\mathcal{F}_{mk}(w)$ with the summation over q yields

$$\mathcal{F}_{mk}(w) = e^{-\gamma_{mk}^2} \sum_{q=-\infty}^{\infty} I_q(\gamma_{mk}^2) \delta_{Dirac}(m\nu_x + k\nu_y - w/2\pi + qQ_s) \quad (A.17)$$

This result is used to calculate the Fourier transform $H_x^-(w)$. In particular $H_{xtune}^-(w)$ and $H_{xjklm}^-(w)$ are expressed as follows

$$
\begin{aligned}
H_{xtune}^-(w) &= \int_0^\infty dI_x dI_y \sqrt{2I_x}\, e^{-\frac{1}{2}(2I_x + \overline{A}_x^2 + 2I_y + \overline{A}_y^2)}\, \mathrm{I}_1(\overline{A}_x \sqrt{2I_x}) \times \\
&\qquad \mathrm{I}_0(\overline{A}_y \sqrt{2I_y})\, \mathcal{F}_{10}(w) \qquad\qquad\qquad\qquad\qquad (A.18) \\
H_{xjklm}^-(w) &= -2ij f_{jklm} \int_0^\infty dI_x dI_y (2I_x)^{(j+k-1)/2}(2I_y)^{(l+k)/2} \times \\
&\qquad e^{-\frac{1}{2}(2I_x + \overline{A}_x^2 + 2I_y + \overline{A}_y^2)} \mathrm{I}_{(1-j+k)}(\overline{A}_x \sqrt{2I_x})\, \mathrm{I}_{(m-l)}(\overline{A}_y \sqrt{2I_y}) \times \\
&\qquad \mathcal{F}_{(1-j+k)(m-l)}(w) \qquad\qquad\qquad\qquad\qquad\quad (A.19)
\end{aligned}
$$

Using the properties of the Dirac delta function contained in $\mathcal{F}_{mk}(w)$ the integral over I_x is performed expressing the tunes as in eqs. (4.2). The proper value of I_x is obtained by equating to zero the argument of the Dirac delta function of eq. (A.17). This is expressed as a function of w and I_y and the indexes m and k of the function $\mathcal{F}_{mk}(w)$ contained in the integral by

$$
\begin{aligned}
2I_{x,mkq}(w, I_y) &= \qquad\qquad\qquad\qquad\qquad\qquad\qquad\qquad\qquad (A.20) \\
&\frac{1}{m\nu'_{xx} + k\nu'_{yx}}(w/2\pi - qQ_s - m(\nu_{x0} + \nu_{xy}2I_y) - k(\nu_{y0} + \nu_{yy}2I_y))
\end{aligned}
$$

Since $I_{x,mkq}$ is an amplitude $I_{x,mkq} \geq 0$. It has to be imposed that $I_{x,mkq}$ is zero when the r.h.s. of eq. (A.20) is smaller than zero. To better interpret eqs. (A.18) and (A.19) the following functions are defined,

$$
\begin{aligned}
\mathcal{A}_{xtune}^-(w) &= \frac{1}{|\nu'_{xx}|} \int_0^\infty dI_y \sqrt{2I_{x,100}(w, I_y)}\, e^{-\frac{1}{2}(2I_{x,100}(w,I_y) + \overline{A}_x^2 + 2I_y + \overline{A}_y^2)} \times \\
&\qquad \mathrm{I}_1(\overline{A}_x \sqrt{2I_{x,100}(w, I_y)})\mathrm{I}_0(\overline{A}_y \sqrt{2I_y}) \qquad\qquad\qquad (A.21) \\
\mathcal{A}_{xjklm}^-(w) &= \frac{-2ij f_{jklm}}{|(1-j+k)\nu'_{xx} + (m-l)\nu'_{yx}|} \int_0^\infty dI_y \\
&\qquad (2I_{x,(1-j+k)(m-l)0}(w, I_y))^{(j+k-1)/2}(2I_y)^{(l+k)/2} \times \\
&\qquad e^{-\frac{1}{2}(2I_{x,(1-j+k)(m-l)0}(w,I_y) + \overline{A}_x^2 + 2I_y + \overline{A}_y^2)}\mathrm{I}_{(m-l)}(\overline{A}_y \sqrt{2I_y}) \times \\
&\qquad \mathrm{I}_{(1-j+k)}(\overline{A}_x \sqrt{2I_{x,(1-j+k)(m-l)0}(w, I_y)}) \qquad\qquad (A.22)
\end{aligned}
$$

where $I_{x,mk0}(w, I_y)$ is the function defined in eq. (A.20) with $q = 0$ (q is explicitly reintroduced later). Lastly the terms of the Fourier transform $H_{xtune}^-(w)$ and

$H^-_{xjklm}(w)$ may be written as:

$$
\begin{aligned}
H^-_{xtune}(w) \;=\;& \mathcal{A}^-_{xtune}(w)\, e^{-\gamma^2_{10}} I_0(\gamma^2_{10}) \;+ \\
& \sum_{q=1}^{\infty} e^{-\gamma^2_{10}} I_q(\gamma^2_{10}) [\mathcal{A}^-_{xtune}(w + q2\pi Q_s) + \mathcal{A}^-_{xtune}(w - q2\pi Q_s)]
\end{aligned}
\tag{A.23}
$$

$$
\begin{aligned}
H^-_{xjklm}(w) \;=\;& \mathcal{A}^-_{xjklm}(w)\, e^{-\gamma^2_{(1-j+k)(m-l)}} I_0(\gamma^2_{(1-j+k)(m-l)}) \;+ \\
& \sum_{q=1}^{\infty} e^{-\gamma^2_{(1-j+k)(m-l)}} I_q(\gamma^2_{(1-j+k)(m-l)}) \;\times \\
& [\mathcal{A}^-_{xjklm}(w + q2\pi Q_s) + \mathcal{A}^-_{xjklm}(w - q2\pi Q_s)]
\end{aligned}
\tag{A.24}
$$

Despite the length of the formula its interpretation is quite simple. If chromaticity is zero this implies that $\gamma_{mk} = 0$, $\forall\, m, k$ and then all the modified Bessel functions with index $q > 0$ vanish, resulting in:

$$
\begin{aligned}
H^-_x(w) \;=\;& H^-_{xtune}(w) + \sum_{jklm} H^-_{xjklm}(w) \tag{A.25} \\
=\;& \mathcal{A}^-_{xtune}(w) + \sum_{jklm} \mathcal{A}^-_{xjklm}(w) \tag{A.26}
\end{aligned}
$$

This equation shows how the spectral lines found in the single particle motion eq. (3.38), which had zero width, are transformed into distribution functions. The effect of chromaticity, as seen from eqs. (A.23) and (A.24), is to introduce an infinite number of peaks around the principal ones displaced by integer multipoles of Q_s, this integer represented by q is the order of the sideband.

The functions $\mathcal{A}^-_{xjklm}(w)$ still contain the integral over I_y which has to be done numerically. Nevertheless in those cases where only one transverse plane is relevant for the calculations, an analytical expression of $H^-_x(w)$ could be derived.

Appendix B

Spectral lines introduced by h_{3000} and h_{1020} with an AC dipole.

From eq. (9.27) the term h_{3000} (which at the AC dipole location is equal to the term h'_{3000}) contributes to the horizontal motion with the quantity

$$\frac{-6ih_{3000}}{1 - e^{-i2\pi Q_x}R_{x,y}R_\tau}\zeta_x^{+2} \, , \qquad (B.1)$$

where ζ_x^+ is given by

$$\zeta_x^+ = \sqrt{2I_x}e^{-i(\psi_x+\psi_{x0})} + |\delta_{x-}|e^{-i(2\pi Q_{xD}\tau-\eta_{x-})} - |\delta_{x+}|e^{+i(2\pi Q_{xD}\tau+\eta_{x+})} \, . \qquad (B.2)$$

Expanding the square ζ_x^{+2} in eq. (B.1) gives

$$\begin{aligned}
\zeta_x^{+2} &= 2I_x e^{-i2(\psi_x+\psi_{x0})} + |\delta_{x-}|^2 e^{-i2(2\pi Q_{xD}\tau-\eta_{x-})} + |\delta_{x+}|^2 e^{+i2(2\pi Q_{xD}\tau+\eta_{x+})} \\
&\quad + 2\sqrt{2I_x}|\delta_{x-}|e^{-i(\psi_x+\psi_{x0})-i(2\pi Q_{xD}\tau-\eta_{x-})} \\
&\quad - 2\sqrt{2I_x}|\delta_{x+}|e^{-i(\psi_x+\psi_{x0})+i(2\pi Q_{xD}\tau+\eta_{x+})} - 2|\delta_{x-}||\delta_{x+}| \, .
\end{aligned} \qquad (B.3)$$

The frequencies of the lines introduced by this expression are: $-2Q_x$, $-2Q_{xD}$, $2Q_{xD}$, $-Q_x - Q_{xD}$, $-Q_x + Q_{xD}$ and 0.

By virtue of eq. (B.1) the resonance conditions corresponding to the different lines are: $-3Q_x = p$, $-2Q_{xD} - Q_x = p$, $2Q_{xD} - Q_x = p$, $-2Q_x - Q_{xD} = p$, $-2Q_x + Q_{xD} = p$ and $-Q_x = p$ with $p \in Z$.

The equivalent calculation will be done now for the term h_{1020}. From eq. (9.27) the term h_{1020} contributes to the horizontal motion with the quantity

$$\frac{-2ih_{1020}}{1 - e^{-i2\pi Q_x}R_{x,y}R_\tau}\zeta_y^{+2} \, , \qquad (B.4)$$

where ζ_y^+ is given by

$$\zeta_x^+ = \sqrt{2I_y}e^{-i(\psi_x+\psi_{y0})} + |\delta_{y-}|e^{-i(2\pi Q_{yD}\tau-\eta_{y-})} - |\delta_{y+}|e^{+i(2\pi Q_{yD}\tau+\eta_{y+})} \, . \qquad (B.5)$$

Expanding the square $\zeta_y^{+^2}$ in eq. (B.4) gives

$$
\begin{aligned}
\zeta_y^{+^2} &= 2I_y e^{-i2(\psi_y + \psi_{y0})} + |\delta_{y-}|^2 e^{-i2(2\pi Q_{yD}\tau - \eta_{y-})} + |\delta_{y+}|^2 e^{+i2(2\pi Q_{yD}\tau + \eta_{y+})} \\
&\quad + 2\sqrt{2I_y}|\delta_{y-}|e^{-i(\psi_x + \psi_{y0}) - i(2\pi Q_{yD}\tau - \eta_{y-})} \qquad\qquad\qquad (\text{B.6}) \\
&\quad - 2\sqrt{2I_y}|\delta_{y+}|e^{-i(\psi_y + \psi_{y0}) + i(2\pi Q_{yD}\tau + \eta_{y+})} - 2|\delta_{y-}||\delta_{y+}| \; .
\end{aligned}
$$

The frequencies of the lines introduced by this expression are: $-2Q_y$, $-2Q_{yD}$, $2Q_{yD}$, $-Q_y - Q_{yD}$, $-Q_y + Q_{yD}$ and 0.

By virtue of eq. (B.4) the resonance conditions corresponding to the different lines are: $-2Q_y - Q_x = p$, $-2Q_{yD} - Q_x = p$, $2Q_{yD} - Q_x = p$, $-Q_y - Q_x - Q_{xD} = p$, $-Q_y - Q_x + Q_{xD} = p$ and $-Q_x = p$ with $p \in Z$.